# Electronic States on the Clean and Oxygen-Covered Molybdenum (110) Surface Measured Using Time-of-Flight Momentum Microscopy

Dissertation in Physics
to obtain the degree of
"Doktor der Naturwissenschaften"
At the Department of Physics
Johannes Gutenberg University Mainz

Sergii Chernov
Born in Sumy (Ukraine)
Mainz, November 19, 2015

Day of Defence: 20.04.2016

# Abstract

Recent experiments discovered a new class of materials called topological insulators and started an extensive investigation in order to find more materials of such type and to understand and explore the opening perspectives in fundamental science and application. These materials exhibit a Dirac-type (massless) electronic state, bridging the fundamental band gap. Surprisingly, a strongly spin-polarized surface state with linear dispersion resembling that of Dirac type was found on the already well-investigated W(110) surface. This rose the question of the existence of the same non-trivial electron state on other metal surfaces.

The present work describes the investigation of surface electronic states on the Mo(110) surface, their dispersion and transformation upon surface oxidation. This system is isoelectronic to the case of W(110) but due to the lower atomic number the spin-orbit interaction responsible for local band gap formation is substantially decreased by a factor of 5. The Mo(110) surface was shown to exhibit a linearly dispersing state quite similar to the one on W(110), but within a smaller energy range of 120 meV, with the Dirac point lying in the center of a local band gap in k-space.

The experimental investigations were performed with the help of momentum microscopy, using a Ti:sapphire laser in the lab and synchrotron radiation at BESSY II, Berlin. The results show good agreement with theoretical calculations of the band structure and photoemission patterns for clean Mo(110).

The fully parallel 3D acquisition scheme allowed to visualize the full surface Brillouin zone of the sample up to few eV binding energy within a single exposure of typically less than 30 min. This opens the door to future time-resolved experiments with maximum detection efficiency.

# Zusammenfassung

Die kürzlich gemachte experimentelle Entdeckung einer neuen Klasse von Materialien, den sogenannten Topologischen Isolatoren, resultierte in einer ausgedehnten Suche nach weiteren Materialien desselben Typs, um die sich eröffnenden Möglichkeiten, sowohl für die Grundlagenforschung als auch für praktische Anwendungen, zu untersuchen. Die Materialien besitzen einen Dirac-artigen elektronischen Zustand, welcher die zugrundeliegende Bandlücke überbrückt. Überraschenderweise entdeckte man nun auf bereits früher gründlich untersuchten W(110)-Oberflächen einen stark spin-polarisierten Dirac-Oberflächenzustand mit linearer Dispersion (masselose Fermionen). Es stellt sich die Frage nach der Existenz dieses nicht-trivialen elektronischen Zustands auf anderen Metalloberflächen.

Die folgende Arbeit beschreibt die Untersuchung von elektronischen Oberflächenzuständen der Mo(110)-Oberfläche, deren Dispersion und Veränderung durch eine Oxidation der Oberfläche. Dieses System ist W(110) sehr ähnlich, doch aufgrund geringerer Ordnungszahl ist die Spin-Bahn-Wechselwirkung, welche verantwortlich für die Ausbildung der lokalen Bandlücke ist, um einen Faktor 5 reduziert. Die Mo(110)-Oberfläche zeigt einen ähnlichen, linear dispergierenden Zustand wie W(110), allerdings in einem geringeren Energiebereich von 120 meV, mit einem Dirac-Punkt der innerhalb einer lokalen Bandlücke im k-Raum liegt.

Die experimentellen Messungen wurden mittels Impulsmikroskopie mit einem Ti-Saphir Laser im Labor sowie Synchrotron-Strahlung am BESSY II in Berlin durchgeführt. Die Ergebnisse zeigen eine gute Übereinstimmung mit theoretischen Berechnungen der Bandstruktur und Photoemissionsspektren für eine reine Mo(110) Oberfläche.

Die parallele 3D-Datenerfassung ermöglicht es, die komplette Oberflächen-Brillouin-Zone der Probe bis zu wenigen eV Bindungsenergie darzustellen, bei einer einmaligen, kurzen Belichtung von typischerweise weniger als 30 Minuten. Dies öffnet die Tür für zukünftige zeitaufgelöste Experimente mit maximaler Detektionseffizienz.

# Table of contents

# 1. Introduction

Until two decades ago, the role of the electron spin in the electronic structure of solids was classified into basically two different scenarios, those governed by exchange interaction and those governed by spin-orbit interaction. A snapshot of this situation is presented in the textbooks [1] and [2].

The former category comprises the ferromagnetic materials. Here an initial spin polarization of the electrons exists in the solid that can be either in the system of itinerant, i.e. delocalized electrons (prototypical systems being the 3d band ferromagnets Fe, Co, and Ni) or localized in certain orbitals like in rare earth metals or their compounds (a prototypical material being EuO where the initial spin polarization is found in the 4f-subshell. The common characteristic is an angular momentum orientation in the initial state, mediated by exchange interaction. This leads to a macroscopic magnetization in ferromagnets or an antiparallel alignment of the magnetic moments in antiferromagnets.

In materials with significant spin-orbit interaction the electronic bands are split, in analogy to the fine-structure splitting in heavy atoms. In this case there is no macroscopic spin orientation in the initial state. Hence these materials appear paramagnetic, i.e. they have no permanent magnetic moments in zero field. However, in the interaction with circularly polarized light the phenomenon of optical spin orientation can occur. This is a direct consequence of the "magnetic" selection rule $\Delta m_j = \pm 1$ for right- and left-handed circularly polarized light. Optical spin orientation was shown for free Cs atoms [3, 4]. It was used in order to generate an ensemble of highly spin-polarized atoms in the confirmation of the theoretically predicted Fano-effect [5]. This phenomenon was exploited for the detection of band symmetries in heavy paramagnetic materials [6]. The most prominent example for optical spin orientation is the GaAs-source of polarized electrons, as operated at MAMI [7], where the optical spin orientation in strained GaAs-derived materials leads to intense beams of almost fully polarized electrons.

The relevant theoretical paper by Rashba, predicting a ground-state spin orientation in non-ferromagnetic materials, thus opening a third class of spin systems in solids, appeared already 1960 [8]. However, until its experimental proof it received only little attention. The necessary precondition was a vanishing spatial inversion symmetry. In this case, a spin-splitting (nowadays called *Rashba-splitting*) occurs due to a dissymmetric term in the Hamiltonian which, in turn, leads to a splitting of formally degenerate states with spin-up and spin-down. The result is a rigid orientation of the spin-polarization vector with respect

to the momentum vector. Unlike for the class of ferromagnets there is no macroscopic preferential spin orientation, but a "local" one (meaning local in k-space). Later, the consideration that the inversion symmetry is broken on each surface of a crystalline solid led to the prediction of the Rashba -effect at surfaces of heavy materials, today referred to as Rashba-Bychkov effect [9]. The Rashba-effect was largely ignored by the main-stream community studying spin phenomena, until in 1996 La Shell et al. verified the prediction of Rashba and Bychkov for the Au (111)-surface [10]. The spin splitting is mediated by spin-orbit interaction, i.e. it is predominantly visible for heavy materials, although meanwhile the Rashba-Bychkov effect has been confirmed even for materials of intermediate atomic number, like Cu [11].

In the original work of Rashba and Bychkov only the potential gradient perpendicular to the surface was considered. As a consequence of this "*Rashba-Hamiltonian*" the spin orientation for "ideal" systems like Au(111) is oriented parallel to the surface. Since this class of phenomena does not relate to one of the two conventional categories, it is nowadays readily referred to as "*Rashba-Physics*". In the prototypical system Au(111) the Shockley-type surface state (appearing in the band gap of the d-electrons) is split into two paraboloid-shaped bands with opposite spin. The spin-orientation is rigidly fixed transversal to the momentum vector, staying in-plane for this system.

Intense experimental activities started in many groups and it soon became clear that quantitatively not only the potential gradient perpendicular to the surface gives rise to the spin splitting, as in the original prediction of Rashba and Bychkov, but in-plane contributions are of equal importance [12]. These contributions lead to a pronounced rotation of the spin orientation out-of-plane. In fact, many systems show complicated spin textures with spin components varying in-plane and out-of-plane along the circumference of a band feature in k-space.

Being initially more of academic interest, the field of Rashba-Physics suddenly gained tremendous importance in prospective applications when D. Hsieh et al. [13] discovered the first topological insulator bismuth antimonide. In the bulk electronic structure, materials of this class have the typical properties of insulators, i.e. they show a band gap. However, at the surface a metallic state exists. Moreover, this special surface state is "topologically protected", meaning that unlike typical surface states it cannot be destroyed by adsorbates or surface defects. Rather, as reaction to impurities or disorder at the surface, the topologically protected surface state moves into deeper layers of the material. Like the Rashba-effect, the topological surface states are mediated by spin-orbit interaction, i.e. they

require the presence of heavy atoms in the material. The typical appearance of such states is the formation of a Dirac cone (similar to the famous case of graphene [14]), i.e. the bands of this special surface state are characterized by linear E(k)-dispersion. Since a linear E versus k relation is known for massless particles like photons, electrons in such states are also referred to as Dirac-fermions or "massless" electrons. As a consequence of in-plane fields, the Dirac cone usually deviates from perfect rotational symmetry. In fact, it can be strongly warped like in the material $Bi_2Te_3$. The spin polarization can show a complicated texture with significant out-of-plane components [15].

The marked difference between a Rashba-band (like the Shockley state of Au(111)) and a topological surface state is that the former shows a band doublet with opposite spin orientation, whereas the latter shows a Dirac cone with only one preferential spin orientation for a given momentum vector. One consequence of this is that an electric current running along the edge of a topological insulator should be highly spin polarized. This is extremely interesting for applications, because the protected, highly spin polarized state opens a new spin-transport channel for spintronics devices.

As suggested by its name, topologically protected surface states occur on topological insulators. In view of this, it was a surprise that in 2011, the Hiroshima group (Miyamoto et al. [16]) discovered a Dirac-like surface state in a partial band gap of the W(110)-surface using spin-resolved photoelectron spectroscopy.

Theoretical investigations by two different groups [17, 18] confirmed and analyzed the unusual nature of this surface state, which indeed shows strong analogies to the surface states on topological insulators. However, in this case the substrate is metallic. Further experimental and theoretical papers on the exceptional case of the W(110) surface state appeared revealing further details [19, 20].

The surprising existence of a Dirac-like state on a metal rose the question whether similar states occur on the (110)-surfaces of other heavy bcc-metals. An investigation for the analogous Ta(110)-surface by the Münster group in cooperation with the Hiroshima group showed that for this surface no Dirac-like state exists [21, 22].

The purpose of the present Thesis was to investigate the (110)-surface of the isoelectronic bcc material molybdenum. Prior to the present work, it was already known that the surface electronic structures of W and Mo look rather similar [23-25]. However, the question of Dirac-like states was not addressed for Mo. Spin-orbit interaction is essential for the occurrence of this effect, because the surface state arises in a spin-orbit induced partial

band gap. Thus, the case of Mo is particularly interesting because spin-orbit interaction is about a factor of 5 smaller than in W. The reduced spin-orbit coupling has for example dramatic consequences on magnetic anisotropy of ferromagnetic films grown on these surfaces [26]. It is interesting to investigate the subtle differences in the band structure of Mo and W. The experimental work of this Thesis had strong support from theoretical side by the TU München group (H. Ebert et al.), who performed ab-initio calculations for Mo(110) parallel to the measurements.

The experiment employed the newly-developed time of flight momentum microscope of our group. The relevant measurements were performed in a beamtime at the storage ring BESSY II (Berlin) in July 2014. This was the first scientific case studied with the new kind of microscope, therefore an essential part of this Thesis is devoted to the description and characterization of the microscope. Prior to the work at BESSY II, experiments using a Ti-sapphire laser in the lab were performed.

The existence of a Dirac-like state on Mo(110) could be unambiguously verified and the structure of this state could be elucidated in detail, hand in hand with the calculations performed by the theoreticians. A special challenge was the small size of the band gap of only 120 meV at the Γ-point (center of the surface Brillouin zone: $k_{||} = 0$). However, the special texture of the state allowed to follow experimentally the Dirac-like linear dispersion in a rather large $k_{||}$-range away from the center of the Brillouin zone. A second anomalous state with linear dispersion and conical shape was found about midway between the center of the Brillouin zone and the N-point. Both anomalous states are well-reproduced by the theoretical calculations. The full 3D spectral function $I(E_B, k_x, k_y)$ allowed a most detailed quantitative comparison between experiment and theory. In addition to the clean Mo(110)-surface, also the oxygen-covered surface was studied and similarities and differences have been found that can partly be explained in terms of “hole doping” by the oxygen atoms.

The photoelectrons were excited by linearly polarized light (p-polarized). This allowed the determination of the linear dichroism in photoemission in the full half-space above the sample. The quantity of linear dichroism in the photoelectron angular distribution gives information on the symmetries of the electronic bands. The dichroism patterns show the same degree of good agreement with the theoretical ab-initio calculations as the intensity patterns.

# 2. Topologically nontrivial d-derived surface states

The previously discovered new class of materials called topological insulators (TIs), exhibit a Dirac-type electronic state, bridging the band gap. This discovery started an extensive investigation of such materials in order to understand and explore the opening perspectives in fundamental science and application [27]. After investigations of HgTe [28] and bismuth chalkogenide (e.g. $Bi_2Se_3$) [29] systems, the focus has been shifted to the search for new topological insulators [30]. While insulating in the bulk, topological insulators show metallic conductivity at the surface. A nearly linear dispersion of bands bridging the fundamental gap, those electronic state arises as a result of a combination of spin-orbit interaction and time-reversal symmetry. Such a band character provokes much discussion about the similarity to "massless" relativistic particles, where the particle energy is also proportional to its momentum. Another attractive class of materials are systems with Rashba-type spin splitting. Both of these material types (TIs and Rashba systems) are interesting for spintronic applications as they show highly spin-polarized surface states without an external magnetic field.

So far nontrivial electron states in most of the investigated systems were based on *sp*-electrons. A few studies of spin-polarized states in nonmagnetic *d*-electron systems have been published such as W(110) and Ta(110)[16-21]. The possible strong correlation effects among d electrons in Rashba systems and topological insulators have become important scientific targets.

## 2.1 Discovery of an anisotropic Dirac–like surface resonance on W(110)

The criteria for the appearance of Dirac-type states at the surface of topological insulators are well-understood and an increasing number of materials have been predicted to exhibit these special, topologically-protected states. It was a surprise that recently a strongly spin-polarized surface state with linear dispersion resembling that of Dirac type was found on the already well-investigated W(110) surface [16]. This was unexpected as W(110) has no similarities to known TIs except strong spin-orbit interaction because of a large atomic number Z=74. As a metal it has no fundamental band gap (although it still exhibits a local band gap caused by spin-orbit interaction). A band inversion across a fundamental band gap is also missing. Unlike TIs of HgTe and $Bi_2Se_3$ types, tungsten is not a compound. In addition the energy range of the observed surface state is populated by d – electrons while the fundamental band gap in known topological insulators (e.g. $Bi_2Se_3$) is crossed by p electrons. The 'Dirac-like surface state' on W(110) is energetically situated in a partial band gap that

is due to spin–orbit coupling, similar to the spin–orbit-induced fundamental band gap in a topological insulator [17]. The question, whether its existence is connected with a non-trivial (local) topology is still under debate. The surface of W(110) has $C_2v$ symmetry, unlike $C_3v$ in the $Bi_2Se_3$-type system, thus the symmetry of the Dirac-like state is also different. It has a strongly elongated shape exhibiting linear dispersion only in one direction.

It should be mentioned that the surface electronic structure of W is much different from the bulk in consequence of broken lattice symmetry and surface relaxation. The latter for W(110) was investigated by X-ray diffraction [31] and makes up 2.76%.

### 2.1.1. A strongly distorted Dirac-cone-like state based on d-electrons

The method of choice for the study of Dirac states is photoemission. Angular-Resolved Photoelectron Spectroscopy (ARPES) is very surface sensitive, hence it is appropriate to detect surface states of metals. Therefore band mapping requires ultra-high vacuum conditions and a clean sample surface with no adsorbates. Oxidation with subsequent flash in vacuum is a standard procedure for the cleaning of many surfaces [32]. A clean surface of W(110) is obtained by repeated cycles of heating in an oxygen atmosphere ($2\times10^{-6}$ to $2\times10^{-7}$ Pa) at 1500 K and a subsequent flash to 2300 K. The pressure rise during the flash can serve as a relative measure of surface cleanness. The lower the pressure – the lower amount of carbon oxides remain on the surface after oxidation. Thus smaller is the amount of carbon which stays at the surface or comes from the bulk of the sample while heating. In Ref. [19] the pressure during the flash remained below $5x10^{-7}$ Pa. This was sufficient to remove contaminants such as carbon and oxygen from the surface. The surface cleanness was controlled by Auger electron spectroscopy and also by observation of a very sharp (1x1) LEED pattern [19].

ARPES measurements of Miyamoto et al. [16] performed along the $\overline{\Gamma S}$ direction at a photon energy of $h\nu$=22.5 eV (Fig. 2.1(a),(b)) reveal both bulk and surface bands. The broad unsharp features at the Fermi region and region below 1.4 eV change their appearance with a change of photon energy. They also are found to show almost no spin polarization. Therefore they are attributed to bulk continuum states [16].

It is known that the W band structure exhibits a quite large partial band gap that is induced by spin-orbit interaction [18]. In Fig. 2.1(a)-(c) it appears as dark regions but the band structure there shows four characteristic surface states designated as $A, B, S_1$ and $S_1'$. Surface states A and B were proven to be derived from surface dangling bonds by exposing to small amounts of adsorbates. Less than 1 ML coverage of hydrogen causes these states to

disappear [23, 16], thus proving their close relation to the topmost atomic layer. The presence of these states may serve as a criteria of a clean surface in the absence of LEED or other instruments for surface quality examination. It is found that band S1 shows no shift of binding energy upon change of the excitation photon energy. This confirms its two dimensional (surface) nature. Band $S_2$ has different appearance at different photon energies. It is almost invisible at 22.5 eV and attains strong intensity at 43 eV (Fig. 2.1(d)) [16]. It disperses along the band $S_1'$ in the upper region close to the Fermi level, forming together a kind of split band.

Fig. 2.1(c) shows the band structure region containing band S1 measured with enhanced momentum resolution. Consideration of the exact position of this band by defining the most bright point across a line shows that it can be fitted with a straight line in a region of 220 meV binding energy (Fig. 2.1(e)). The hatched areas at the top and bottom mark the bulk states region outside the spin-orbit induced band gap. It is found that the surface state S1 shows almost linear dispersion around the $\overline{\Gamma}$-point ($k_{\parallel} = 0$) close to the crossing point.

The ordinary free electron dispersion would be of parabolic type corresponding to nonrelativistic electrons with an effective mass m* and representing the square dependence of energy on the particle momentum $E \sim \frac{p^2}{2m^*}$. A linear dispersion behaviour like in Fig. 2.1(c) is thus nontrivial and points to nearly zero effective mass in this region of momentum space.

W(110) showed a linear dispersion of the S1 surface state in a region of energies even larger than for the well-known topological insulator $Bi_2Se_3$ where it comprises only a region of 150 meV [33].

At the same time the similarity to the Dirac state is not complete as the linear character along $\overline{\Gamma S}$ is not conserved along $\overline{\Gamma N}$ direction (Fig. 2.2(a)). Rather it shows "heavy" character, meaning a flat band. Constant energy sections of the band structure in Fig. 2.2(b) show that the S1 band is strongly anisotropic and forms a shape of a stretched ellipse at an energy of 0.3 eV above the crossover point and shrinks almost to a line in the region of crossing at the binding energy of 1.25 eV.

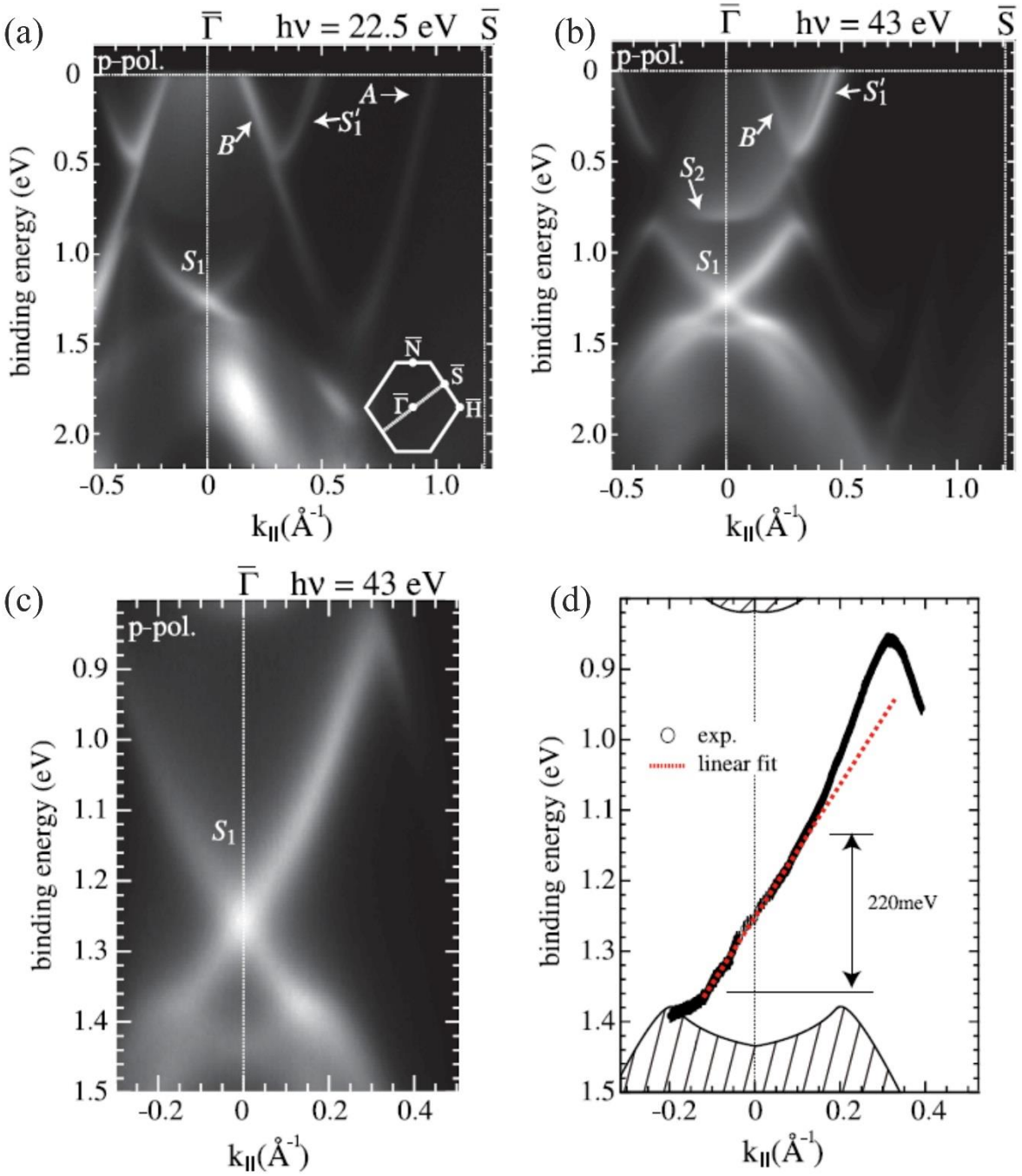


**Fig. 2.1.** Electron band dispersion of W(110) along $\overline{\Gamma S}$ measured with p-polarized light at photon energies of 22.5 eV (a) and 43 eV (b). The band S1 was also measured with better momentum resolution (c). S1 intensity maximum (black line) and its linear fit (red dotted line) are shown in (d). (From Miyamoto et al. [16])

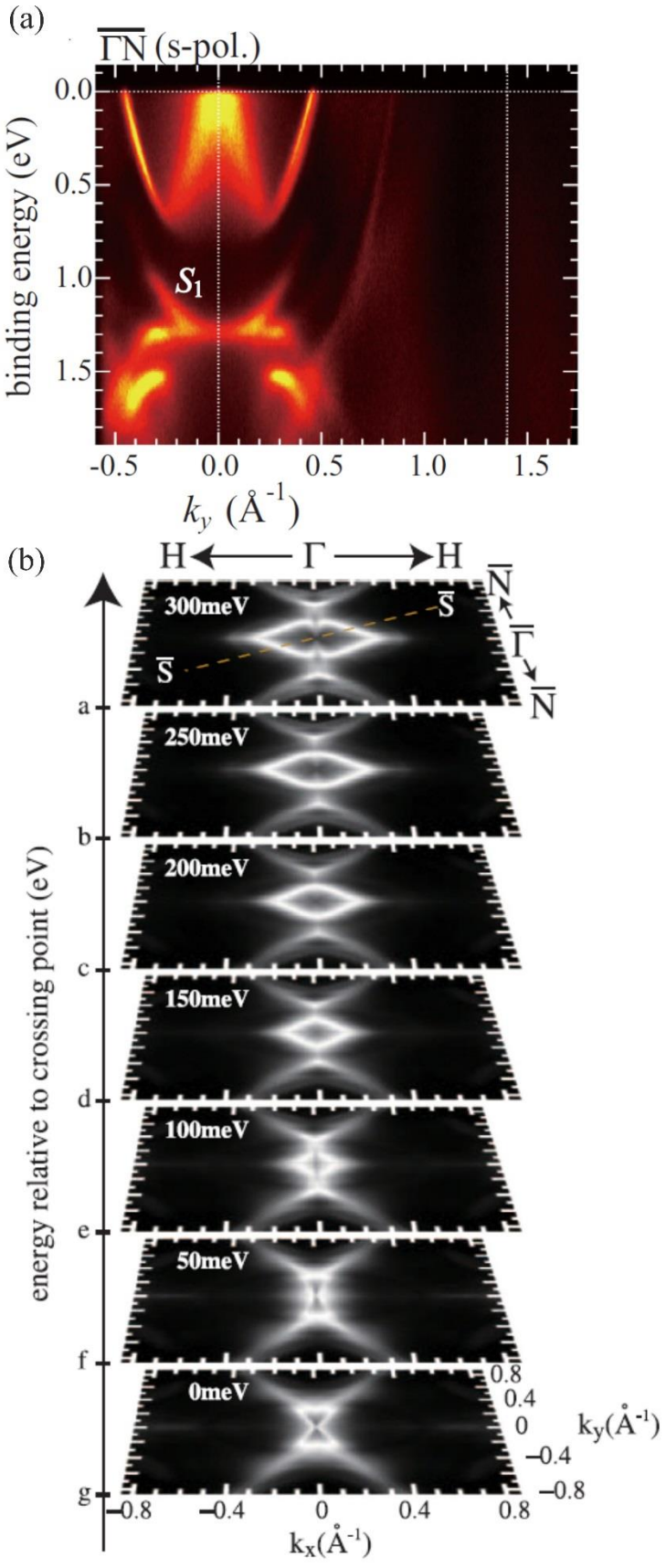


**Fig. 2.2.** W(110) band dispersion along the $\overline{\Gamma N}$ direction measured with s-polarized light at $h\upsilon$= 43 eV (a). Constant energy sections for W(110), 0 meV corresponds to the crossing energy of the S1 band (b). (From Miyamoto et al. [19], [16])

### 2.1.2. Band symmetries probed with linearly polarized light

Upon excitation with polarized light, the photoemission intensities show a dependence on the polarization plane orientation as well as on the azimuthal and polar angles of light incidence. This effect is often referred to as linear (or circular) dichroism in the angular distribution (LDAD or CDAD) and it can serve as a tool for probing the symmetry of electronic bands [34-36] and magnetization of the sample [37]. The linear dichroism effect depends on different factors. Firstly, it is a probe for spatial symmetries which is required for dipole transitions at a given experimental geometry. In turn, spin-orbit and exchange (in case of a magnetic sample) interactions also have an influence on these quantities.

The point group of the (110) surface of a non-magnetic bcc sample like tungsten with light along a high symmetry direction is $C_2v$. It has four irreducible representations in single groups denoted usually as $\Sigma^1$, $\Sigma^2$, $\Sigma^3$, and $\Sigma^4$. Dipole selection rules for transitions into the $\Sigma^1$ final-state band depend on the light polarization: for a component of the polarization vector E along the [110] surface normal (ideally grazing incidence), electrons from $\Sigma^1$ initial states are excited; for a component along the [001] in-plane direction (normal incidence, polarization vector in the [001] azimuth direction), electrons from $\Sigma^3$ initial states are excited [38]. For off-normally p-polarized light in between these two extremes, the light polarization contains both components, so both initial states with either $\Sigma^1$ or $\Sigma^3$ spatial symmetry contribute to the photoemission signal [37].

The effect of spin–orbit coupling on the band structure is to lift all degeneracies at band crossings by inducing hybridization, since all bands exhibit the same double-group symmetry. These bands are thus not allowed to cross each other. In the presence of a magnetization, the bands are further split by the exchange interaction.

For W(110) such a symmetry analysis was performed analyzing ARPES results of high symmetry directions [19]. Measurements were performed with s- and p-polarized light (Fig. 2.3). If the spin-orbit interaction in the system is neglected, an odd or even symmetry can be assigned to bands with respect to each symmetry plane. Considering the strong spin-orbit interaction, it will cause a certain intermixing of symmetries, so all kinds of bands are observable for both polarizations. The exchange interaction is not present for tungsten.

Band A in Fig. 2.3 is observed in both $\overline{\Gamma N}$ and $\overline{\Gamma H}$ but only for p-polarized light. Therefore it is assigned to $\Sigma^1$-type of symmetry. Band S1 shows up for p-polarized light along $\overline{\Gamma H}$ and for s-polarized light along $\overline{\Gamma N}$. It is weakly present also for s-polarized light along $\overline{\Gamma H}$ and for p-polarized light along $\overline{\Gamma N}$.

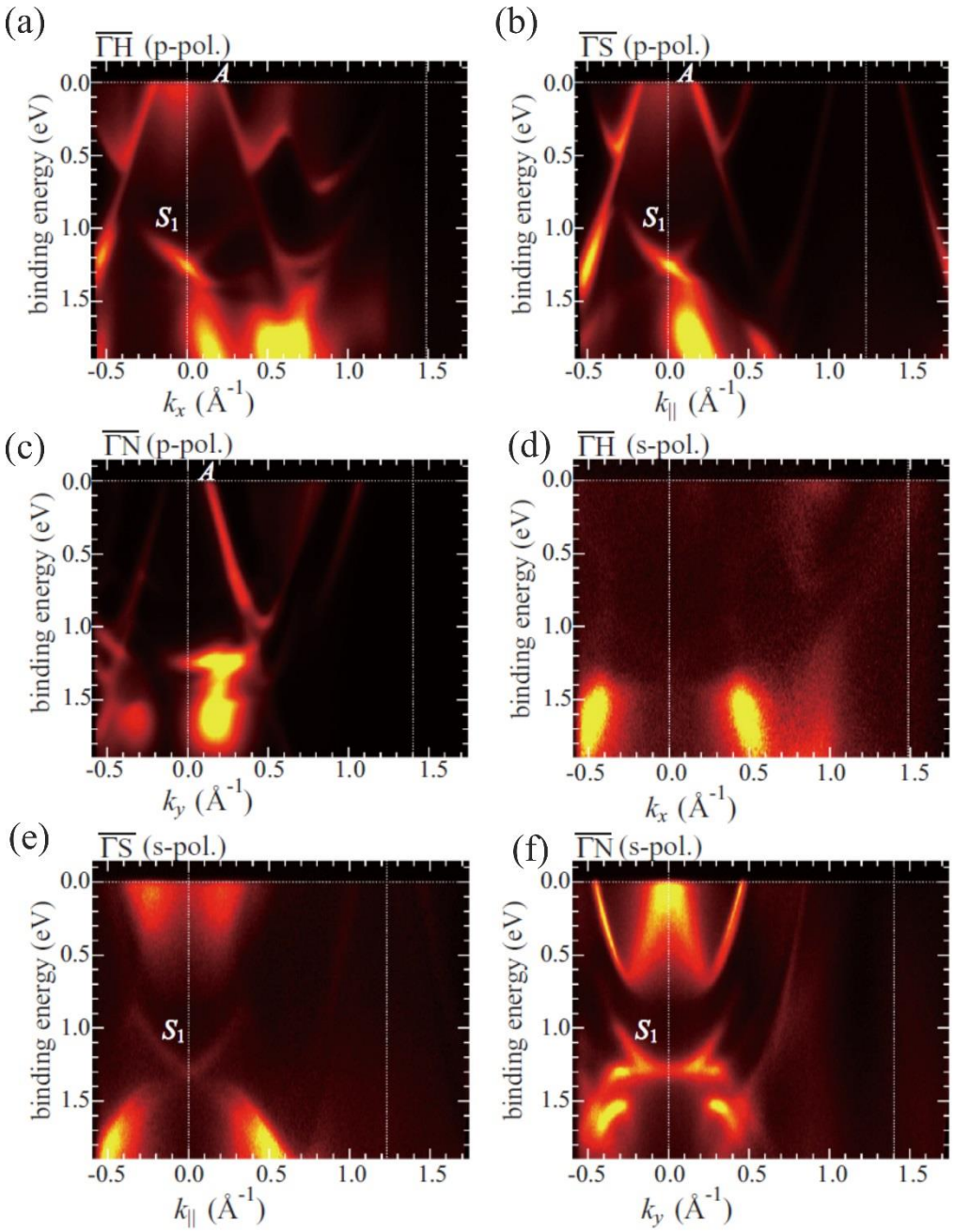


**Fig. 2.3.** W(110) electron bands measured by ARPES at p-polarized (a,b,c) and s-polarized (d,e,f) light with photon energy of 22.5 eV. (From Miyamoto et al. [19])

The intensity is low and the dispersion shape is not clear for the latter cases. As a consequence this band is assigned predominantly to $\Sigma^3$-type of symmetry with small admixtures probably due to spin-orbit coupling. With this, the analysis of the most prominent surface bands is complete. The bulk states in the lower and upper regions (higher and smaller binding energies, respectively) show less clear behavior. For the states below 1.35 eV some signatures appear for p-polarized light along all symmetry directions, while some intensity

still shows up for s-polarized light. From these observations, they are generally assigned to $\Sigma^1$ and $\Sigma^2$ symmetry groups.

### 2.1.3. Spin texture of the Dirac-like states in W(110)

Topological insulators show an interesting spin texture of the Dirac fermions of the surface state. In 2009 it was shown with the help of spin-resolved ARPES that these states are not degenerate and spin polarized [39]. At the Fermi surface they show spins rotating by 360º around the center of the Brillouin zone connecting the momentum and spin of the electrons in perpendicular orientation. In addition, this leads to a Berry phase of π and to nontrivial properties of such a 2D electron gas. This has an effect of decreasing localization in an external magnetic field in contrast to an ordinary 2D electron gas [40]

Similar spin resolved ARPES measurements were performed on the W(110) surface [20]. They revealed high spin polarization in the surface bands. For spin measurements with a traditional Mott detector, photoemission was excited with a He discharge lamp at hν = 21.2 eV. As a consequence of the low efficiency of both ARPES and Mott detector approaches, energy and angular resolution were sacrificed for shorter measurement time. They were set to 100 meV and 2°, respectively. The spin polarization P was calculated from $I_L$ and $I_R$ observed intensities of electrons scattered to the left and right.

The spin structure was measured for the "heavy" $\overline{\Gamma N}$ and "massless" $\overline{\Gamma S}$ direction, represented in Fig. 2.4(a) and (b) respectively. The crossing state S1 in the centre shows high spin polarization. Both branches of the S1 band in this section are not doubled but rather contain only one spin polarization. This is observed for both mutually orthogonal sections. In the $\overline{\Gamma S}$ section the S1 band dispersing to both sides from the crossing point approaches band A.

Here S1 shows breaks due to avoided crossing and hybridizes with band A, bending to lower energies at higher k, as schematically shown in Fig. 2.4(c). The same feature is observed on the other side from state A, when following band S1' from the Fermi level to lower energies. Here S1' breaks bending to higher energies when going to lower k values.

A simple model calculation assuming anisotropic Rashba constants presented in Fig. 2.4(d) showed strong anisotropy of the S1 state 20 meV above the crossover point. The exact spin direction is found to be oriented predominantly in plane, in the direction of band dispersion [19]. This feature of spin structure is similar to those of known topological insulators. But together with the strongly elongated elliptical shape in W(110) it shows predominant spin orientation along the $\overline{\Gamma N}$ direction. Such a spin orientation is interesting.

An electric current passed along an edge of such a system in $\overline{\Gamma N}$ direction must exhibit a remarkable spin polarization [17].

The expressed behavior is nicely reproduced by theoretical calculations performed by Mirhosseini el al. [17]. The calculated electronic structure shown in Fig. 2.5 confirms the observed high spin polarization. In the calculation it reaches 100%.

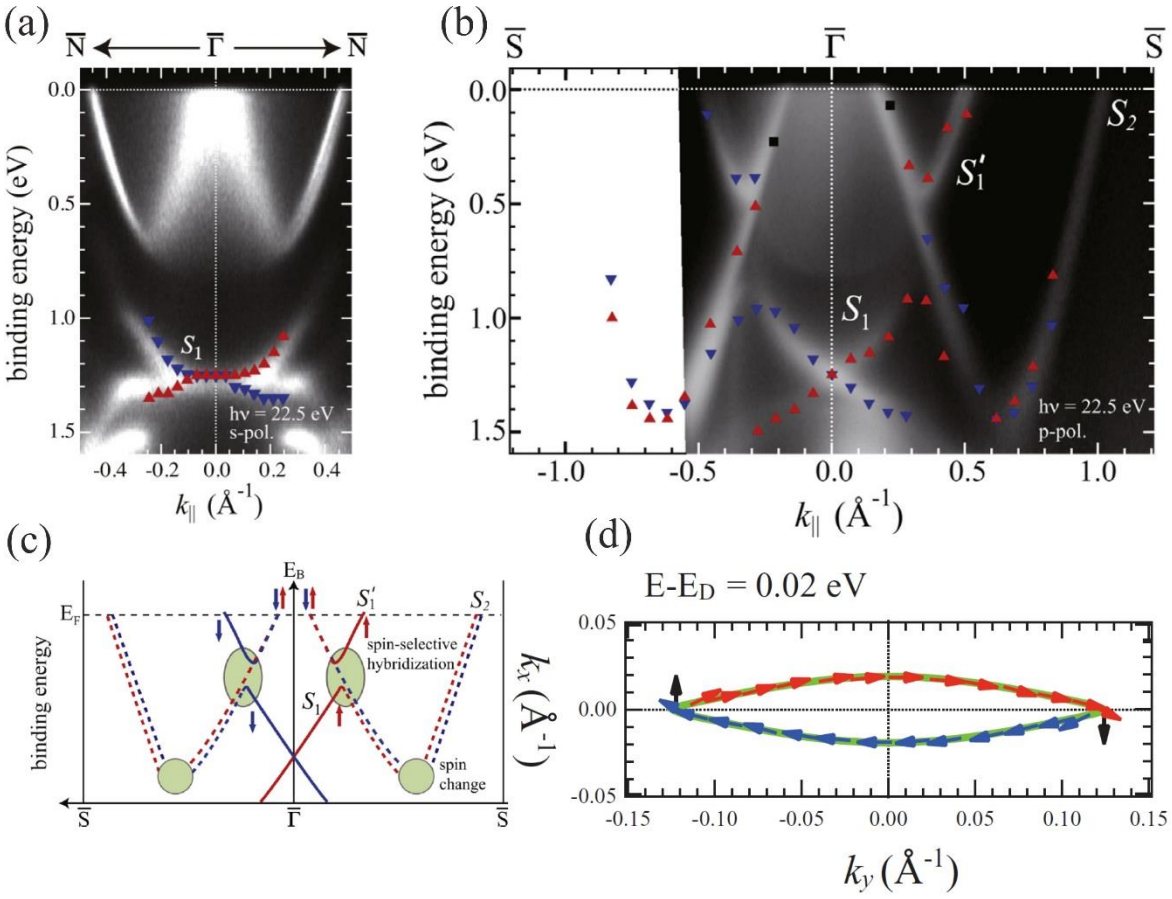


**Fig. 2.4.** Spin ARPES results along the $\bar{\Gamma}-\bar{N}$ and $\bar{\Gamma}-\bar{S}$ directions (a) and (b), respectively. Red and blue triangles denote opposite spin polarizations. Schematic sketch of band dispersion along the $\bar{\Gamma}-\bar{S}$ direction for S1, S1' and S2 bands (c). Calculated spin texture of the S1 state in the constant-energy section 20 meV above the crossing point (d). (From Miyamoto et al. [16, 19])

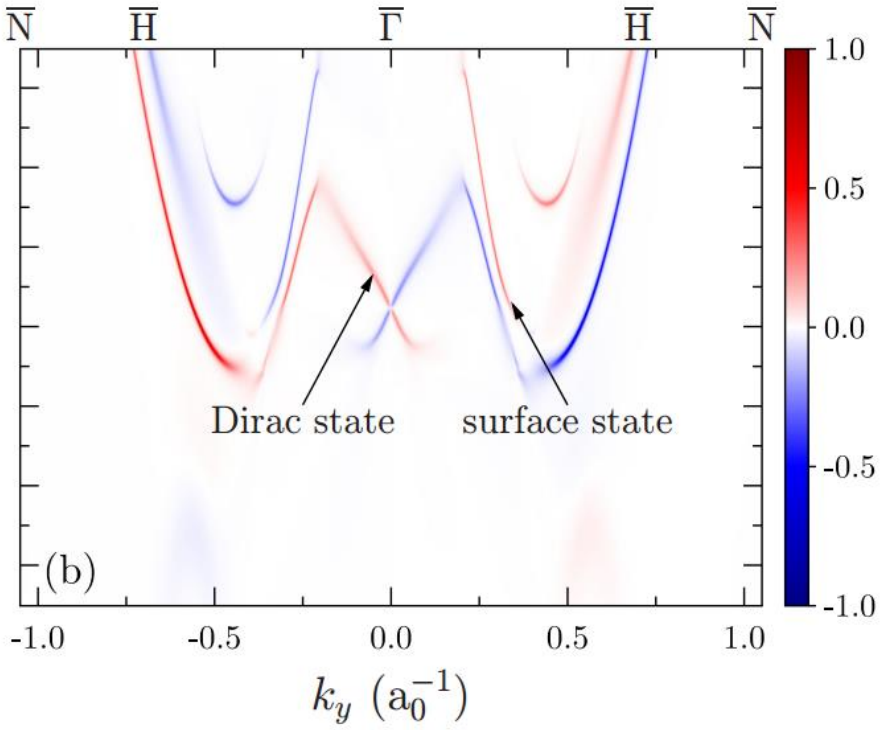


**Fig. 2.5.** Calculated spin-resolved electronic structure of the surface layer of W(110) along $\bar{\Gamma} - \bar{\mathrm{H}}$. The spin quantization axis is normal to the wavevector. The false-color bar denotes the degree of spin polarization. (From Mirhosseini el al. [17])

## 2.2. Theoretical explanation and calculation for W(110)

The anomalous state is situated in a partial band gap created by the spin–orbit coupling. Quite the same is observed in a topological insulator, although, there the spin-orbit interaction causes a fundamental band gap. In a topological insulator true Dirac states are formed in a practically isotropic two-dimensional electron gas, the Dirac state of W(110) is highly anisotropic. It shows linear (i.e. Dirac-like) dispersion in one direction and almost no dispersion along the orthogonal direction. This correlates with the twofold symmetry of the W(110) surface [19]. The discovery of a "Dirac surface state" on W(110) was surprising and needed a theoretical implementation in order to better understand its origin and properties.

It was found that model Hamiltonian calculations allow for a comprehensive theoretical study of Rashba-split surface states in systems like Au(111) [41] and bichalcogenide topological insulators [42]. For W(110) this approach was implemented [17] taking into account the twofold surface symmetry (point group 2*mm* [43]). Corresponding Hamiltonians were derived from ***k p*** perturbation theory [44]:

$$H = H_0(\boldsymbol{k}) + H_{soc}^{(1)}(\boldsymbol{k}) + H_{soc}^{(3)}(\boldsymbol{k}),\ \boldsymbol{k} = (\boldsymbol{k}_x, \boldsymbol{k}_y), \tag{2.1}$$

where $H_0(\boldsymbol{k})$ is the basic Hamiltonian of an anisotropic two-dimensional electron gas without taking into account spin–orbit coupling. $H_{soc}^{(1)}(\boldsymbol{k})$ and $H_{soc}^{(3)}(\boldsymbol{k})$ are the Rashba-type spin–orbit Hamiltonian in first and third order [17].

$$H_0(\boldsymbol{k}) = \frac{\hbar k_x^2}{2m_x^*} + \frac{\hbar k_y^2}{2m_y^*}, \tag{2.2}$$

$$H_{soc}^{(1)}(\boldsymbol{k}) = \alpha_x k_x \sigma_y + \alpha_y k_y \sigma_x, \tag{2.3}$$

$$H_{soc}^{(3)}(\boldsymbol{k}) = \alpha_{x^3} k_x^3 \sigma_y + \alpha_{x^2y} k_x^2 k_y \sigma_x + \alpha_{xy^2} k_x k_y^2 + \sigma_y \alpha_{y^3} k_y^3 \sigma_x, \tag{2.4}$$

($\alpha_{x^3}$ = 5.57 eV Å$^3$, $\alpha_{x^2y}$= 12.3 eV Å$^3$, $\alpha_{xy^2}$= –25 eV Å$^3$, and $\alpha_{y^3}$= 1.13 eV Å$^3$).

This Hamiltonian differs considerably from the Hamiltonian for three-fold (111) surfaces [45], [46]. Time reversal symmetry forbids the out-of-plane spin component for a two-fold symmetry surface. Therefore, the spin polarization vector ***s*** has to be in-plane for all wave vectors. However, the measured out-of-plane component of the photoelectron spin polarization can be non-zero because the photoemission process breaks the time-reversal symmetry. Hence some restrictions induced by theory are lifted in experiment.

For the calculations, the entire system was divided into three regions. (1) semi-infinite bulk, (2) the surface region that was constructed of six layers of W atoms and four “layers” of vacuum (necessary to model the surface barrier) and (3) the semi-infinite vacuum region. The surface layer is relaxed toward the bulk by -2.75% of the normal interlayer distance. This value is taken from the surface x-ray diffraction experiments [31]. This value coincides well with the value obtained from LEED experiments [47].

The spin- and angle-resolved photoemission intensity can be calculated within the relativistic one-step model[48,49].

All in all, the expressed model takes into account the most important aspects of the electronic structure and photoemission process. It considers the correct boundary conditions, the electronic structure above the vacuum level (so called time-reversed LEED state), dipole selection rules (via the dipole operators), and the electronic structure of the occupied states. The in-plane wave vector k is conserved due to translational invariance within the layers.

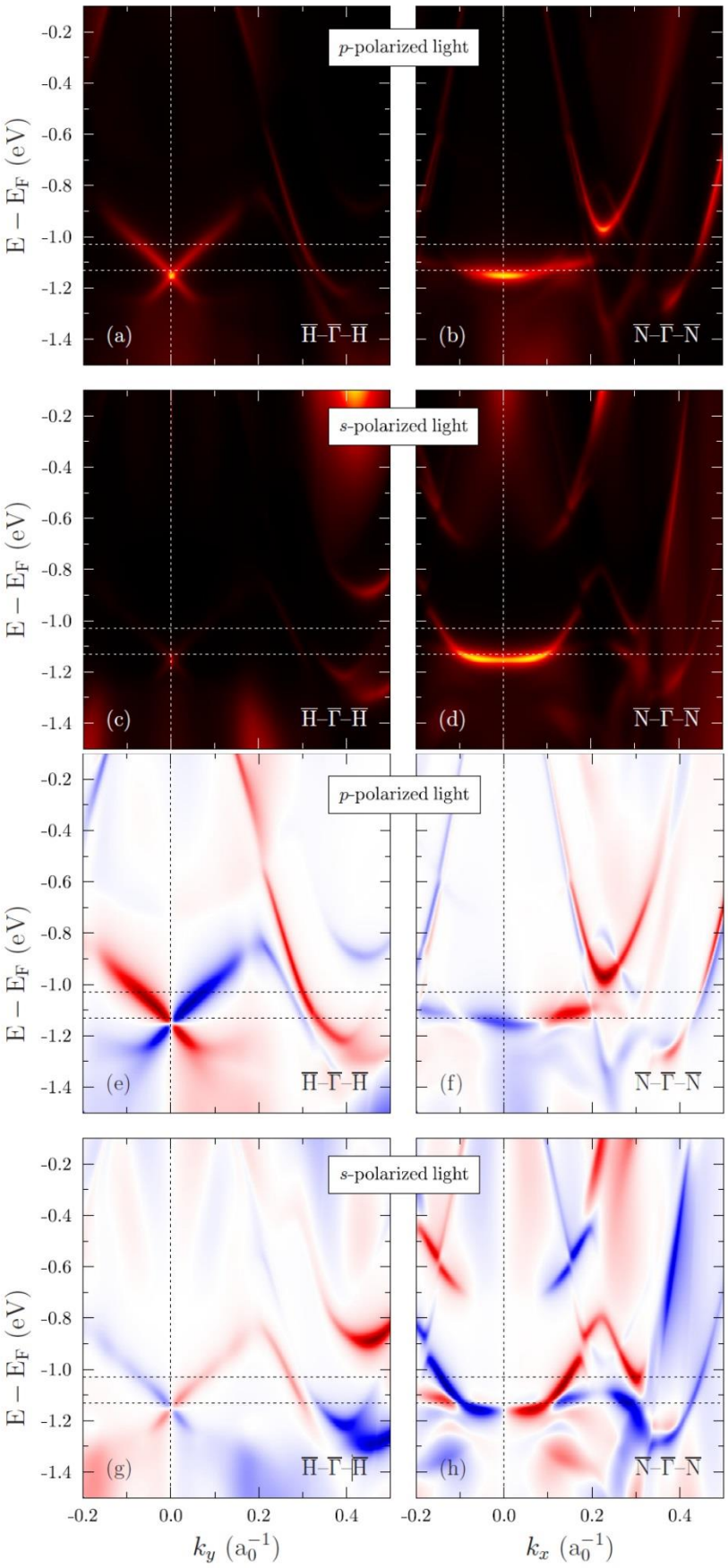


**Fig. 2.6.** Calculated spin-integrated (a-d) and spin-resolved (e-h) ARPES intensities from W(110) along $\overline{\mathrm{N}}\overline{\Gamma}$ and $\overline{\mathrm{H}}\overline{\Gamma}$ directions at $h\nu$=22.5 eV. (From Mirhosseini el al. [17])

In most cases, the calculated photoemission pattern (Fig. 2.6) coincides well with the observed experimental results, shown in Fig. 2.1. The calculation for bulk layers reveals a pocket-shaped partial band gap induced by spin-orbit coupling. Calculations for the topmost surface level shows a marked signat ure at a binding energy of 1.15 eV. This signature confirms linear dispersion at the crossing point along $\overline{\mathrm{H}} - \overline{\Gamma} - \overline{\mathrm{H}}$ and almost flat ("heavy") dispersion along $\overline{\mathrm{N}} - \overline{\Gamma} - \overline{\mathrm{N}}$.

The calculation reproduces the avoided crossing behavior between the Dirak-like band and the surface state B, see Fig. 2.1. The latter is associated with the edge of the bulk band. Consequently, the Dirac-state does not cross the band gap being locked within the bulk band by the surface state A. Both states belong to the same irreducible representation of the small group of k and, therefore, cannot cross for symmetry reasons.

Surface bands blur when they overlap with bulk bands due to hybridization. The anisotropy of the Dirac state's dispersion shows the importance of the third-order terms in the model Hamiltonian.

As was discussed above, the spin alignment is in-plane. In accordance with Mirhosseini et al. it points orthogonal to k [17]. The in-plane spin polarization of the photoelectrons with respect to the quantization axis normal to k is shown in Fig. 2.6 (lower 4 panels). The Dirac state S1 exhibits the expected spin texture which conforms with that derived from the model Hamiltonian. Interestingly, the surface state A that hybridizes with S1 has an opposite spin orientation. According to the calculations the spin polarization of the Dirac state reaches almost 96% at a binding energy of −1.07eV.

With the observation of a Dirac-like surface state on a metal surface, spin–orbit-induced phenomena opened a new field for investigations. In the present Thesis the related case of Mo(110) has been investigated.

## 2.3. Calculation for Mo(110)

Parallel to the experimental work of this thesis, a calculation for Mo(110) has been performed by Braun, Minár, Borek and Ebert (TU München). Their spectroscopic analysis is based on the fully relativistic one-step model in its spin-density matrix formulation. This approach allows describing properly the complete spin-polarization vector in particular for Rashba systems. Here we present the theoretical chapter of the joint publication [50].

The spin-density matrix of the photocurrent is defined by the following equation [51]:

$$\bar{\rho}_{SS'}^{PES}(\boldsymbol{k}_{\parallel},\varepsilon_f) = \langle S,\varepsilon_f,\boldsymbol{k}_{\parallel}|G_2^+\Delta G_1^+\Delta^+ G_2^-|\boldsymbol{k}_{\parallel},\varepsilon_f,S'\rangle. \quad (2.5)$$

It follows then for the spin-density matrix:

$$\rho_{SS'}^{PES}(\boldsymbol{k}_{\parallel},\varepsilon_f) = \frac{1}{2i}\left(\bar{\rho}_{SS'}^{PES}(\boldsymbol{k}_{\parallel},\varepsilon_f) - \bar{\rho}_{S'S}^{*PES}(\boldsymbol{k}_{\parallel},\varepsilon_f)\right). \quad (2.6)$$

The intensity of the photocurrent results in:

$$I^{PES}(\boldsymbol{k}_{\parallel},\varepsilon_f) = Sp\left(\rho_{SS'}^{PES}(\boldsymbol{k}_{\parallel},\varepsilon_f)\right), \quad (2.7)$$

and the corresponding spin-polarization vector is given by:

$$\boldsymbol{P} = \frac{1}{I} Sp(\sigma\cdot\rho). \quad (2.8)$$

Finally, the spin-projected photocurrent is obtained from the following equation:

$$I_{\boldsymbol{n}}^{\pm PES} = \frac{1}{2}(1 \pm \boldsymbol{n}\cdot\boldsymbol{P}). \quad (2.9)$$

The spin polarization is calculated with respect to the vector $\boldsymbol{n}$. This, for example, allows the complete calculation of all three components of the spin-polarization vector for each pair of ($k_x$,$k_y$) values which define the coordinate system for momentum images. Within this formalism $I^{\mathrm{PES}}$ denotes the elastic part of the photocurrent. Vertex renormalizations are neglected. This excludes inelastic energy losses and corresponding quantum-mechanical interference terms [52-54]. Furthermore, the interaction of the outgoing photoelectron with the rest system is not accounted for, which means that the so-called sudden approximation has been applied. This approximation is expected to be justified for not too small photon energies. The initial and final states are constructed within spin-polarized low-energy electron diffraction (SPLEED) theory, where the final state is represented by a so-called time-reversed SPLEED state [49, 55]. Many-body effects are included phenomenologically in the final-state calculation, using a parameterized, weakly energy-dependent and complex inner potential as was performed by Pendry et al. [56]. This generalized inner potential accounts for inelastic corrections to the elastic photocurrent [53] as well as the actual (real) inner potential, which serves as a reference energy inside the solid with respect to the vacuum level [57-59]. Due to the finite imaginary part, the inelastic mean free path is simulated and thus the amplitude of the high-energy photoelectron state can be neglected beyond a certain distance from the surface.

Self-consistent electronic structure calculations were performed within the *ab-initio* framework of spin-density functional theory. The Vosko, Wilk, and Nusair parameterization for the exchange and correlation potential was used [58]. The electronic structure was calculated in a fully relativistic mode by solving the corresponding Dirac equation. This was achieved using the relativistic multiple-scattering or KKR formalism in the TB-KKR mode [60, 61]. The resulting half-space electronic structure, represented by single-site scattering matrices for the different layers and the corresponding wave functions for initial and final-state energies, were used as input quantities for the corresponding photocurrent calculations. The self-consistent half-space electronic structure calculation had been performed for the Mo(110) surface accounting for the inward relaxation of the first atomic layer. The relaxation value of 5% had been taken from literature [62]. For the photoemission calculations, three vacuum layers were added to the semi-infinite half-space of atomic layers. In addition, the surface itself was taken into account by use of a Rundgren-Malmström-type surface potential [63], which can be easily included into the formalism as an additional layer. This procedure allows for the correct description of the asymptotic behavior. As this surface barrier represents a z-dependent potential, a surface contribution as part of the total photocurrent results, which accounts explicitly for the energetics and dispersion of all surface features. Furthermore, the relative intensities of surface-related spectral distributions are quantitatively accounted for by calculating the corresponding matrix elements in the surface region. This procedure is described in detail, for example, in [64, 65]. Also, energy and momentum conservation are naturally included in the formalism [66, 49].

To deal with impurity scattering, a small constant imaginary value of $V = 0.01$ eV was used for the initial state, thus describing the finite life-time of the initial state. Life-time effects in the final state are accounted for by the imaginary part of the inner potential. A constant imaginary value of $V = 1.5$ eV has been chosen again in a phenomenological way for excitation energies in the ARPES regime. According to the experimental setup, the spectroscopic calculations were performed by use of linear p-polarized light with a photon energy of $h = 35.0$ eV. The polar angle of the incoming photon beam was fixed to 68° with respect to the surface normal for all calculations, where the azimuth angle was defined by either the $\overline{\Gamma N}$ or the $\overline{\Gamma H}$ direction, which represent the two high-symmetry directions existing on the Mo(110) surface. All constant energy surface (CES) calculations were made twice for binding energies ranging from $E_F$ to 1.8 eV below $E_F$ with a step width of 0.05 eV. The corresponding dichroic signal was then extracted from each CES-intensity pattern as described in Sect. 5.3.

As the incoming light is partially absorbed by a metal surface, the index of refraction is normally complex. In the general case, the linearly polarized photon beam is transformed to elliptically polarized light, where the corresponding components of the vector potential are determined by the Fresnel equations [67]. The corresponding dielectric response is then described in a phenomenological sense within a macroscopic dielectric constant $\varepsilon(\omega)$, since the most simple approximation of the dielectric constant has been chosen real with a value of ε(35eV) = 0.7 in our spectroscopic analysis. Finally the Fermi level has been renormalized by a rigid energy shift of 0.15 eV to account for a well-known shortcoming of the LDA approximation [68].

It should be noted that many-body effects are neglected for the calculations. In particular many-body interactions caused by electron-phonon coupling, as well as by electron-electron scattering, lead to a finite lifetime of a valence photohole and are reflected by the quasi-particle self-energy. In the case of electron-electron scattering the inverse lifetime increases proportional to $E_B^2$ ($E_B$ binding energy) at low temperatures [69] leading to a quadratic increase of the total peak width with increasing binding energy. For the surface state in Mo(110) Valla et al. [70] found an additional broadening of 40 meV at $E_B$ = 0.4 eV. The electron-phonon coupling leads to an energy-independent broadening that linearly increases with temperature. For the Mo(110) surface state a value of 60 meV was reported for $T$ = 70 K [70]. In a very narrow energy region, near the Fermi level ($E_B < E_{Debye}$) the electron-phonon interaction leads to a linear decrease of the inverse lifetime with decreasing binding energy. Also, there is an enhancement of the effective mass of the electron.

Fig. 2.7 shows the calculated surface bands along the $\bar{\Gamma} - \bar{H} - \bar{\Gamma}$ direction in Mo(110) (a) and their spin texture (c) in comparison with the analogous resonance on W(110) (b and d). The red–blue color code quantified by the color bar denotes the Rashba spin component, perpendicular to the momentum vector. In both cases high degrees of spin polarization occur that depend on photon-polarization orientation, see also[16-20]. The color maps are based on a standard tight-binding (TB-SPRKKR) calculation where the electronic structure results from a fully relativistic self-consistent calculation for a semi-infinite stack of atomic layers. Dark grey levels indicate high spectral intensities. Details of the calculation for W(110) are given in [18].

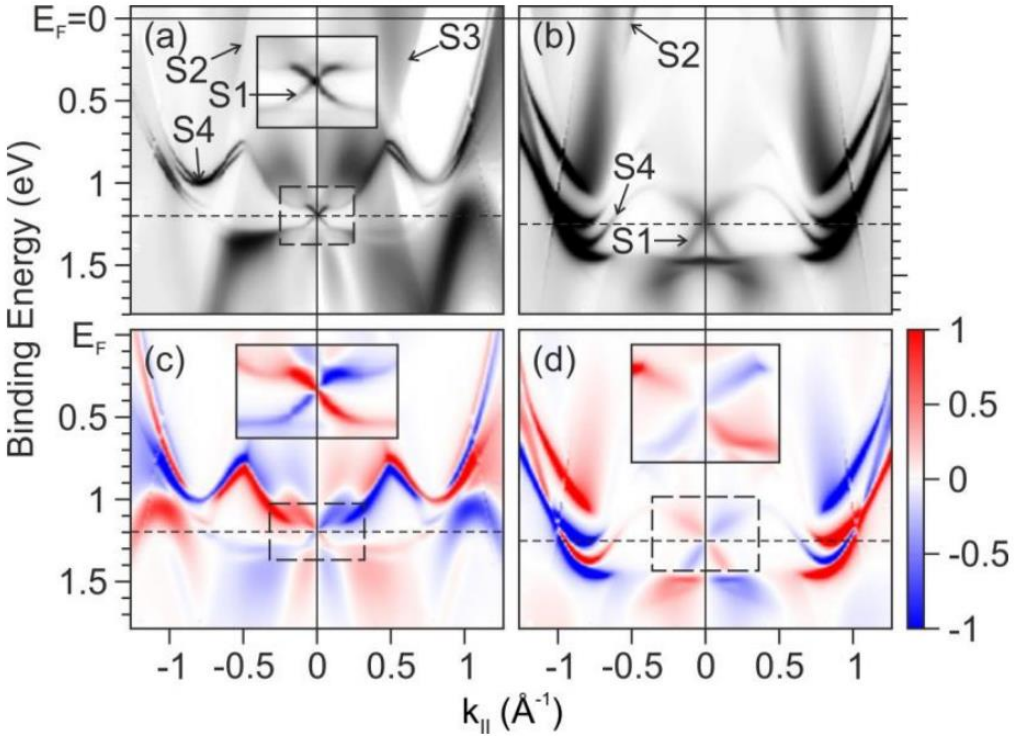


**Fig. 2.7.** Surface states and resonances S1–S4 along the $\bar{\Gamma} - \bar{H} - \bar{\Gamma}$ line on the Mo(110) surface (a and c) in comparison with the analogous states for W(110) (b and d). Photoemission calculations are for s-polarization (right half of (a), (b–d)) and p-polarization (left half and inset in (a), insets in (c and d)) at 68° impact angle. The band crossings at 1.2 eV in Mo(110) (a) and 1.25 eV in W(110) (b) exhibit "Dirac-like" signature and Rashba spin texture, color coded as shown in the color bar (d). Marked dashed rectangles are shown enlarged as insets. Despite the smaller spin-orbit interaction in Mo, the bandgap at $\boldsymbol{k}_{\parallel} = 0$ exists and is crossed by the linearly dispersing surface resonance S1 (a); bulk continua above and below the gap appear in darker grey. (From [50])

For Mo(110) the total gap at Γ has a width of 120 meV and extends from 1.16 to 1.28 eV below $E_F$. The continuum of bulk bands above and below the gap appear in grey. The gap is crossed by a linearly-dispersing surface state that shows a crossing at 1.2 eV and clear Rashba-type spin texture with high spin polarization of about 60% (c). This anomalous band is the equivalent of a similar band found by Miyamoto et al. [16] for W(110). We adopt the labeling from [16] i.e. the anomalous band which crosses $\bar{\Gamma}$ is labeled S1 and the outward dispersing band is S2. The band which runs along the bulk continuum with approximately parabolic shape is S3. A further, eye-catching feature is S4, a spin–orbit split band crossing the total part of the gap with a zigzag course. The anomalous band S1 has the same dispersion and spin signature as a Dirac-state in a topological insulator, so we term it "Dirac-like"

(keeping in mind that the band occurs on a metal). Due to the small gap size, S1 enters the continuum of bulk states at the upper end of the band gap. Hybridization with bulk states leads to substantial broadening, but the state persists in the bulk continuum (dark diffuse area) and shows a maximum at $\boldsymbol{k}_{\parallel} \approx 0.3$ Å$^{-1}$. In W the spin–orbit interaction is much larger, hence the gap is wider and the Dirac-like state does not enter the bulk continuum. Instead, it connects directly to one of the downward dispersing spin–orbit split bands S4. Since it persists in the bulk continuum, S1 has the character of a surface resonance. The Dirac-like dispersion behavior is exceptional for surface states on metals. The anomalous band seems to exist for simple metals only on these two surfaces. The symmetry character is d-like, whereas topological surface states typically have sp-like symmetry. Despite their similarity, these surface resonances cannot belong to the same topology class because of the missing total gap, which does not exist around the crossing point.

# 3. Momentum microscopy: a novel approach to electronic band mapping

## 3.1. Photoemission

Since the discovery and explanation of the photoelectric effect it became an important phenomenon for applications. It is exploited in image sensors (including IR or night-vision devices), photon multipliers, solar cells (so-called internal photo effect), etc. In science it is widely used for the investigation and characterization of solids, liquids, and gases. In 1905, Albert Einstein proposed an explanation of the photoelectric effect based on the assumption, which was in agreement with the previously discovered Planck relation, that light acts as a collection of wave packets of energy E= hν, where ν is the frequency and h is the Planck constant. According to Einstein's photoelectric effect formula, the maximum kinetic energy of an ejected electron is:

$$E_{\max} = h\nu - \Phi, \tag{3.1}$$

where $\Phi$ is the work function. The latter is the minimum energy required to bring an electron from matter into vacuum and for metals it equals the difference between the vacuum and Fermi energy levels.

Illuminating a surface with $h\nu > \Phi$, electrons are emitted with different kinetic energies starting from $E_{\max}$ to 0. In this case the term of binding energy $E_B$ appears (usually referred to the Fermi energy) and the exact kinetic energy of a photoelectron is:

$$E_{\mathrm{kin}} = h\nu - \Phi - E_{\mathrm{B}}. \tag{3.2}$$

Fig. 3.1 shows a schematic view of a photoemission spectroscopy experiment [71].

Photoelectron spectroscopy allows for investigation of both bulk and surface electronic structures. An example of a wide-range spectrum is shown in Fig. 3.2. Probing depth depends on the electron inelastic mean free path length (IMFP). The latter is a function of the electron energy and thus depends on the excitation photon energy (Fig. 3.3). Probing depth is very large for both very low and high energies. In the region between 20 and 200 eV, the IMFP is <1 nm thus making the study very surface sensitive[72,73]. In order to conduct bulk sensitive measurements, hard X-ray photoelectron spectroscopy is used. At these energies, the probability of electron excitation by an incoming photon becomes more than two orders of magnitude smaller requiring sufficiently high photon flux [74].

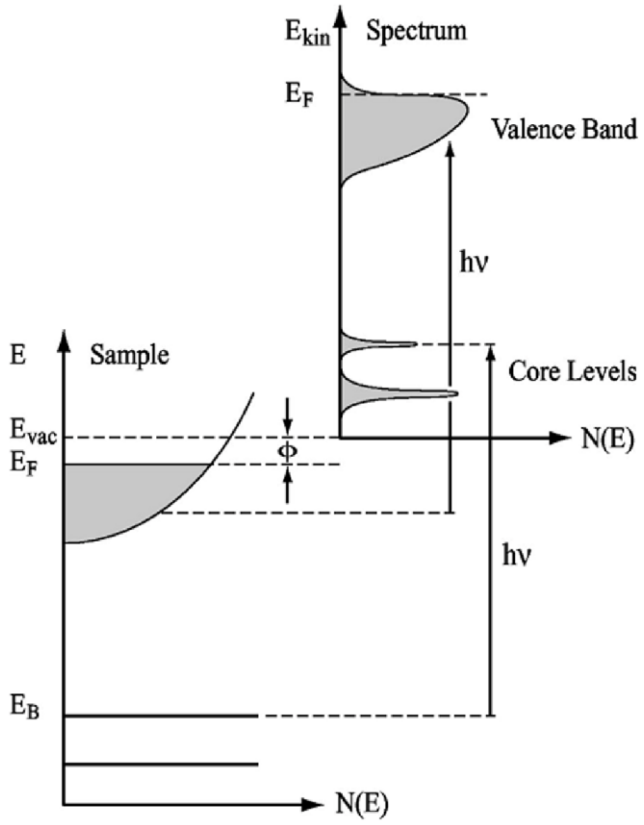


**Fig. 3.1.** Energy level scheme of photoemission (schematic). The photoelectron energy distribution after excitation represents the density of states inside the solid. (from [71])

Theoretically the photoemission process naturally can be described by a three-step model, schematically shown in Fig. 3.4 [75].

It assumes the following three steps:

- Photoelectron excitation inside the solid (by energy transfer from a photon);
- Travel of the photoelectron to the surface;
- Transmission of the photoelectron through the surface into vacuum.

Then the electron emission current is proportional to the product of probabilities of all three steps $P(E_k, hv) \cdot T(E_k, hv) \cdot D(E_k)$, respectively. With this approach, the information about the electronic bands and density of states in the solid is coded in the first term.

In a more recent approach, the photoemission process is treated as a one step process. Within this model an electron from a Bloch state is excited into a so-called time-reversed LEED state, which has a certain lifetime in the crystal [76].

Intensity, dichroism effects and spin polarization of photoelectrons are governed by the transition matrix elements.

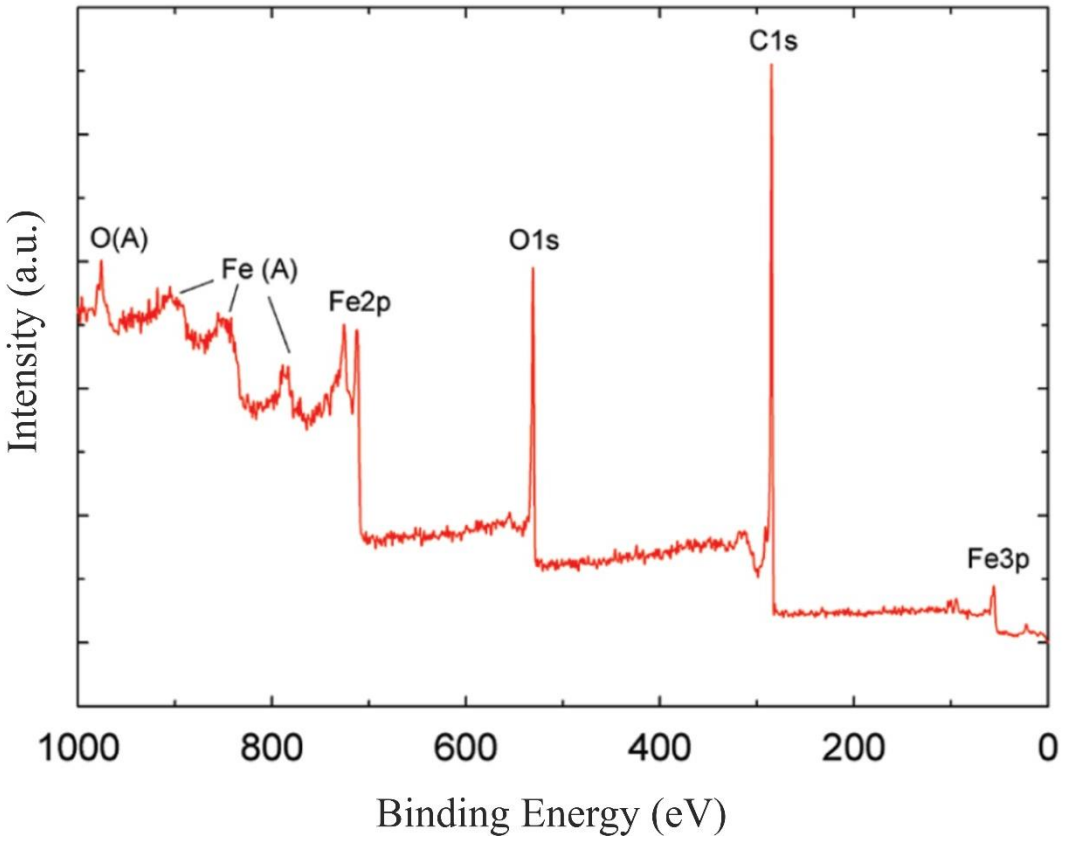


**Fig. 3.2.** X-ray photoelectron survey spectrum of multiwalled magnetic carbon nanotubes with maghemite nanoparticles (MWNT/γ-$Fe_2O_3$) taken with 0-1000 eV photons energy. (from [77])

Effects originating from matrix elements can be divided into four groups [75].

1. Orbital and *hυ* dependence of the photoionization cross-sections.

2. Polarization dependence of the observed spectra with respect to the photoelectron angular distribution, reflecting the selection rule between the initial and final states based on the idea that the photoexcitation is essentially an electric dipole transition.

3. hν dependence of the observed spectral line shape due to the effects of the energy dependence of the photoexcited final states deviating from the nearly-free-electron state.

4. Photoelectron diffraction effects reflecting the spatial configuration of neighbouring sites around the emitter atom.

The third point becomes important when working with low photon energies (<100eV) as the deviation of the final state from the quasi-free-electron state becomes large. The second point, with consideration to the experimental geometry, is important for experimental application reflecting the symmetry of initial and final electron wave functions.

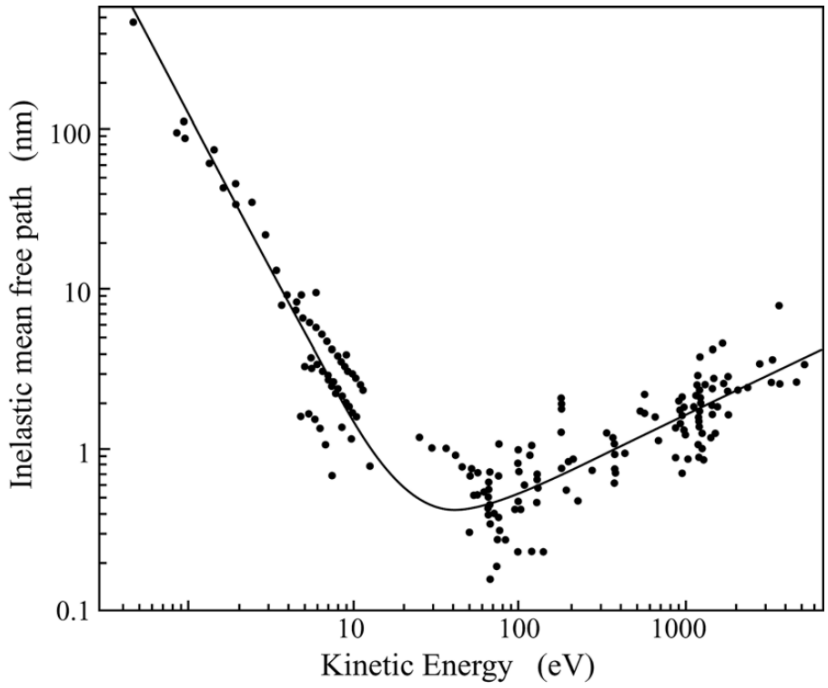


**Fig. 3.3.** Mean free path of electrons in solids depending on the electron energy above the Fermi level. The dots represent measurement on different elements and compounds. (from [73])

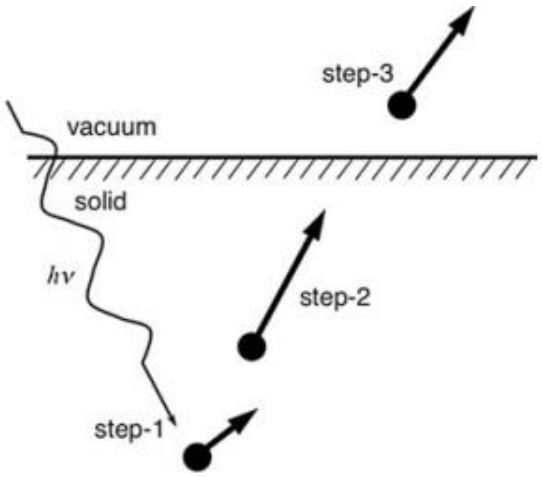


**Fig. 3.4.** Photoemission process as considered by the three-step model. (from [75])

In addition to energy resolution in photoemission spectroscopy, the angle of electron emission plays an important role. As the photon momentum in the low-energy range is negligible in comparison to the electron momentum, the photon-induced transition does not change the electron momentum, except for a reciprocal lattice vector $\boldsymbol{G}$. In the $E$ and $k$

(electron wave vector) coordinates, it is called vertical transition and keeps the information about the initial electron momentum, as schematically shown in Fig. 3.5. Another important point is that during the photoemission process the momentum component parallel to the sample surface stays constant. Constant electron parallel momentum and the change of perpendicular momentum affect the photoemission angle. All this enters into the angular and energy distribution of the emitted electrons representing the electron band structure of the sample.

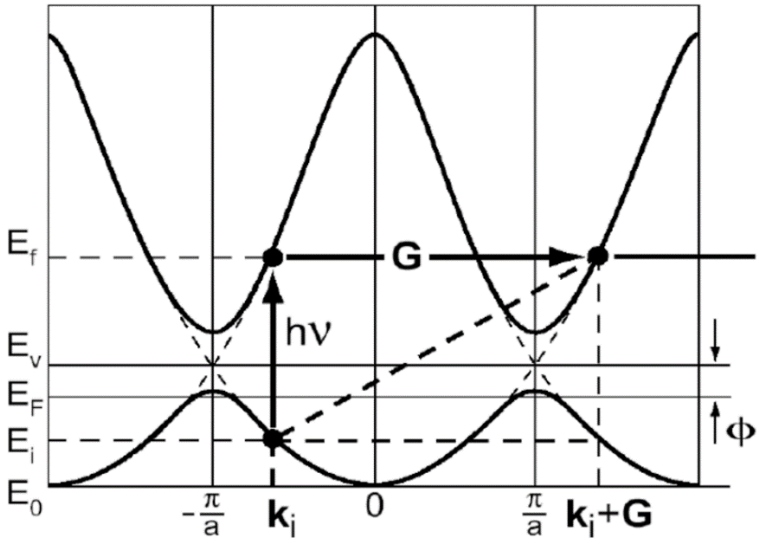


**Fig. 3.5.** Schematic representation of an electron transition (direct transition) between two states excited by a photon *hv*. Since a reciprocal lattice vector ***G*** is required to fulfil energy and momentum conservation, these processes are also called "umklapp"-processes. $E_0, E_i, E_F, E_v \; and \; E_f$ denote the bottom of the valence band, the initial energy, the Fermi energy, the vacuum level and final energy, respectively.

Angle resolved photoemission spectroscopy (ARPES) is a well-known technique for the investigation of the electronic structure of materials.

The short escape depth of electrons makes photoemission spectroscopy a powerful surface sensitive technique. Still it shows both surface and bulk electronic contributions. To distinguish between these two terms one needs to perform additional experiments. The easiest approach for this is to perform photoemission measurements at different photon energies from the soft to the hard X-ray regime to tune the electron IMFP and thus change the intensity ratio between surface and bulk contributions.

## 3.2. Basic principle of momentum microscopy

In the most simple and obvious way using the means explained in the previous chapter, the electron band structure can be probed with the help of ARPES. In this approach an electron spectrometer is located above the sample surface on a movable mount, allowing to change the polar and azimuthal detection angles (Fig. 3.6). The main drawback is the low efficiency of this technique. The angular (and momentum) resolution then depend on the electron acceptance angle and the energy resolution is reciprocal to the energy acceptance window. So, the accumulation and measurement speed is reciprocal to the resolution.

A more powerful approach to $\boldsymbol{k}_{\parallel}$-resolved photoelectron spectroscopy is called momentum microscopy. A principal scheme of a momentum microscope is shown in Fig. 3.7. The main element is an immersion objective electron lens operated at high voltages of typically 8 to 20 kV. Electrons released from the sample under excitation by photons are accelerated by the immersion field of the objective lens and focused with the focusing electrode onto a screen (not shown). Fig. 3.7 illustrates electron trajectories up to the formation of the first reciprocal image in the back focal plane of the lens. Electrons emitted parallel to the electron optical axis of the microscope are focused to a single point on the optical axis in the back focal plane. Other electrons, emitted at some angle to the axis end up at a different point, in the same plane but off-axis.

Let us further discuss the electron trajectories in this region. The electric field inside the gap between the sample and the lens is quite uniform with the gradient oriented along the lens axis. This determines several important properties of the lens. First of all, electrons are rapidly accelerated along the lens axis up to several keV kinetic energy. This makes the starting co-axial velocity negligible for electrons with energies up to several tens of eV. Thus it determines low chromatic aberrations for the lens.

The entrance angle of the electron is also reduced. An electron follows a parabolic trajectory and starting at an angle of $\alpha_0$ up to 90º with respect to the surface normal. The electron entrance angle is the smaller, the higher the acceleration voltage is. For electron starting energies much smaller than the final energy ($E_{st} \ll E_{st} + eU_{ex}$), the angle at which an electron enters the lens is much smaller, than the initial photoemission angle: $\alpha' \cong \alpha_0 \sqrt{E_{st}/(E_{st} + eU_{ex})}$. Strong coaxial acceleration speed leads to small $\alpha$ even for the fastest electrons (from the Fermi level) emitted far-off normal. This makes it possible to collect and image with low aberrations electrons from the whole $2\pi$ solid emission angle above the sample surface.

Moreover strong acceleration leads to negligible starting axial velocity, i.e. a low dependence of electron trajectories on perpendicular momentum ($\boldsymbol{k}_{\perp}$), when the sample surface is normal to the lens axis (Fig. 3.7). As a consequence the point where the electron hits the back focal plane of the lens, depends almost solely on the initial momentum parallel to the sample surface, i.e. the $\boldsymbol{k}_{\parallel}$. Therefore it is possible to refer to the image in the back focal plane as a momentum image of the sample. The $\boldsymbol{k}_{\parallel}$-scale remains constant for all kinetic energies of the electrons as long as $\sin\alpha' \approx \tan\alpha'$.

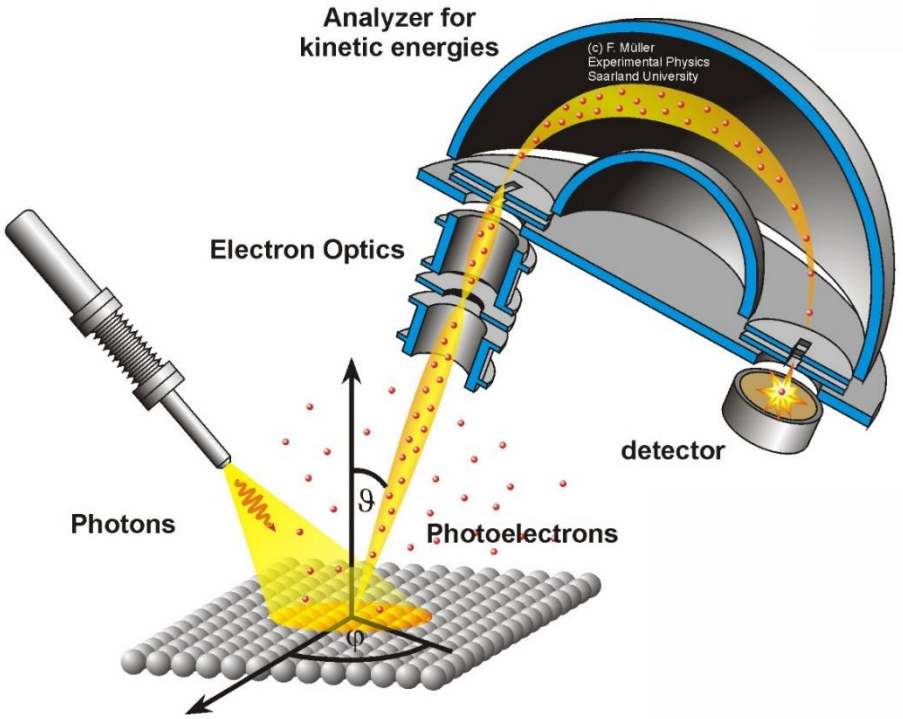


**Fig. 3.6.** Schematic arrangement of a conventional ARPES experiment. (From [78])

Further the momentum image from the back focal plane is magnified and transferred onto the screen by projective electron lenses. The scheme of a momentum microscope resembles that of an ordinary photoemission electron microscope (PEEM) but instead of the real image plane the back focal (also called diffraction, reciprocal, or momentum) plane of the objective immersion lens is projected onto the screen.

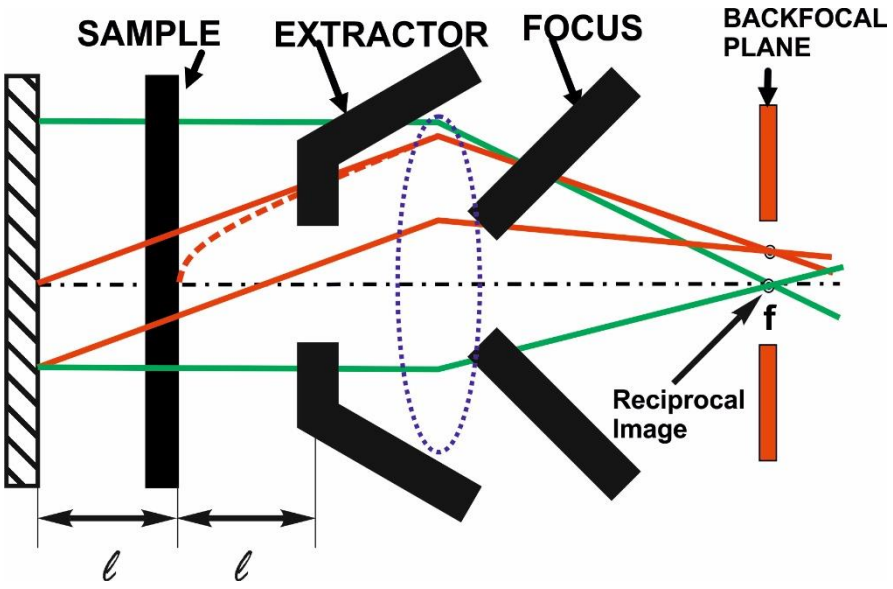


**Fig. 3.7.** Electron trajectories in the immersion electron objective lens for different starting angles and lateral positions on the sample (schematic). The hatched rectangle denotes the "virtual source".

The resolution of the momentum microscope depends on the same aberration factors as for a classical PEEM. The most important are chromatic and spherical aberrations and the diffraction limit making three major contributions to blurring of a spot (Fig. 3.8). It should be mentioned that there is no existing diverging electron lens, thus it is not possible to compensate lens aberrations by round lenses but only reduce them by improving the lens itself. Only multipole elements and electron mirrors can correct aberrations[79-81].

It is known that electron optics has lowest aberrations for electrons in the vicinity of the optical axis, i.e. low-angle electrons. Therefore spatial resolution gets worse with increasing $\alpha$. The spherical aberration of the acceleration field is expressed by the following formula.

$$\Delta l_{\mathrm{s}} \approx l\sqrt{\frac{E_0}{E_{\mathrm{acc}}}}\alpha^2 = C_{\mathrm{s}}^{\mathrm{acc}}\alpha^3. \tag{3.3}$$

Chromatic aberration of the acceleration field also depends on the angle according to the formula:

$$\Delta l_{\mathrm{c}} = -l\sqrt{\frac{E_0}{E_{\mathrm{acc}}}}\cdot\frac{\Delta E}{E_0}\cdot\alpha = C_{\mathrm{c}}^{\mathrm{acc}}\cdot\frac{\Delta E}{E_0}\cdot\alpha. \tag{3.4}$$

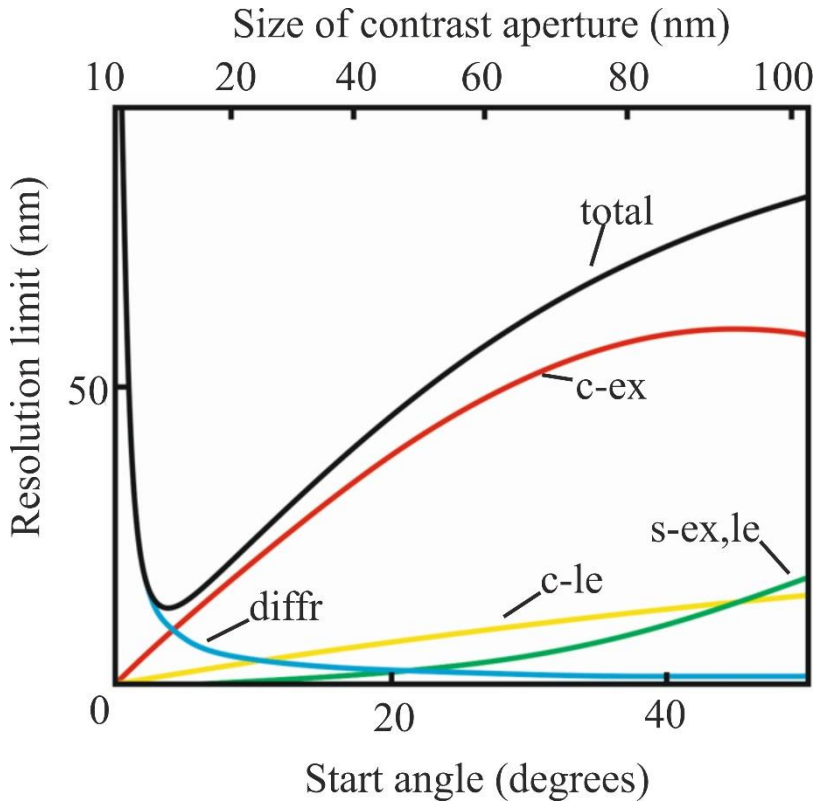


**Fig. 3.8.** Model calculation of the total real-space resolution (black line) of an optimized electrostatic cathode lens and different contributions to it. Chromatic aberration of the extractor field is denoted by red colour (c-ex). Chromatic aberration of the objective lens (c-le) is drawn in yellow. Spherical aberration of the extractor field (s-ex) and lens (s-le) are the green line. The blue line is the diffraction contribution (diffr), dependent on the size of the contrast aperture. For the calculations the extractor voltage was taken as 30 kV, starting energy 1.5 eV.

For the reciprocal image, an aperture placed in a real image plane will act similarly to a contrast aperture. The latter is often placed in the focal plane to cut off large-angle beams and improve resolution. However it is not possible to decrease the aperture size towards zero. In addition to the problem of low intensity, the diffraction limit comes into play. The size of a diffraction disc is estimated with the formula:

$$\delta_{\mathrm{d}} = 0.6\,\lambda/\alpha \cong 0.6\sqrt{1.5/E}\cdot\alpha^{-1}, \tag{3.5}$$

where for electrons:

$$E = \hbar^2 k^2/2m = (2\pi\hbar)^2/(2m\lambda^2) = 1.5[eV\cdot nm^2]/\lambda^2. \tag{3.6}$$

The total microscope resolution accounting for all three factors can be written as:

$$\rho_{\mathrm{tot}} = \sqrt{(c_{\mathrm{s}}\cdot\lambda^3)^2 + (c_{\mathrm{c}}\,\Delta E/E\cdot\lambda)^2 + (0.61\,\lambda/\alpha)^2}. \tag{3.7}$$

Here $E$ is taken in [eV], and $\lambda$, $\delta_{\mathrm{d}}$, $\Delta l_{\mathrm{s}}$, $\Delta l_{\mathrm{c}}$, and $\rho_{\mathrm{tot}}$ are in [nm]. Here, $c_{\mathrm{s}}$ and $c_{\mathrm{c}}$ are the aberrations of all lenses, not only of the acceleration field in eq. (3.3 and 3.4). For an extensive treatment of aberrations of combined system with many lenses, see e.g. [82]. Therefore to increase the resolution, it is necessary to decrease the starting energy of electrons and increase the acceleration-field voltage.

## 3.3. Momentum microscopy using a dispersive energy analyser

The idea of parallelization of ARPES measurements arose quite long time ago [83]. The natural way of energy filtering for momentum microscopy came from the already developed field of spectromicroscopy, of which momentum microscopy is a part. A hemispherical energy analyzer was found to be appropriate for the imaging energy filtering. This tool allows for a far superior energy resolution in comparison to a retarding field energy analyzer [84]. First we have a look at a hemispherical analyzer in the so-called $E-\theta$ mode, Fig. 3.9 [85]. In this case, the spectrometer works in the wide energy band mode. This means that instead of an exit slit there is a large open exit field of up to 20×40 mm. Electron deviations in the y-direction (orbit radius) from the center point are a result of different electron energies. Deviations in the x-direction are due to different entrance angles along x. Diverging angles along y also influence the detected y coordinate and thus the entrance slit is made in the shape of an elongated narrow slit: only a small interval along x (energy coordinate) but a large y-range (angular coordinate). At the exit of the analyzer, an installed 2D imaging detector (usually an MCP in combination with a fluorescent screen and a CCD camera) represents a 2D electron distribution in coordinates $E$ and $\theta_x$. The $E(k)$ 2D band structure is acquired by sequential measurements when scanning the sample tilt angle $\theta_y$.

The energy and $\theta_y$-resolution of such an analyzer is a function of the entrance slit width and hemisphere diameter [85].

$$\Delta E \cong E_0 \left(\frac{s}{2R}\right). \tag{3.8}$$

Where R is the analyzer radius, s is the slit width, $E_0$ the pass energy and $\Delta E$ the energy resolution of the detector. For the ideal case of a fine slit of 0.1 mm width and 1 eV pass energy, a standard analyzer theoretically can give an energy resolution of 0.25 meV at the expense of low signal intensity (<1 meV is stated to be achieved for SCIENTA R8000 spectrometer [86]). At the same time the $\theta_x$ acceptance angle range makes only $\pm 15°$

The formula (3.8) only holds for a beam with no divergence, entering at a perfectly defined angle. For finite angular acceptance $\alpha$ the resolution is further limited by spherical aberrations[87,88].

$$\Delta E \cong E_0 \left(\frac{s}{2R} + \alpha^2\right). \tag{3.9}$$

The $\alpha^2$-term is the spherical aberration of the electron analyser. From this formula it follows that good energy resolution ΔE requires either a small energy $E_0$ or a small width of the entrance slit d. Moreover the $\alpha^2$-term must be small enough by restricting the maximum electron divergence angle.

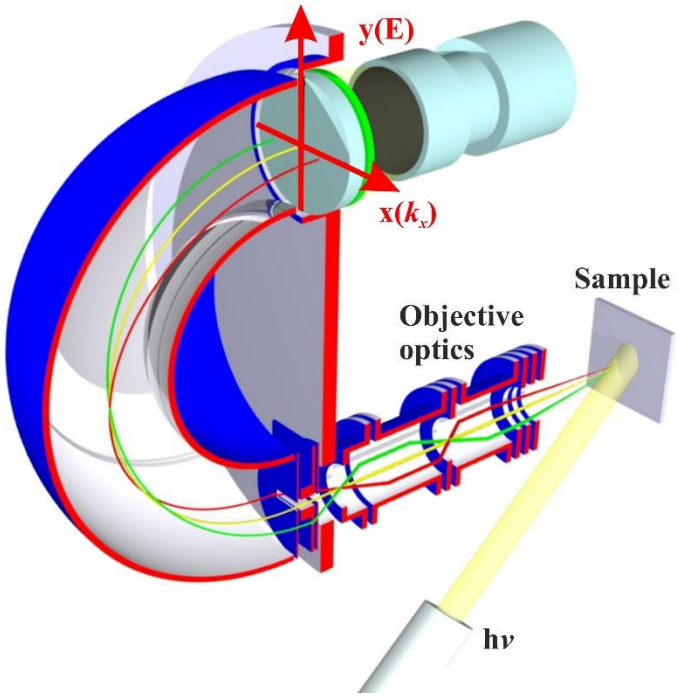


**Fig. 3.9.** Schematic representation of a hemispherical dispersive energy analyzer in the so-called $E - \theta$-mode of operation. (Adapted from [89]).

Another approach to energy filtering with hemispherical analyzers was used in the NanoESCA instrument, a joint development of Uni Mainz, Uni Saarbrücken (S. Hüfner, F. Reinert), Omicron GmbH and Focus GmbH [90]. It was first used for real space spectromicroscopy and then also used for momentum microscopy. To compensate the $\alpha^2$ aberrations in the spectrometer section a concept of two hemispherical analysers in tandem configuration was proposed (Fig. 3.10).

The action of the two hemispheres is illustrated in Fig. 3.10. In a spherical electrostatic field electrons circulate similarly to planetary motion and their trajectories repeat after a complete revolution, independent on the start energy and angle. This means that after $2\pi$ revolution a perfect achromatic image without aberrations of the input pattern is generated [91]. Because of symmetry reasons the second half of the elliptical orbit compensates the aberrations of the first half. The energy selecting slit is situated on the opposite side from the entrance slit after 180◦ revolution, the same as in case of a single hemispherical analyser. Here the largest energy dispersion occurs and thus the filtering is most effective. Due to steric reasons it is not possible to place an output slit in the same place as the input. In the NanoESCA this obstruction is solved by splitting of the sphere into two hemispheres and rearranging them as shown in the Fig. 3.10. One sphere is now put in an inverted orientation. The transfer optics between the two hemispheres is to invert the beam in between the spheres.

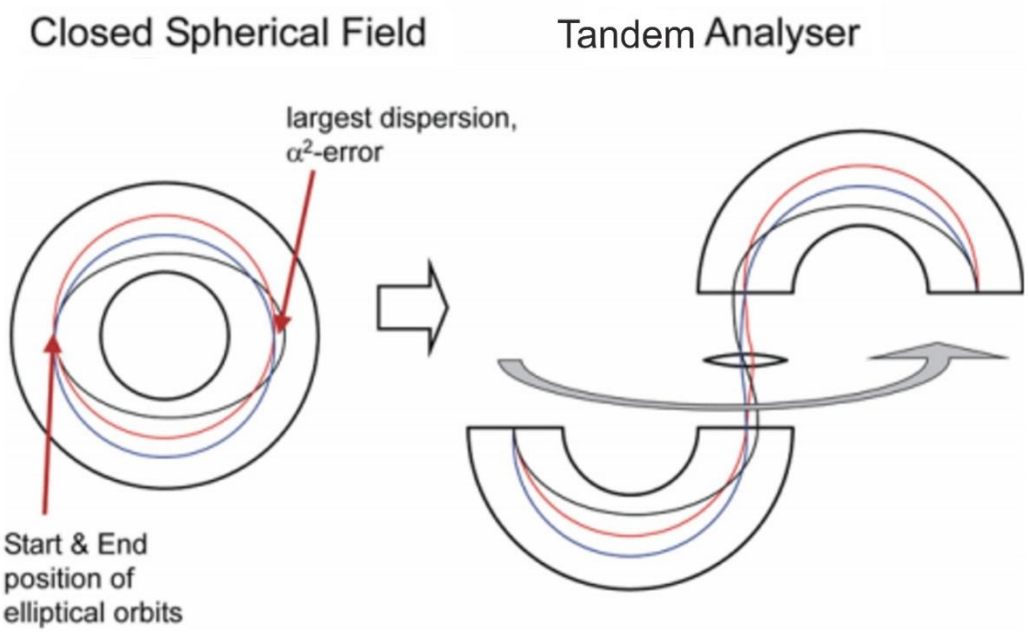


**Fig. 3.10.** Basic idea for the imaging double energy analyzer. Different colours denote different entrance angles of electrons with equal energy [90].

Only the first hemisphere serves for energy discrimination. So, the energy resolution of this tandem analyser is defined by the first hemisphere and the second is only to compensate further the angular aberrations of the obtained image. In practice it can be advantageous to run the two hemispheres in a mode without the inverting lens, so that the

dispersion of the two hemispheres adds up. In this way, the performance could be strongly improved in a new design [92].

For pump-probe or other time-resolved experiments, the time resolution of a device is a principal factor. In a hemispherical detector the travel time of electrons with different entrance angles are different. The time spread after a revolution of 180° $T_{180°}$ in the first approach can be written as [93]:

$$\frac{\Delta T}{T_{180°}} = \frac{3}{2}\frac{d}{R_0} + \frac{8}{\pi}\alpha \tag{3.10}$$

But for a complete ellipsoidal trajectory the transit time T of a particle with energy *E* is independent of the start angle $\alpha$ [94]:

$$T = \text{const}E^{-3/2}, \tag{3.11}$$

And particles with energy spread *dE* arrive to the exit of the analyser with time spread *dT:*

$$\frac{dT}{T} = -\frac{3}{2}\frac{dE}{E}. \tag{3.12}$$

Here the right part of the equation contains an expression for the energy resolution of the detector. In turn it can be determined as follows from the formula (3.9) [87]. Then for small slit size and electron angle from equations (3.12) and (3.9) we have:

$$\frac{\Delta T}{T_{360°}} = -\frac{3}{2}\left[\frac{d}{2R_0} + \alpha^2\right], \tag{3.13}$$

Where $T_{360°}$ is the time period of a full revolution. For a pass energy of 100 eV in a setup with a hemisphere radius of 124 mm, $T_{360°}$=186 ns. For a slit width of d=0.5 mm and maximum entrance angle of α =1.5°, the calculated time spread is ΔT ≈0.5 ns. Time resolution can be improved to below 100 ps, by decreasing the slit width and increasing the pass energy.

With compensation of travel times for inner and outer going beams, energy and time-resolved measurement can be performed using a time-resolved detector for image acquisition, e.g. a delay-line detector (DLD) [95].

The NanoESCA can work in two modes, real space and angular resolved mode. In the first case, it works as an ordinary PEEM with additional energy filtering and projection/retardation lenses, transferring the real image plane to the entrance of the analyzer. Furthermore, an energy filtered real space image is projected on the detector. In the second case the optics are tuned to do the same for the image in the back focal plane where, as we discussed above, the momentum image is formed. In the latter regime, a transfer lens is engaged to decrease the magnification of the first image plane and, in

accordance to Helmholtz Lagrange law, increase the angular magnification. The plane of the first real image contains an adjustable field aperture that confines the area on the sample contributing to the angular image. The achievable k-space resolution is better for a smaller field of view on the sample. However, the NanoESCA is optimized for real space resolution which comes at the expense of $k$-resolution.

Recently an improved momentum microscope was developed at MPI für Mikrostrukturphysik in Halle that brings outstanding energy and $k_{\parallel}$ resolution [92]. A schematic view and electron trajectories are shown in Fig. 3.11. Energy filtering is performed also with the help of two hemispherical analysers of 150 mm in radius. The total image magnification of a system can be written as product of the magnifications of the objective lens, the first and the second retarding stages in Fig. 3.11(b). A single lens action is calculated in the following way (according to Liouville's theorem, from [92]):

$$M = \frac{\boldsymbol{k}_{\parallel}^{max}}{\sin(\alpha_A)\beta\sqrt{E_{Pass}}}, \tag{3.14}$$

where M is the magnification, $\beta = \sqrt{2m_e/\hbar^2}$, $E_{Pass}$ is the pass energy of the hemispherical analyser, $\alpha_A$ is the angular acceptance interval of the analyser, $\boldsymbol{k}_{\parallel}^{max}$ is the maximum parallel momentum that is transmitted at a given kinetic energy. The most important part that influences the resolution of the system is the objective cathode lens. It is schematically presented in Fig. 3.12 including the electron trajectories exiting at 5 different $\Delta\boldsymbol{k}_{\parallel}$ alues (within the range of ± 2Å$^{-1}$) and from three different positions on the sample with 50 $\mu m$ spacing [92]. Each electron enters the objective lens at an angle $\alpha'$, so that:

$$\sin(\alpha') = \frac{\boldsymbol{k}_{\parallel}}{\beta\cdot\sqrt{eU_A+E_0}}, \tag{3.15}$$

where $U_A$ is the accelerating anode voltage, $E_0$ is the electron start energy. From this equation it is obvious, that for large accelerating fields when $eU_A \gg E_0$, the magnification of the first momentum image in the backfocal plane of the objective lens proportionally depends solely on the initial parallel momentum.

It was estimated that the most crucial influence on the resolution makes the spherical aberration, which is mainly proportional to the third order of $\alpha'$. In Fig. 3.12(b) solid symbol lines illustrate the aberrations (electron displacement) of the objective lens $\Delta r = C_s M_0 \alpha'^3$. Higher order terms of aberration are also considered in [92]. Aberrations tend to diminish with smaller $k_{\parallel}$ (smaller $\alpha'$) and higher $U_A$ (which also leads to decrease of $\alpha'$). The fifth-order term becomes important for large $k_{\parallel}$ and requires higher acceleration voltage for

imaging. The dashed lines in Fig. 3.12(b) show the projected slit width thus illustrating the influence of the analyzed area on spherical aberrations.

The energy resolution of the device is defined by the same equation and as follows from equation (3.8) $\Delta E$ depends on the pass energy. For this instrument both hemispheres add up in dispersion, i.e. R in (3.8) is the sum of both radii.

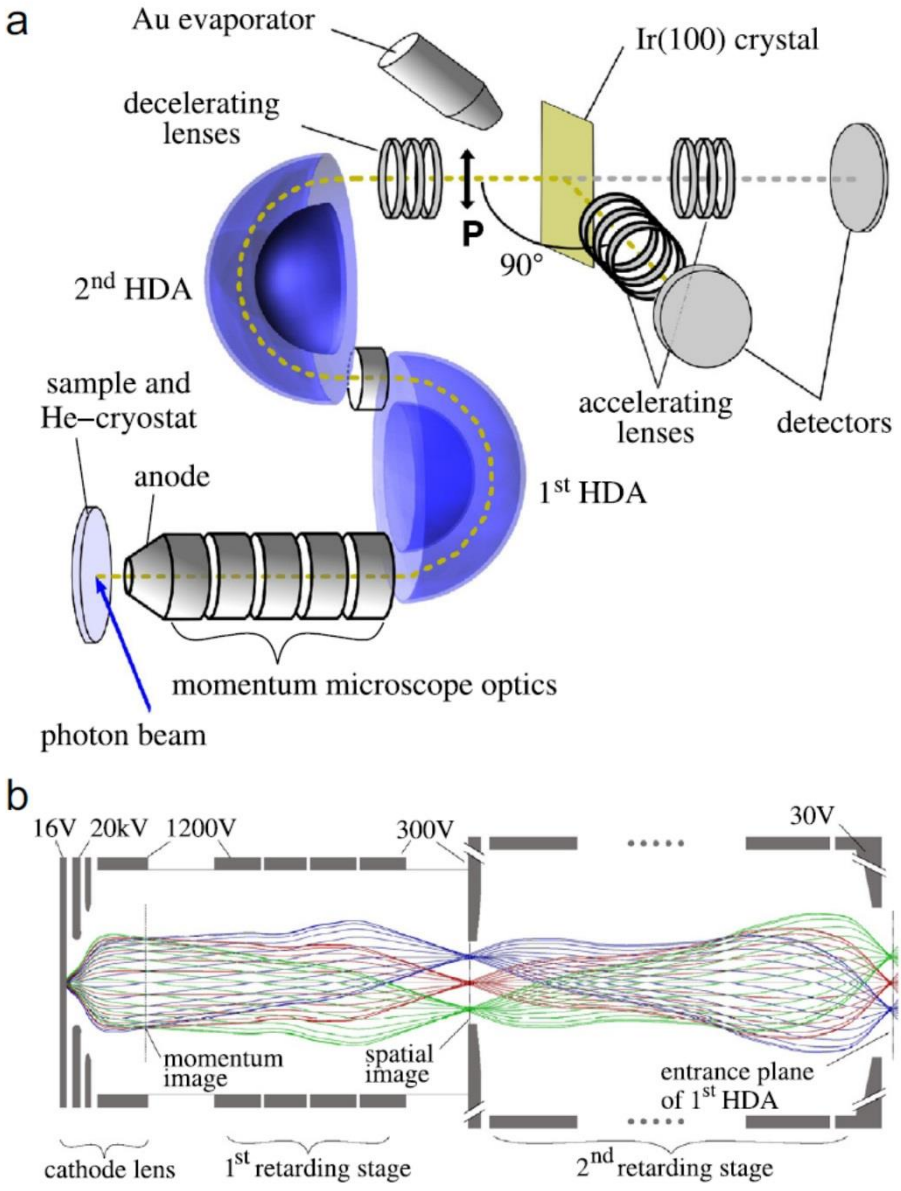


**Fig. 3.11.** Schematic view of a new generation of momentum microscope with imaging spin filter as developed at the Max Planck Institute in Halle (a). Schematic overall lens system and electron trajectories (b). (From [92])

Momentum resolution was determined on a Au(111) sample at a temperature of 18 K. Au (111) was chosen as an appropriate system for momentum calibration and tests of energy

resolution. It exhibits a paraboloid-shaped Shockley surface state with non-uniform spin structure. The state shows Rashba-type spin splitting into an inner and outer branch due to spin-orbit interaction[96,97].

The energy resolution was defined experimentally by measuring the intensity in the $\bar{\Gamma}$ point for different binding energies (along the dashed line in Fig. 3.13(b)). Interestingly, the real measurements of $\Delta E$ at pass energies of 50 to 100 eV appeared smaller than calculated from formula (3.8), i.e. for an ideal hemispherical spectrometer. At 15 eV pass energy, the measured energy resolution is 12 meV, as follows from the linescan (panel (d)) across the dashed line in Fig. 3.13(b). The geometrically calculated broadening is 10 meV and additional experimental broadening is attributed to unstable electrode voltages.

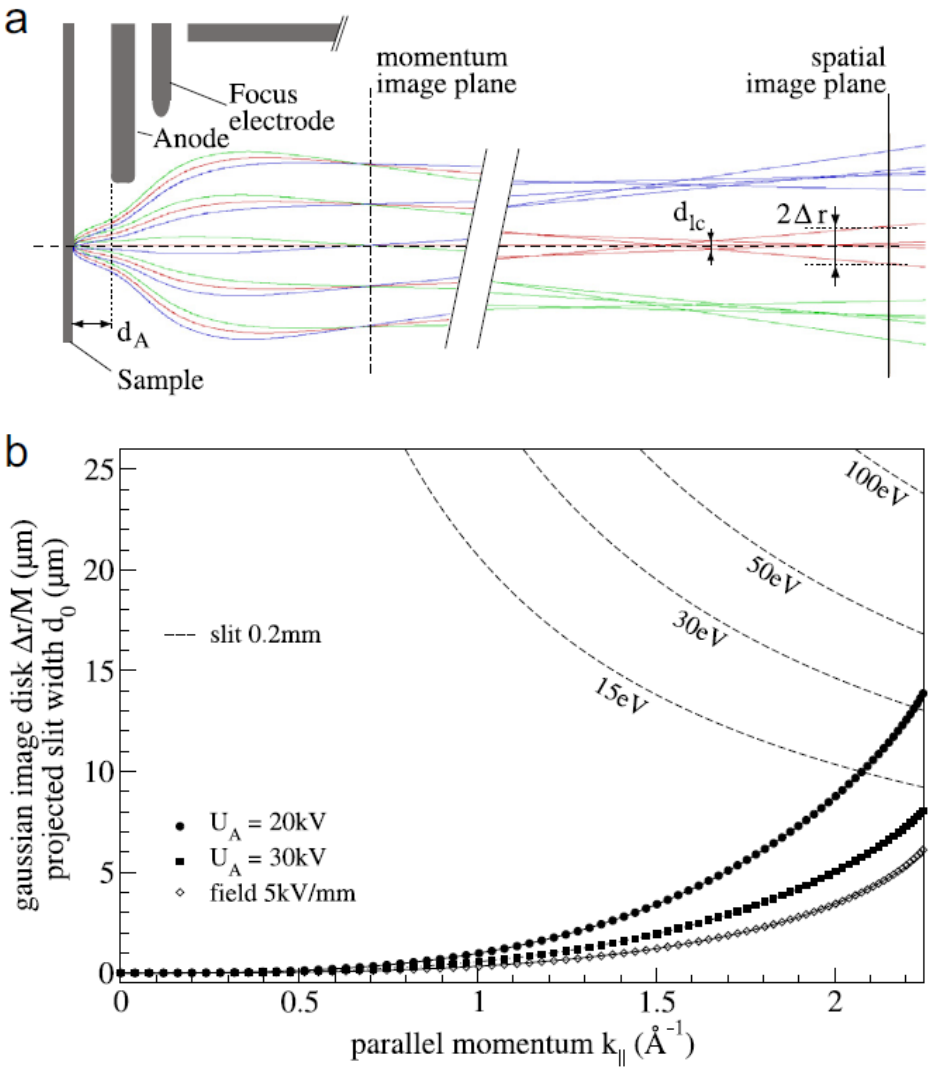


**Fig. 3.12.** Schematic view of the momentum microscope objective lens including the sample, anode and two focusing electrodes; electron trajectories are shown (a). Transverse displacement of electrons (solid symbols) and projected width of the analyser slit in the first Gaussian image plane. Other explanations are given in the text. (From [92])

The $\boldsymbol{k}_{\parallel}$ resolution was measured at 30 eV pass energy. The Shockley state exhibits a shape of two concentric circular bands. They are separated by $\Delta\boldsymbol{k}_{\parallel}$=0.025 Å$^{-1}$[96,97]and the inner and outer circles have radii of 0.165 and 0.190 Å$^{-1}$, respectively. These states appear clearly separated in Fig. 3.13(a),(b). A line scan along the dashed line in panel (a) is presented in panel (c). It reveals a $\boldsymbol{k}_{\parallel}$ resolution of the instrument of 0.0049 Å$^{-1}$ [92].

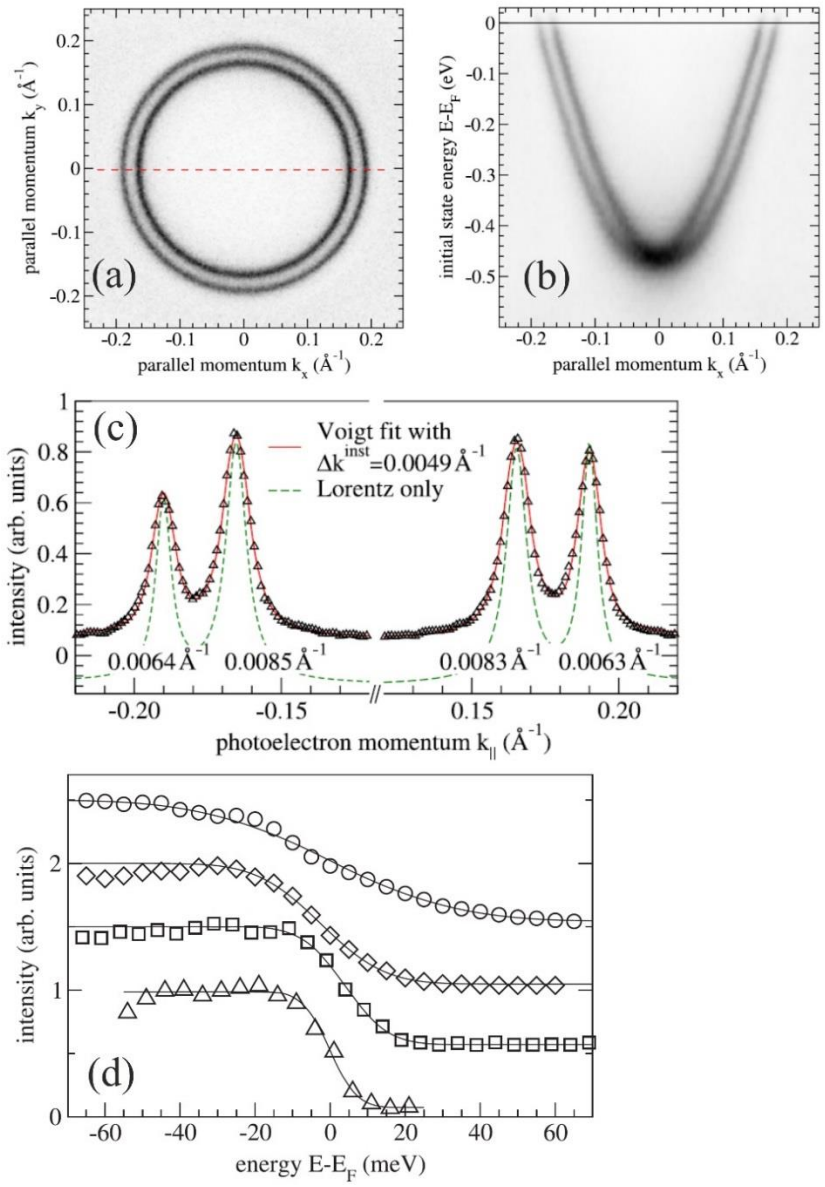


**Fig. 3.13.** Momentum image of the Shockley state on the Au(111) surface at the Fermi energy (a). Cut at $k_{\mathrm{y}} = 0$ through a series of momentum images taken at different energies (b). Intensity profile for $k_y = 0$, along the dashed line in panel (a), measured at the Fermi level (c). Intensities measured in the center of the Brillouin zone of the Au(111) sample cooled to 18 K (b), as a function of binding energies for pass energies E=100, 50, 30 and 15 eV, starting from the top curve (d). (From [92])

# 4. Experimental details

## 4.1. Sample preparation and characterization

A (110) surface of a molybdenum single crystal was studied. We concentrated on the investigation of surface electronic states and surface resonances, thus an atomically clean sample surface was a necessary precondition. Sample cleaning was performed in a standard procedure [32] of oxidation cycles accompanied by high-temperature flashes. Oxidation was performed in 5 $\times 10^{-7}$ mbar oxygen atmosphere at a temperature of 1600 K with a subsequent flash at 2100 K to remove the oxide. Newly produced single-crystal metal samples often contain many impurities (in particular, carbon and sulfur). Upon heating, these atoms segregate from the bulk to the surface. Thus, after several flashes even in UHV the sample surface is rapidly contaminated. Therefore at the initial stage every sample requires long term cycle cleaning to purify the bulk in the surface vicinity. Such initial cleaning was performed in front of a LEED unit for fast surface geometry checks.

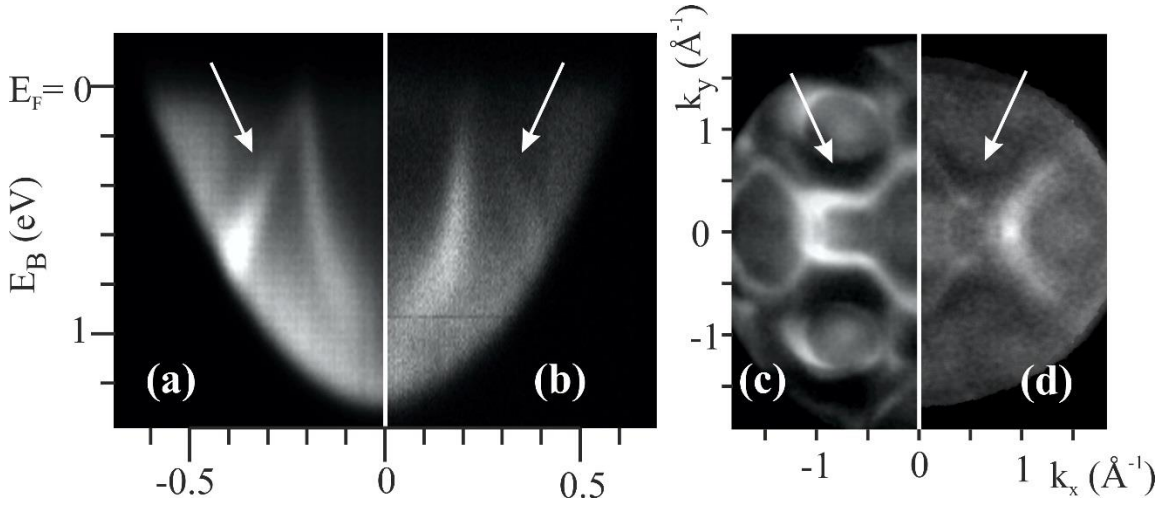


**Fig. 4.1.** $\bar{\Gamma} - \bar{\mathrm{N}}$ section of the clean Mo(110) band structure taken with Ti-sapphire laser excitation (2 PPE at $2h\upsilon$ = 6.2 eV) (a). The same but 1 hour after cleaning under UHV conditions, shows a disappearing band due to a small amount of adsorbates (b). Constant energy section close to the Fermi level obtained with synchrotron excitation ($h\upsilon = 35\ eV$) shows a partial band gap (c). The same, but taken for an earlier cleaning stage (not clean surface) shows less black-and-white contrast and no band gap.

The experimental chamber had no LEED system attached. After the sample was transferred into the system via atmosphere, cleaning was performed based on momentum

images (Fig. 4.1). In the laboratory experiments, we observed a quite sensitive electronic state, denoted by an arrow in Fig. 4.1(a). This is the surface state similar to the one labeled B in Fig. 2.1 and it corresponds to surface dangling bonds, as discussed in literature [16,23,98]. This state survives on a clean Mo(110) surface only for about 0.5-1 hour in UHV conditions at 1-2×$10^{-10}$ mbar pressure and then smears out accompanied with an overall increase of background intensity and a decrease of contrast, Fig. 4.1(b). In the synchrotron experiments the excitation energy was substantially different and due to selection rules and matrix element effects the state differs in intensity. In this way we referred the general contrast and low background intensity in partial band gap regions (Fig. 4.1 (c),(d)) to the surface cleanness.

Oxygen-covered surfaces with different coverage were obtained in two different ways. In laboratory experiments – short term exposure to oxygen at a pressure of 2×$10^{-8}$ mbar at room temperature. At the synchrotron the sample was heated to 1100 K in ~5×$10^{-8}$ mbar oxygen atmosphere for 15 minutes and then annealed at 1200 K for a few seconds in UHV.

## 4.2. Time-of-flight momentum microscopy

Time-of-Flight (ToF) momentum microscopy is a novel approach to investigate the electronic bandstructure. It aims at even more parallelization than momentum microscopy with a dispersive energy analyser. To achieve this, ToF momentum microscopy implements simultaneous detection of photoelectrons in a whole range of kinetic energies. The method combines the *k*-imaging properties of a cathode-lens microscope, which is optimized for best resolution of the reciprocal image [92], with the superior resolution and parallel acquisition capability of imaging ToF electron microscopy [99]. In the present setup, time (energy) resolved electron imaging is realised by ToF electron dispersion in combination with a space and time-resolving (3D) imaging device, capable of measuring the exact time and spatial coordinates of every electron hit, such as a delay-line detector (DLD).

The basic idea of momentum microscopy makes use of the fact that in each imaging optical system the reciprocal image represents the distribution of the transversal momentum components. In mathematical language it is defined as the Fourier image, providing the distribution of "spatial frequencies" (being nothing else than the transversal momentum pattern). Owing to $\boldsymbol{k}_{\parallel}$-conservation in the photoemission process, the reciprocal image formed by the objective lens of a photoemission microscope directly yields the surface-projected band structure inside the crystal. This image occurs in the back focal plane of the cathode lens. In momentum microscopy this Fourier pattern is imaged with ultimate k-resolution [92]. The intriguing advantage is that high accelerating voltage of the cathode lens

gives access to the $\boldsymbol{k}_{\parallel}$–distribution of the full half-space above the solid at kinetic energies of 100 eV and more. For sufficiently high photon energy, the angular range of outgoing electrons corresponds to a large parallel momentum range in the solid, exceeding the first Brillouin zone. Principally, the technique is applicable in a wide energy range up to hard x-ray excitation in the several keV regime.

Generally, band mapping using the momentum microscopy approach sets to resolve three electron coordinates, i.e. two lateral coordinates being characteristic for $\boldsymbol{k}_{\parallel}$ and the kinetic energy "coordinate" determined by the binding energy $E_B$ according to equation (3.2). Taking into account that most electron detectors are zero- or two-dimensional (channeltron, MCP-screen), conventional band mapping requires scanning of one of the coordinates to get a set of two-dimensional spatial distributions of electron intensity. The common approach is to scan the energy coordinate. This was previously realized using energy filtering with an imaging dispersive energy analyser [88].

Unlike other techniques, where one measures slices at various energies sequentially, a ToF momentum microscope instantly measures a 3D distribution in coordinates (x,y,t) representing the electronic surface-projected band structure of a sample in ($k_{\mathrm{x}}$, $k_{\mathrm{y}}$, $t$). Fig. 4.2 shows a 3D plot of a constant intensity surface (in reciprocal coordinates $k_{\mathrm{x}}$, $k_{\mathrm{y}}$, $t$), representing a measurement of an oxygen-covered Mo(110) surface. The excitation of two-photon photoemission was performed with a frequency-doubled Ti:Sapphire laser ($2h\nu$ = 6.2 eV). With the help of special software these 3D data can be further cut into sections, viewed at all possible angles, etc. for better presentation of the features.

The principal scheme of a ToF microscope with electron trajectory lines is presented in Fig. 4.3. The ToF energy filtering approach facilitates parallel acquisition of an energy range of photoemitted electrons of the order of 1.5-3 eV width limited by the chromatic aberration of the microscope. Thus it greatly reduces measurement time. In this respect the approach has the minimum possible ratio between the excitation dose and collected signal. This characteristic is very important for the investigation of samples sensitive to radiation damage such as DOEO, Fabre salts, etc. [100,101] with hard X-Ray photoelectron spectroscopy, when the photoemission cross section is very small and radiation damage is a time-limiting factor. Another field of application would be spin-resolved band mapping, when the signal intensity is tremendously lowered by a spin-filter. ToF momentum microscopy allows the implementation of a modern spin detection method with an imaging spin-filtering crystal [102, 103].

One constraint of this approach is that it requires a pulsed photon source like a synchrotron, a free-electron laser, a pulsed laser or a high-harmonic source. A table-top experiment can be

performed with a laser source at the expense of the smaller accessible range of momenta and binding energies.

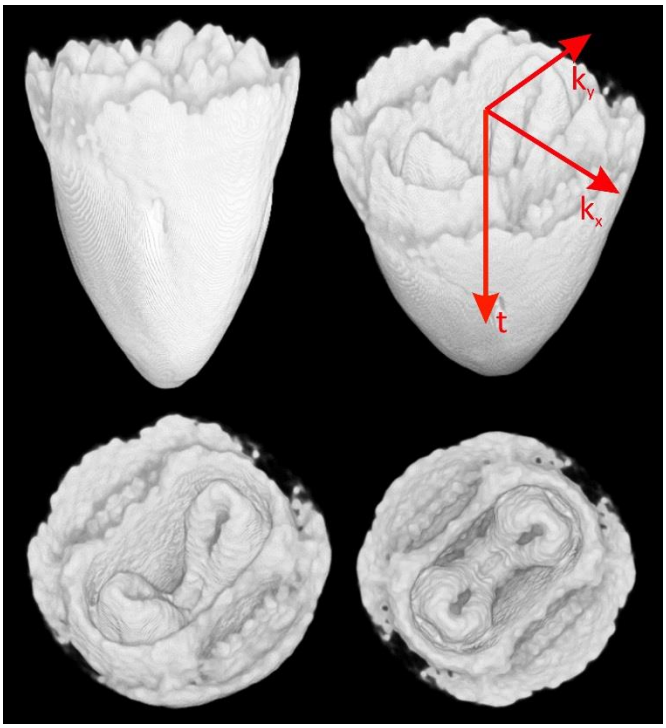


**Fig. 4.2.** 3D representation of the distribution of photoemission intensity from O/Mo(110) in coordinates ($k_x$, $k_y$, $t$). The figure shows raw data, as accumulated in the ToF k-microscope. Just the contrast is set in the viewing software.

The DLD is a key component of the microscope. This imaging unit consists of a multichannel plate (MCP) detector with flat crossed wireframe anodes (Fig. 4.4) behind it. It is capable of counting incident particles subsequently by means of a time-to-space conversion for the lateral coordinates. The MCP is used as a position-sensitive electron multiplier that amplifies single incoming electrons by a factor of at least $10^7$ [104, 105]. Its basic working principle is shown in Fig. 4.4. On each end of two wire meanders a synchronized time to digital converter (TDC) is situated. When an electron hits the MCP it causes a burst of secondary electrons exiting the micro channels at the opposite side of the plate. These electrons induce an electromagnetic pulse in the meanders which runs and disperses to both ends, reaching different TDCs at different times, depending on the position of the electron hit. Each of four TDCs measures the time of the arriving electronic pulse. The exact time of an event can be extracted from the mean value of all four measured time values. The two lateral coordinates are calculated by the difference of pulse propagation times to both ends of each meander.

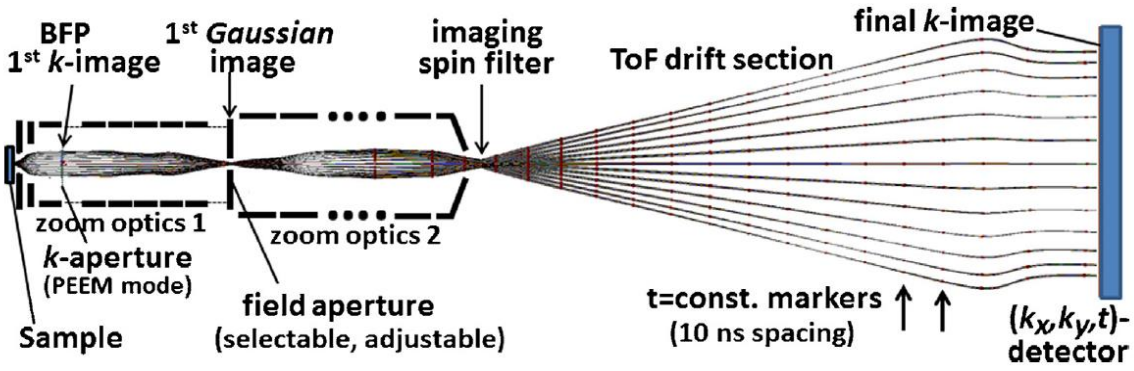


**Fig. 4.3.** Schematic cross section of the ToF k-microscope. Trajectories for 100 eV start energy on the sample and drift energy 30 eV are shown. An imaging spin filter can be inserted as indicated. Isochronous contours in the ToF section, marked by dots on the trajectories, show high planarity. Trajectories exhibit small divergence, the radial coordinate is stretched by a factor of 10. (from [106])

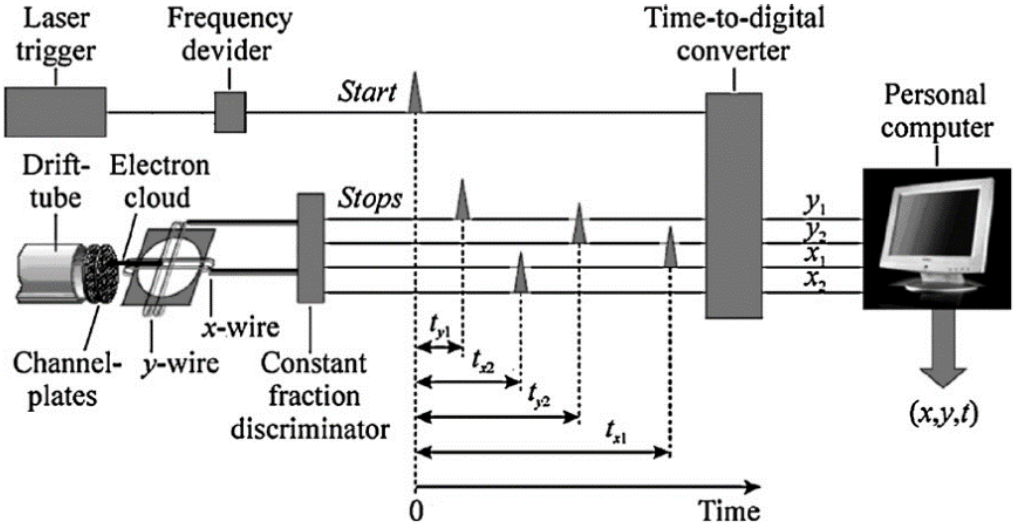


**Fig. 4.4.** Principal scheme of time- and lateral-resolved electron detection with a delay line detector (DLD). Two wire meanders oriented orthogonally are responsible for determination of x and y spatial coordinates as well as for the time of an electron hit. The four meander outputs of the delay line anode are measured with respect to any periodic start signal by means of a fast pulse processing unit. The position of an event on the detector is defined from differences of the corresponding time results (from [105]).

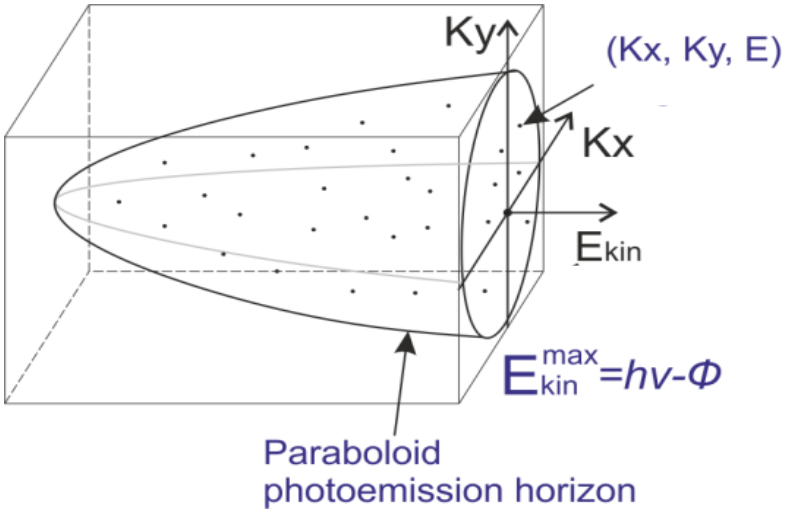


**Fig. 4.5.** The 3D data matrix and electron coordinates are confined by the paraboloid-shaped photoemission horizon and the cut through the Fermi energy, visible as $E_{kin}^{max}$.

Fig. 4.5 illustrates the basic principle of ToF momentum microscopy: All counting events in the $E - \boldsymbol{k}_{\parallel}$ paraboloid confined by the Fermi-energy cut and the photoemission horizon (condition $\boldsymbol{k}_{\perp}$=0) are detected at a fixed setting of the k-microscope. The binding energy (with respect to $E_F$) is determined as in a conventional photoemission experiment $E_B = h\nu - \Phi - E_{bias} - E_{kin}$, where $h\nu$ is the photon energy, Φ is the work function, $E_{bias}$ is the sample potential with respect to the drift space potential, and $E_{kin}$ is the electron energy in the drift space. Utilizing the relation between $E_{\mathrm{kin}}$ and time-of-flight one can determine the binding energy from the electron flight time. The 3D image detector (delay-line type) [105,107] accumulates the counting events in the $(E_{\mathrm{B}}, k_{\mathrm{x}}, k_y)$-voxels of the data matrix. For visualization, sections can be made in any plane of the $I(E_{\mathrm{B}}, k_{\mathrm{x}}, k_y)$ matrix (or 3D tomograms).

Obviously, the time resolution of a DLD is a limiting factor for the energy resolution of the momentum microscope. For a given time resolution, the energy resolution can be increased by extending the length of the ToF space or decreasing the kinetic energy of the electrons in the ToF space. The resolution of the instrument depending on the length of the drift space can be easily calculated from a simple nonrelativistic kinetic energy formula[105,107].

$$\tau = L(m_e/2E_{kin})^{1/2}, \tag{4.1}$$

$$dE/_{d\tau} = -2(2E_{kin}^3/m_e)^{1/2}/_L, \tag{4.2}$$

where L is the length of a drift space, $E_{kin}$ is the electron energy in the drift space and $m_e$ is the electron mass. In the ToF drift section, the electron energy is calculated as $E_{kin} = h\nu - \Phi - E_B - E_{bias}$. Here we suppose that the electron propagation time inside the microscope is negligible, except the ToF section. This assumption is rational as soon as the electron optics is run under much higher voltages than the drift section electrode. In the other case in order to determine $\tau$ and $dE/d\tau$ a full simulation of the electron propagation in the microscope column has to be performed by means of a special software like SIMION.

The time resolution of the present DLD generation is about 180 ps. For the given length of the drift section (900 mm) drift energies between $E_d$ = 40 eV and 4 eV yield theoretical energy resolution $\Delta E$ = 50 meV down to 2 meV, respectively (Fig. 4.6). Although it is possible to decelerate electrons almost to zero kinetic energy to gain energy resolution, this is difficult due to the increasing effect of external magnetic fields (in case of insufficient magnetic shielding) and leads to image distortions and loss of k-resolution.

A size-selectable and adjustable field aperture located in the first Gaussian image plane (Fig. 4.3) defines the source spot on the sample surface for the present instrument in a range of 25 to 150 μm. This allows an increase of momentum resolution by restriction of the source spot size, independent of the focusing quality of the photon source. In a momentum microscope the reciprocal image is magnified onto the image detector. In this case, the selected field of view acts in the same way as a usual contrast aperture (placed in a reciprocal image plane) of a conventional real-space photoelectron microscope (PEEM). For sufficiently high photon flux density on the sample, a field of view down to <1 μm can be selected in the Gaussian plane, at the expense of a smaller accessible momentum disc. The zoom optics can also be used to focus a Gaussian image onto the DLD for spectroscopic ToF-PEEM imaging. In this mode a k-aperture can be moved into the backfocal plane (BFP), acting as a normal contrast aperture for resolution optimization. Both apertures are driven by piezomotors with absolute position readout.

A zoom lens transforms the electron beam to the desired drift energy in the imaging time-of-flight spectrometer. Photoelectron momentum maps and spectra are taken simultaneously in an energy interval of typically 1.5-3 eV width, limited by the chromatic aberration of the objective lens. Constant time markers and corresponding dots on electron trajectories in Fig. 4.3 show isochronous surfaces in the ToF section with 10 ns spacing. Good flatness of these planes evidences a highly uniform energy scale for the instrument across the whole detector surface and an absence of transversal momentum influence on the time of flight. In other words, there is essentially no correlation between the transversal

momentum and the kinetic energy. This is an outstanding feature of the present instrument, in comparison to other spectroscopic ToF devices. There are two reasons for this: (I) the cathode lens is a strong immersion lens causing a virtual image of the source at twice the distance from the extractor electrode with an apparently much higher starting energy of ~20 keV (depending on the extractor potential) and a much smaller cone of effective emission angles; (II) in the subsequent electron-microscope column there is no significant beam deterioration (small filling factors of lenses, low aberrations). The radial coordinate in Fig. 4.3 is 10x stretched, i.e. in an isogonic plot all rays would run very close to the axis except for the linearly-diverging beam in the drift section.

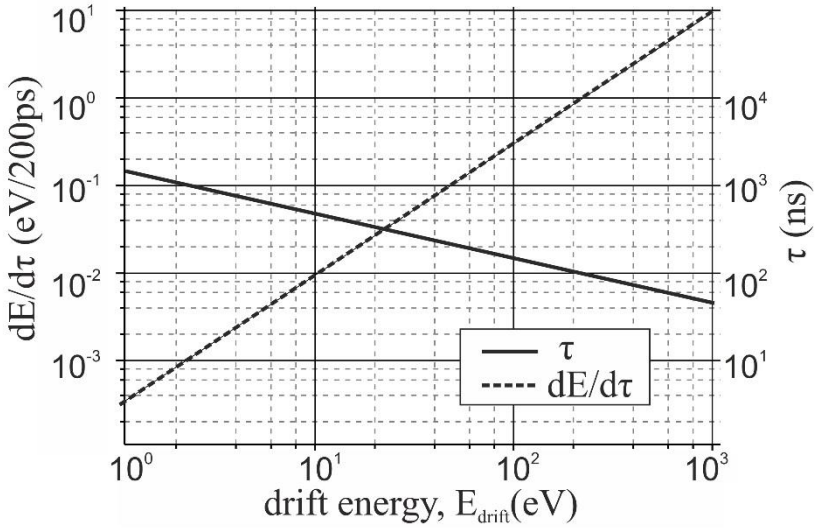


**Fig. 4.6.** Calculation of time-of-flight and dispersion dE/dt versus drift energy $E_d$ for a drift tube of 900 mm length and an assumed time resolution of 200 ps.

The described device allows implementation of a spin-filter [108, 92]. It is supposed that the imaging spin filter crystal is situated in the place, designated in Fig. 4.3 at 45º to the microscope axis. Electrons are reflected specularly and a spin-filtered beam travels a second ToF section to the DLD. Spin filtering is due to high spin-orbit interaction for electrons in a high-Z target. This approach to spin filtering benefits from large efficiency, providing a multichannel approach with up to $10^4$ independent data points simultaneously [109]. In our case this means simultaneous acquisition of a large part of the electron signal, and not a point-by-point spin probing, as in the case of a Mott or classical SPLEED detector. Still this approach is demanding, as the reflectivity and spin-selectivity (asymmetry) depends on polar and azimuthal angles of the detector and also on the energy of the incident electrons. For

effective filtering one needs a working point with high and uniform reflectivity and asymmetry over some energy and angular interval. In our experiment, the energy width of the working point is especially important, as we aim at simultaneous collection of electrons spread in energy by several eV.

## 4.3 Energy- and *k*-calibration and resolution

The kinetic energy of the electron in the drift section is $E_d = h\nu - \Phi - E_B - E_{bias} + E_{drift}$, where $E_{bias}$ and $E_{drift}$ are the sample and drift space potentials multiplied by the electron charge, respectively.

In the drift section the electron time of flight is expressed by the formula:

$$\tau = \frac{C}{\sqrt{h\nu - \Phi - E_B - eU_{bias} + eU_{drift}}} + \tau_0, \quad (4.3)$$

where $\tau_0$ is the delay between the laser pulse and DLD trigger pulse, $C$ is a constant representing mainly the electron path geometry. It is obvious that the function $E_B(t)$ needs an energy calibration from the experiment and, in addition, this relation is non-linear.

Energy calibration for the experiments was performed by measuring the same spectrum at different sample bias voltages in the following way. First we measure ToF spectra at different bias voltages, for instance $eU_{bias}$= 9, 10, 11 and 12 V (Fig. 4.7). Then we define the positions of marked features in the ToF spectra (table 1).

As known, the work function of Mo ranges from 4.3 to 4.95 eV [110]. The (110) face is the most closely packed and has the highest work function of Φ =4.95 eV. The photon energy was $h\nu$ =35 eV. The drift space was at ground potential, $U_{drift}$=0.

It needs several steps to precisely define the binding energy of a spectral feature with respect to the Fermi edge. In the first step we fit the data in table 1 with the formula (4.3) (Fig. 4.8), using a least squares fit. This gives us the unknown values $t_0$ and $C$ to find the transfer function of the microscope. In our case the values obtained for the parameters were C= $(313.99 \pm 3.23)$ $[ns\sqrt{eV}]$, and $\tau_0$=$(38.516 \pm 0.744)$ [ns]. With these, the energy position of a given peak can be determined. For this purpose we use only use time measured at $E_F$ because the binding energies E(A) and E(B) are not known precisely.

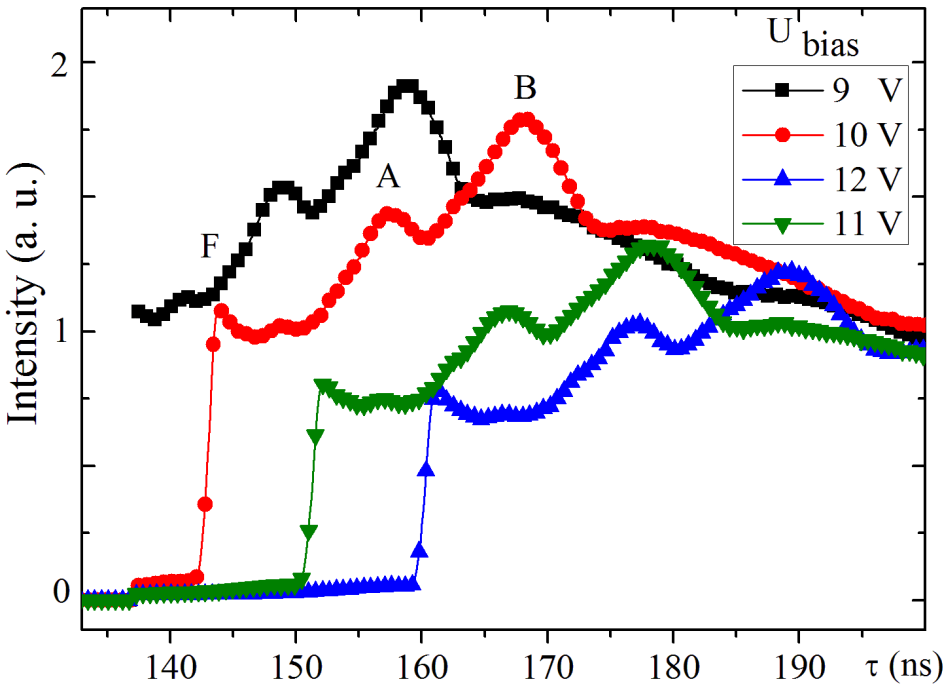


**Fig.4.7.** Time-of-flight photoelectron spectra from Mo(110) taken at $U_{bias}$= 9, 10, 11 and 12 V. The black curve is truncated at the lower end of the timewindow.

**Table 1.** Position of characteristic features F, A and B in Fig. 4.7

| $U_{bias}$ | $\tau\ at\ E_F, ns$ | $\tau\ at\ E(A), ns$ | $\tau\ at\ E(B), ns$ |
|---|---|---|---|
| 9 | Out of range | 149 | 159 |
| 10 | 144 | 157 | 168 |
| 11 | 152 | 167 | 178 |
| 12 | 161 | 177 | 189 |

For the studied case of Mo(110) and zero drift space potential ($U_{drift}$=0) we get:

$$\tau = \frac{C}{\sqrt{h\nu - \Phi - E_B - eU_{bias}}} + \tau_0, \tag{4.4}$$

$$Ekin = \frac{C^2}{(\tau - \tau_0)^2}, \tag{4.5}$$

$$E_B = h\nu - \Phi - eU_{bias} - \frac{C^2}{(\tau - \tau_0)^2}. \tag{4.6}$$

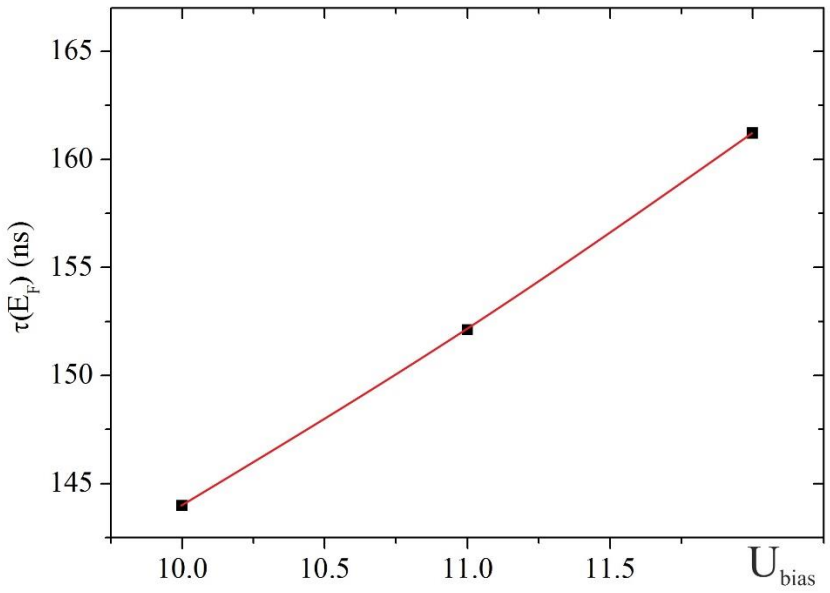


**Fig. 4.8.** Least squares fit for the data (Fermi cut-off) in table 1 by the formula (4.3).

The $\boldsymbol{k}_{\parallel}$-scale, in the case of the synchrotron experiment, can be calibrated by measuring the size of the first Brillouin zone. When the excitation energy is high enough, a part of the Fermi surface larger than the first Brillouin zone can be observed on the screen. It is necessary to define the boundaries of the Brillouin zone in the pattern on the screen as a primitive cell in reciprocal space. Its size is defined by the real size of the primitive cell in real space. The latter, in turn, can be calculated from the real crystal lattice constant, which is known or can be measured by other methods (LEED, RHEED, HRTEM, diffraction in TEM, STM, etc). Thus, in our experiments we usually used one to one scaling of the theoretically calculated and experimentally observed constant energy photoemission patterns to determine the absolute scale for our measurements.

In the case, when the accessible area in reciprocal space is smaller than the first Brillouin zone, it is not possible to define the field of view from the point of the translation symmetry of the pattern on the screen. Then one can determine the field of view radius (the maximum accessible $k_{\parallel}$ ) by theoretical means. For a free electron we have:

$$E_{kin} = \frac{p^2}{2m} = \frac{\hbar^2 k^2}{2m} = \frac{\hbar^2}{2m}\left(k_x^2 + k_y^2 + k_z^2\right) \qquad (4.7)$$

On the other hand the kinetic energy of an electron in the photoemission process:

$$E_{kin} = h\nu - \Phi - E_B \qquad (4.8)$$

In an ARPES experiment electrons at the edge of the field of view (the so-called photoemission horizon, see also Fig. 4.5) at the Fermi energy have maximum possible kinetic energy and zero $k_\perp$, so the maximal $k_\parallel$ is given by:

$$k_{\parallel max} = \frac{1}{\hbar}\sqrt{2m_e E_{kin}} \tag{4.9}$$

After this, having a reference size of the field of view, one has a k-scale for the observed patterns. An example was shown in Fig. 4.1.

The energy resolution obtained during the synchrotron experiment was evaluated at the Fermi edge. The sample temperature was about 150 K, so thermal broadening of electrons at the Fermi edge makes about $4kT$ = 52 meV. During the synchrotron experiment on Mo(110) the measured Fermi edge width (rise of intensity from 20% to 80% of the maximum) was 96 meV (Fig. 4.9(a,b)). A higher energy resolution was obtained during a 1PPE laboratory experiment with laser excitation on a caesiated Au(111) sample cooled down to 150K. A resolution of 28 meV was measured at the bottom of parabolic photoemission horizon shown in Fig. 4.9(c,d).

As a consequence of rather low pulse frequency of BESSY II in single-bunch mode of 1 MHz and high photoelectron intensity the space charge effect was observed to distort the momentum image and lower the resolution. The Fermi surface in this case appear curved with maximum distortion at the $\bar{\Gamma}$-point (Fig. 4.10). Decreasing the intensity by 80% one reduces the space-charge influence, as can be seen by the smaller Fermi edge curvature and better resolved features in the area marked with a dashed circle. Thus, the space charge effect may be one additional limiting factor for the signal intensity as discussed in [111].

During the synchrotron experiment a great amount of secondary electrons is produced, so the intensity of non-scattered electrons is rather low in comparison to the total photoemission intensity. The secondary electrons were cut off with the help of a grid in front of the electron detector, driven at negative (retarding) voltage. At the same time, the use of a grid in the electron path disturbed the image at the screen, decreasing the $\boldsymbol{k}_\parallel$-resolution. During the Mo(110) experiment a resolution of 0.05 $Å^{-1}$ was measured at the edge of the feature S4 (see also Chapter 5.2), presented in Fig. 4.9(e,f)). With laser excitation under laboratory conditions the amount of secondary electrons is much smaller, so there is no need to use a retarding grid. Fig. 4.9(g,h) shows a surface state on Au(111) close to the Fermi level. As known, it shows a Rashba-splitting of 0.025 $Å^{-1}$[42,112], which was barely resolved in an experiment with our set-up (Fig. 4.(g)). The estimated resolution measured at the edge of the photoemission horizon for this measurement was about 0.01 to 0.02 $Å^{-1}$(Fig. 4.9(g,h)). Further measurements on energy and momentum resolution at lower temperature are under way.

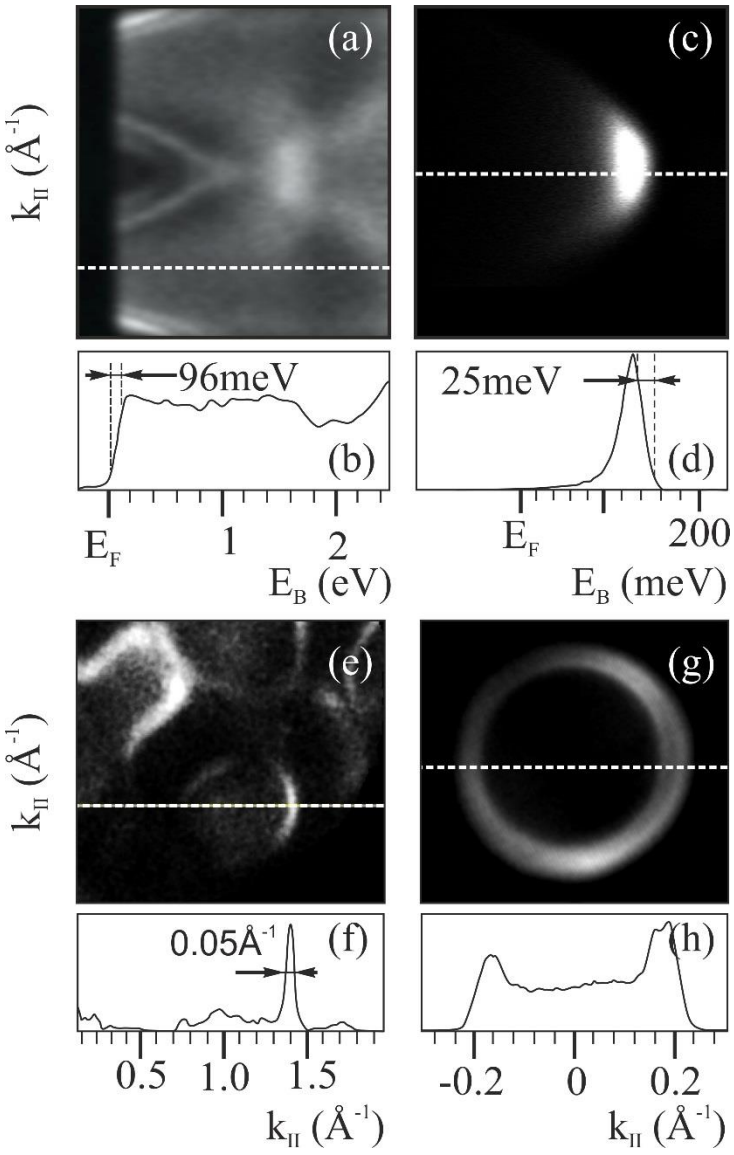


**Fig. 4.9.** E-vs-$k$ section across the 3D bandstructure of Mo(110) parallel to $\bar{\Gamma} - \bar{\mathrm{N}}$ in the vicinity of the $\bar{\mathrm{S}}$-points for the synchrotron experiment (a,b); the same for 1PPE laser excitation on a caesiated Au(111) cooled to 150 K (c,d); $k_x - k_y$ section from synchrotron experiment for Mo(110) (e,f); the same for the 1PPE experiment with laser excitation on a caesiated Au(111) sample cooled to 150 K showing spin-orbit splitting of the surface state (g,h). The lower panels show linescans across the white dashed lines.

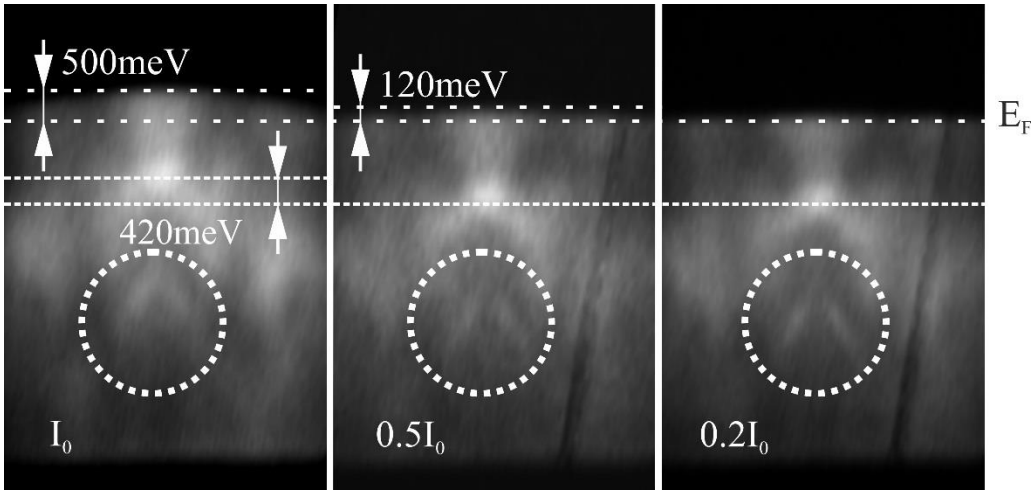


**Fig. 4.10.** $\bar{\Gamma} - \bar{\mathrm{H}}$ section of the band structure of an unprepared Mo(110) surface at different photon intensity of the synchrotron beam. The Fermi level appears bent in the left and center panels due to the space charge effect.

## 4.4 Ti:sapphire laser and Synchrotron beamline U125-SGM at BESSY II

Measurements were performed with two different excitation sources. In the lab – with a Spectra-Physics Mai Tai® Ti:sapphire laser oscillator. It offers a tunable range of wavelengths from 750 to 850 nm, which corresponds to a photon energy range from 1.66 down to 1.46 eV. We used linearly and circularly polarized light. Photoemission experiments were performed in two-photon photoemission mode (2PPE) with frequency-doubled laser light, thus the excitation energy was $2h\upsilon =$ 5.84 to 6.64 eV. The pulse frequency was 80 MHz and the pulse width was 100 fs, according to specifications of the laser. Such a short pulse leads to a relatively large bandwidth broadening due to Heisenberg's uncertainty principle: $\Delta t \times \Delta E \geq \hbar/2$. For Δt=100 fs, $\Delta E \geq \frac{\hbar}{2\Delta T}$ =3.3 meV. The laboratory experiments were done at room temperature, causing an energy broadening of about $4kT \approx$ 100 meV at the Fermi edge.

The work function of clean Mo(110) is 4.95 eV [110,113], giving an accessible binding energy range up to 1.69 eV. Therefore at the Fermi surface the accessible momentum area has a radius of $\boldsymbol{k}_{\parallel max} = \frac{1}{\hbar}\sqrt{2m_e E_{kin}} = 0.66$ Å$^{-1}$.

The measurements with Synchrotron radiation were taken at beamline U125-2 SGM [114] at BESSY in July 2014 during a single-bunch beamtime (pulse period 800 ns). It is equipped with a *spherical grating monochromator* with a 500 l/mm grating providing

photons in the energy range from 29 to 138 eV. The energy resolution of $E/\Delta E$ = 16000 gives a bandwidth of about 2 meV at 35 eV photon energy. Given the work function of Mo(110) this results in a kinetic energy range of 30 eV with the lowest 10 eV being cut off by retarding electron lenses or by the retarding grid in the front of the electron detector. Typical photon flux at 35 eV is about $10^{12}$ photons per second for an electron current of 280 mA, translating into $4x10^{10}$ photons per second for the single-bunch conditions of about 10 mA. The focused spot was 120 by 60 μm in size, the actual source size being selected electron optically. During experiment the sample was cooled to 140K.

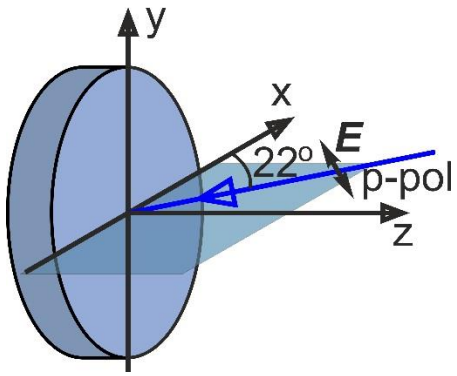


**Fig. 4.11.** Geometry of the experiment. The photon beam is p-polarized with the electric vector **E** lying in the xz-plane. Linear dichroism asymmetries are discussed in the coordinate system shown, with either the $\bar{\Gamma} - \bar{H}$ or $\bar{\Gamma} - \bar{N}$ azimuth parallel to the x-axis.

Fig. 4.11 shows the experimental geometry and defines the coordinate system. The photon beam was linearly polarized in horizontal direction, which means p-polarization for our geometry. The impact direction was 22° from the x-axis, see Fig. 4.11. The azimuth of photon impact could be varied via sample rotation.

In addition to 3D intensity maps $I(k_x, k_y, E_B)$, maps of linear dichroism in the angular distribution (LDAD) are are determined from the intensity patterns of the x>0 and x<0 half planes. This quantity is well suited to probe the (non-relativistic) symmetries of the observed band states [36,115]. In order to yield the full information, the photon impact direction was varied between the $\bar{\Gamma} - \bar{H}$ and $\bar{\Gamma} - \bar{N}$ azimuthal planes. Linear dichroism maps are determined from the photoemission intensity of the complete first Brillouin zone by deriving *voxel-by-voxel* the "left-right asymmetry" (analogously to a spin-orbit type spin detector):

$$A_{LDAD}(k_x,k_y,E_B) = [I(k_x,k_y,E_B) - I(-k_x,k_y,E_B)] / [I(k_x,k_y,E_B) + I(-k_x,k_y,E_B)] \qquad (4.11)$$

In order to emphasize the dichroic signal of intense bands it is advantageous to plot the numerator of eq. (4.11), termed the *LDAD signal*, which is also bipolar and can be plotted on a false-color scale. For quantification of the LDAD, we use the asymmetry according to eq. (4.11). By definition, the asymmetry vanishes at the centerline $k_x$=0. For photon impact in the $\bar{\Gamma} - \bar{H}$ or $\bar{\Gamma} - \bar{N}$ azimuth, the asymmetry is derived analogously. The same geometry with photon impact in the $\bar{\Gamma} - \bar{H}$ and $\bar{\Gamma} - \bar{N}$ planes has been used for the photoemission calculations in chapter 5. This way of measuring dichroism is orders of magnitude more effective than the previous approach using conventional ARPES (e.g. [115]).

# 5. Experimental results

## 5.1. Momentum microspectroscopy

The traditional microspectroscopy supposes spectral measurements at a defined microscopic area of the object image. But the momentum microscopy allows performance of such spectroscopy from areas localized in reciprocal space of the object. Local spectra are derived from the 3D data set by extracting energy profiles in a small $k_x - k_y$ interval of typically $3\times10^{-2}$ Å$^{-1}$ size. Spectra for some high-symmetry points on Mo(110) are shown in Fig. 5.1.

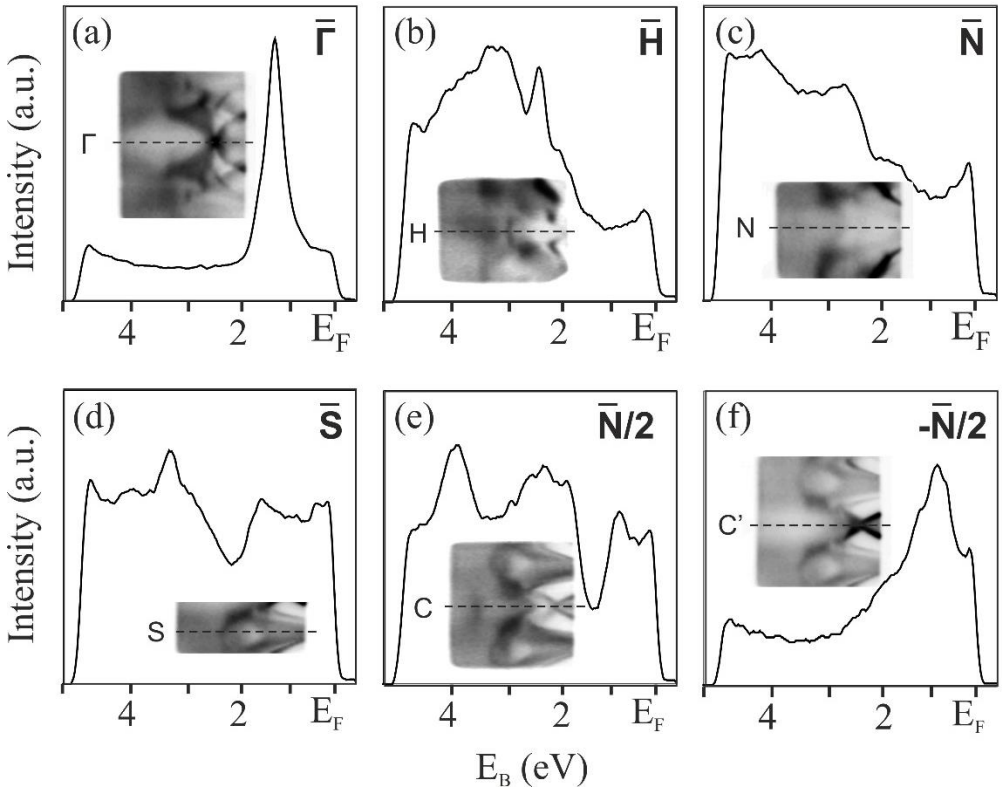


**Fig. 5.1.** Momentum-space microspectroscopy of the Mo(110) surface at several high-symmetry points as denoted in Fig. 5.3 (a,g). The local spectra are extracted in small $k_x - k_y$ intervals with sizes smaller than the dots in Fig. 5.3. The insets in the spectra show the corresponding $E$-$\boldsymbol{k}_\parallel$ sections close to the high-symmetry points. $\bar{\mathrm{N}}/2$ and $-\bar{\mathrm{N}}/2$ are denoted by "+" in Fig. 5.3 (a).

No correction for surface-refraction (so-called "$\theta$-correction") is necessary like in spectroscopy using a hemispherical analyzer. For observation under a fixed angle, the $k_\parallel$-

value varies with kinetic energy due to refraction at the surface barrier. Thus in contrast to ARPES measurements we obtain microspectra at a precise location in momentum space without any data treatment. The power of this novel approach of k-space microspectroscopy is clearly visible in the selection of spectra in Fig. 5.1. The spectrum taken at the $\bar{\Gamma}$-point (spectrum (a)) shows a very intense and sharp feature of the band crossover (see inset). At points $\bar{\mathrm{N}}/2$ (e) and $-\bar{\mathrm{N}}/2$ (f), which is at the midway along $\bar{\Gamma}-\bar{\mathrm{N}}$ the spectra show the linear band crossovers at about $E_{\mathrm{B}}$= 0.77 eV (see below). In conventional spectroscopy local spectra in momentum space (i. e. at a fixed $\Delta\boldsymbol{k}_{\parallel}$value) can be obtained only from many individual scans, applying the θ-correction on each scan. The local spectra at the various high-symmetry points are markedly different. The pronounced, sharp intensity feature in (a) is the Dirac-like crossover point (cf. next section). Spectrum (b), taken at $\bar{\mathrm{H}}$ reveals a narrow, deeper-lying band. Spectra (a), (e) and (f) show the crossing points of two bands with linear dispersion at points $\bar{\Gamma}, \bar{\mathrm{N}}/2$ and $-\bar{\mathrm{N}}/2$, respectively. The strong intensity difference of the linearly-dispersing bands points $\bar{\mathrm{N}}/2$ and $-\bar{\mathrm{N}}/2$ is due to the linear dichroism. Note that the photon energy of 35 eV strongly enhances the spectral weight of all surface resonances. Thus the spectra cannot be quantitatively compared with literature data (like, e.g. [116, 117]) taken at other photon energies.

## 5.2. Band mapping of surface resonance on Mo(110)

A ToF momentum microscope is like a "magnifying glass", looking directly into *k*-space without any data treatment. This is accomplished by combining $(k_x, k_y)$-imaging in the backfocal plane of a cathode objective lens with parallel energy recording of an $E_{kin}$-interval of several eV width. It requires a pulsed photon source and a 3D $(k_x, k_y, \tau)$ image detector (τ denoting the time-of-flight). The $k$-space object under study is thus observed on a linear $\boldsymbol{k}_{\parallel}$-scale (independent on energy, see [92]) and a linear time-of-flight scale that translates into kinetic energy as approximately $E_{kin} = \frac{1}{2} m_e (l/\tau)^2$ ($l$ and $m_e$ being the length of the drift section and the electron mass, respectively) neglecting the flight time in the focusing lens system. Fig. 4.11 illustrates the data acquisition geometry.

All data shown in this chapter correspond to a single data acquisition run of about 20 min. A spatial view of 3D data matrix (i.e. the E-vs-$k$ spectral function) of the surface bands on Mo(110) is shown in Fig. 5.2. The spatial plots under different perspectives (a-f) show the raw $(k_x, k_y, \tau)$-data without any treatment (except setting of the image contrast), retaining the linear time axis. In Fig. 5.2 (a) the time axis was translated into an energy axis which is slightly nonlinear accounting for the relation $E_{kin}$/eV = [1567 ns/τ]$^2$ (valid for 900 mm drift section of

the present instrument neglecting the dispersing contributions of the lens system). The high-energy cut off of the kinetic energy scale is given by the Fermi energy, defining the zero of the binding-energy scale $E_B$ ($E_F$)= 0. This 3D representation of $E$-vs-$k$ in the full SBZ (same data matrix also underlying Figs. 5.3-5.5) was acquired at fixed setting of the $k$-microscope, $h\nu$ =35 eV and a flux of $4\times10^{10}$ photons/sec. Given the single-bunch conditions at BESSY II with its large period (800 ns) of photon pulses, acquisition took 20 min. We note that for an "ideal" period of 200 ns a 3D matrix of this quality can be acquired in a few minutes (exploiting 5 Mcps count rate of the delay-line detector).

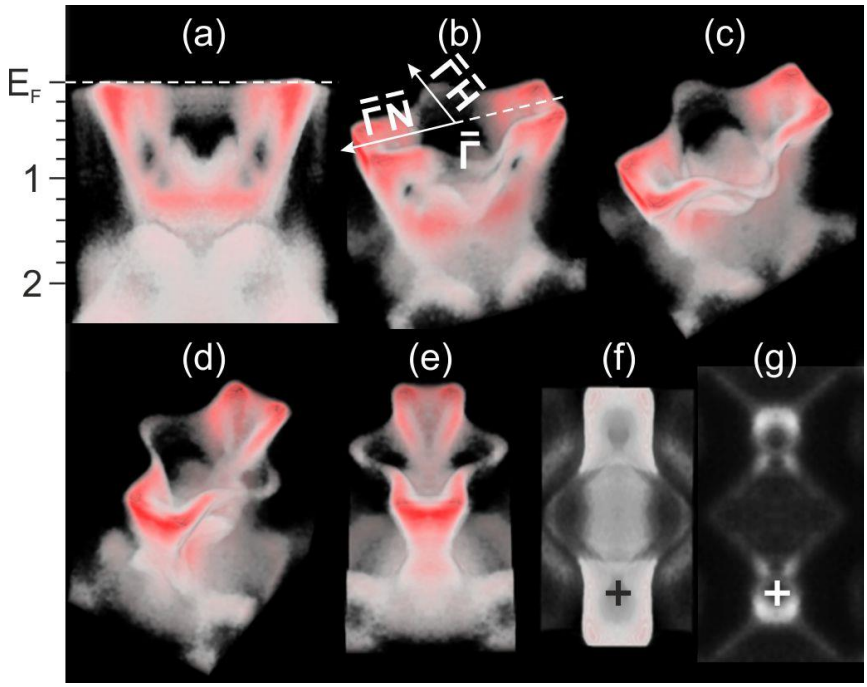


**Fig. 5.2.** 3D data matrix of the E-vs-***k*** spectral function showing the topology of the surface resonances on Mo(110); raw data as observed by the ToF $k$-microscope. The perspective views (a-e) uncover many subtle details of the $k$-space object. Top view (f) and cut through constant energy surface (g) reveal funnels (+) midway along the $\bar{\Gamma}-\bar{\mathrm{N}}$ line. Binding-energy scale and $k_\parallel$-directions are denoted in (a,b), red color marks enhanced intensity.

The perspective views reflect the $C_{2v}$ symmetry and reveal several interesting details of the topology: we immediately recognize the linearly-dispersing outermost boundaries of the $k$-object in views (d,e), the holes along the $\bar{\Gamma}-\bar{\mathrm{H}}$ direction in (a,b), the narrow elongated waist of the object in (e), the two funnels (+) midway $\bar{\Gamma}-\bar{\mathrm{N}}$ (termed $\bar{\mathrm{N}}/2$) in top view (f) and section (g) and the onset of bulk bands, appearing as diffuse structures at $E_B$ >1.4 eV. As a consequence of the contrast setting, the widths of all band features appear enhanced in this plot. True widths are visible in Figs. 5.3-5.5.

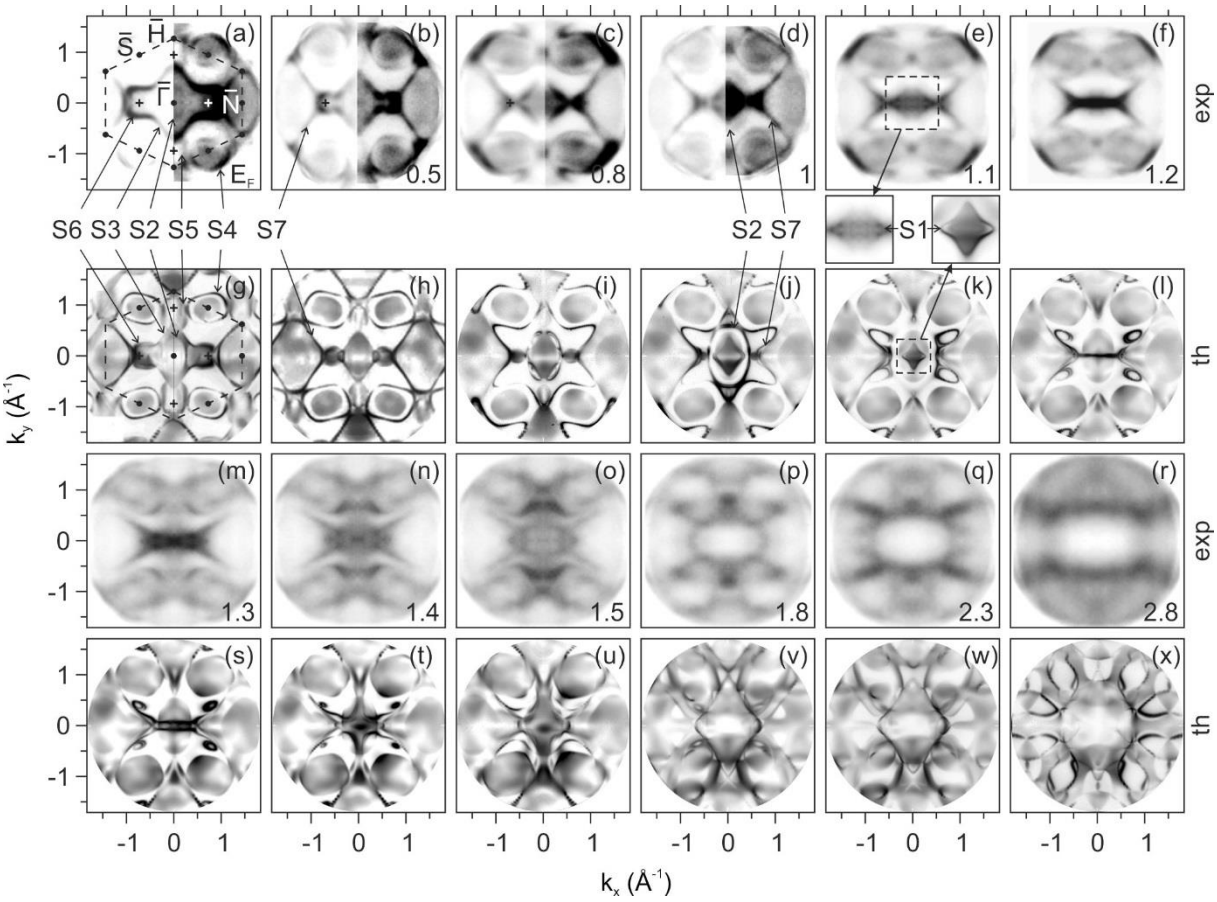


**Fig. 5.3.** Constant-energy sections through the 3D data matrix representing momentum distribution images at the respective binding energy $E_B$ (in eV), as given in the panels. Experimental momentum patterns (a-f above and m-r below the crossover line) and corresponding theoretical ones (g-l and s-x, respectively) are shown together. The sequence spans from $E_F$ (a,g) via the crossover line at $E_B$= 1.2 eV (f,l) to $E_B$= 2.8 eV (r,x). The surface Brillouin zone and symmetry points are marked in (a,g). S1-S7 denote surface states and resonances. The left and right halves of (a-d) are shown with two different contrast settings to emphasize different features.

In order to analyse the electronic structure in more detail, sections ($E$ = const. or $E$-vs-$\boldsymbol{k}$) can be cut through the 3D data matrix. Fig. 5.3 (a)-(f) shows measured *constant energy sections* and (g)-(l) the corresponding theoretical sections between the Fermi energy (a,g) and the pronounced intense line at $E_B$= 1.2 eV, visible in (f,l). The experimental and theoretical sequences are continued in (m-r) and (s-x), respectively, in the energy region between 1.3 eV and 2.8 eV, where pronounced bulk-band features occur. The measured 3D object has been sectioned into 100 energy slices, 12 of which are shown in Fig. 5.3. The linear dichroism is eliminated, i.e. the sections show the denominator of eq. (4.11). Corresponding binding energies

(in eV) are given at the bottom of the panels. The SBZ with high-symmetry points as well as the bands S1-S7 are labelled and marked in the top row. The overall agreement between experiment and calculation is very good, deviations mainly concern the relative intensities of bands and the exact positions of hybridization gaps and band maxima (see below). The total numbers of observed and calculated bands and their principal behavior are identical.

Bands S2 and S3, defined in Fig. 2.7 appear as the elliptical feature around the $\bar{\Gamma}$ point (weakly visible in (a,g), more pronounced in (d,j)) and the diamond centered at $\bar{\Gamma}$, respectively. S4 is the elliptical band around the $\bar{S}$-point. It occurs also for W(110), where it carries a marked "circular" spin texture [118]. S5 is a weakly-visible band close to the $\bar{H}$ point. The feature with the highest intensity in the $E_F$ (i.e. $E_B = 0$) section is the horse-shoe shaped band S6, located between $\bar{\Gamma}$ and $\bar{N}$ (a). Finally, S7 is a diamond-shaped band around $\bar{N}$ (b,h). These pronounced patterns and the four $\bar{S}$-points are eye-catching and have been observed before [23,24,119-122]. Although Fig. 5.3 (a) seems to suggest a closed pattern, S3 and S6 have different symmetry character. These bands separate the continuum of bulk states (grey area inside) from the bandgap (bright area outside) as visible both in experiment (a) and theory (g). The quite complicated behavior of the partial bandgap is nicely visible in the sequences (a-f) and (g-l). The anomalous band S1 shows up only in the vicinity of 1.2 eV, as anticipated from Fig. 2.7. It appears in terms of a narrow ellipse above 1.2 eV (e,k and details as insets), a single intense line running along the $\bar{\Gamma} - \bar{N}$ direction at the crossover energy (f,l) and two parallel lines at 1.3 eV (m,s).

Bands S1, S3, S6 and S7 turned out to be quite robust against surface contamination, i.e. they were visible for a full day after preparation. For W(110) the photoemission signals from the analogous states are theoretically predicted to persist in the hard X-ray range [18], giving evidence of their existence in several layers. In contrast, S2, S4 and S5 disappear rapidly with increasing residual gas adsorption after less than one hour at $10^{-10}$ mbar. The latter observation is in agreement with results for W(110) by Kevan [122] and Miyamoto et al.[16,19] who showed that S2 and S4 derive from surface dangling bonds by exposing the surface to small amounts of adsorbates. The likely reason for the longer lifetime of S3, S6 and S7 (the marked contour at $E_F$) is that these states have the character of surface resonances. S1 is the surface resonance exhibiting linear energy dispersion and, according to theory, a spin-polarization structure which is reminiscent of topological surface states. True topological surface states are stable due to their topological protection.

With increasing binding energy (a-d) we observe a contraction of the intense patterns S3 and S6. It is remarkable that the horse-shoe feature S6 contracts symmetrically to a point marked by + in panels (a-c). This was already recognized in Fig. 5.2 (d-g). The oval bands S2

(around $\bar{\Gamma}$) and S4 (around $\bar{S}$) expand with increasing binding energy. S7 moves towards $\bar{\Gamma}$ and unifies with S4, developing into a six-fold star markedly visible in theory (i,j) and weaker in experiment (c,d). This star runs along the outer borderline of the bandgap as visible in (i).

In order to visualize band dispersions in detail, we extracted $k_x$=*const.* sections (in *E-k* planes), the orientation is sketched in Fig. 5.4 (a). In the first row, (b) and (c) show the experimental and theoretical sections in the $\bar{\Gamma} - \bar{H}$ symmetry plane ($k_x$= 0). The calculated section shows the band crossing in the center of the bandgap at 1.2 eV and the continuation of the band in the bulk continuum, as discussed in Fig. 2.7. The left and right halves of (c) have been calculated for excitation by p- and s-polarized light, respectively. The experimental section (b) does not resolve the details of the crossing point in the bandgap (width 120 meV), since the total energy resolution was only 80 meV in this measurement. At the crossing point we recognize only an intense spot. However, the extension of S1 into the bulk-continuum region is clearly visible as broadened v-shaped feature above the crossing point inside of the parabolic-shaped bulk continuum in (b), very similar as in the calculation (c). The downward-dispersing band S4 appears weaker in experiment than predicted by theory. Surface resonance S3 forms the borderline between the region of bulk-continuum states around $\bar{\Gamma}$ and the bandgap.

The bulk-continuum region has its minimum in the center of the SBZ and its shape resembles a paraboloid. In all directions the gap increases with increasing distance from $\bar{\Gamma}$. Therefore it is interesting to look at sectional planes parallel to $\bar{\Gamma} - \bar{H}$ but displaced from the $\bar{\Gamma}$-point. The experimental cuts (d), (e) and (f) correspond to $k_x$=0.15, 0.25 and 0.3 Å$^{-1}$, respectively. Now the experiment resolves the linear dispersion of S1. In the different perspective of the constant-energy sections this phenomenon was also visible (Fig. 5.3 (e),(m)). The character of S1 changes from surface-resonance-like in the bulk continuum to surface-state-like in the gap. At its upper end, S1 ends by hybridization with the downward-dispersing band S4 (contrast in detail region in (d) enhanced to emphasize S4).

With increasing distance from $\bar{\Gamma}$, the crossing point of S1 slightly increases in energy (f,m) and beyond 0.3 Å$^{-1}$ the crossing point disappears and S1 fades out. Sections (d,e) reveal a crossing and linear dispersion of S1 over an energy range of about 500 meV. The bandgap has increased in this off-$\bar{\Gamma}$ region, allowing S1 to develop its linear dispersion in a larger energy range. The anomalous band extends over a range between $\bar{\Gamma}$ and $k_x \approx$ 0.3 Å$^{-1}$ (f), where S1 appears weaker, but the crossing point is still visible as intense spot. The upper part of the v-feature in (d-f) is the diamond-shaped band S3 as visible in the scheme in (a). It is separated from S1 by a hybridization gap, marked by the circle in (e). The theoretical sections (k-q) show further details: when the bulk continuum retracts, S1 at first runs along the border of the bulk

continuum (k) and then extends into the bandgap (l,m), making contact with S4. For W(110) the behavior is identical, except that this contact with S4 is already visible in the $\bar{\Gamma}-\bar{H}$ symmetry plane (cf. Fig. 2.7).

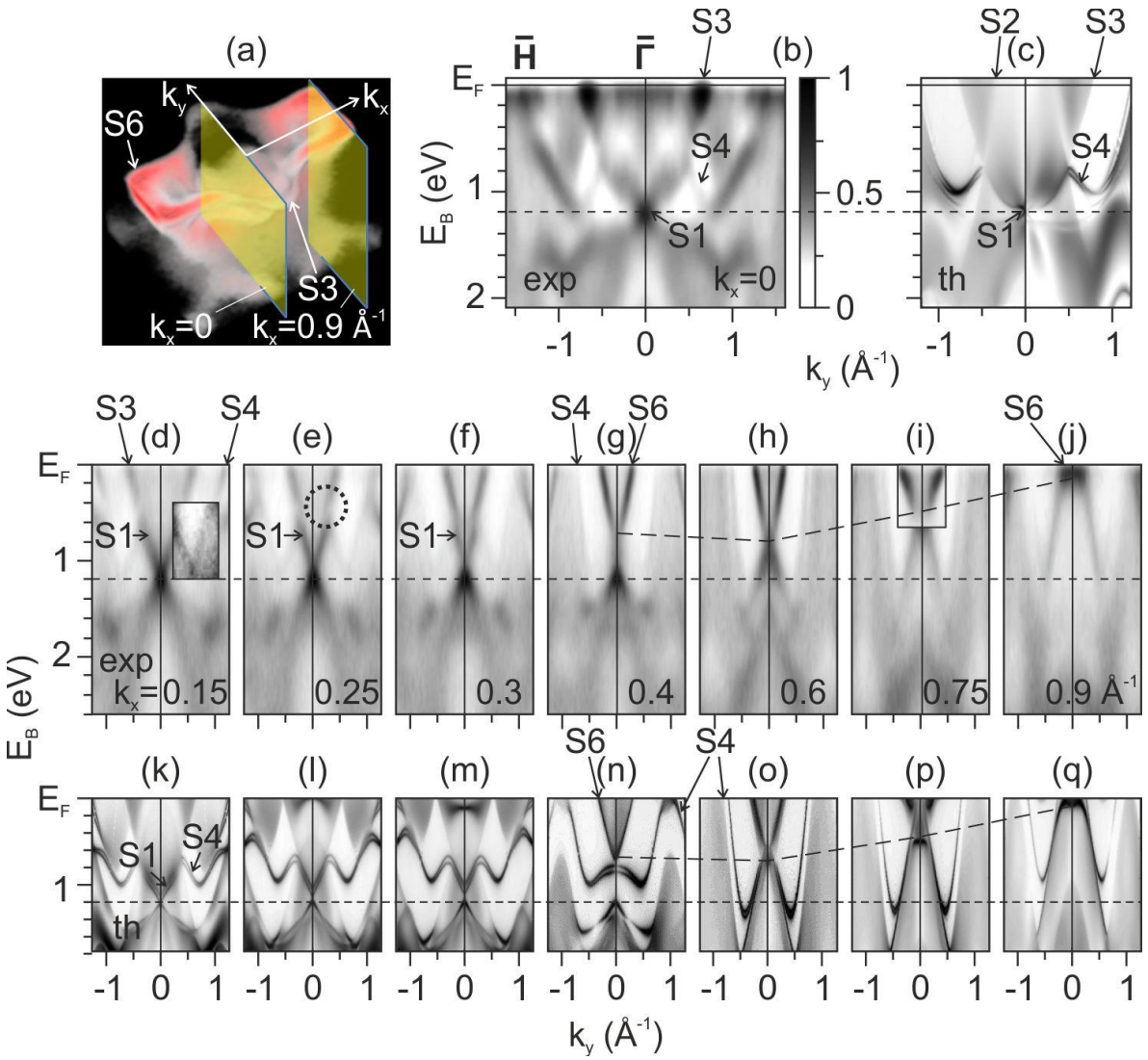


**Fig. 5.4.** $k_x$=const. sections through the 3D data matrix as sketched in (a). (b) experimental and (c) theoretical section in the $\bar{\Gamma}-\bar{H}$ symmetry direction (for details of (c), see Fig. 2.7). (d-j) experimental and (k-q) theoretical sections parallel to $\bar{\Gamma}-\bar{H}$ with increasing distance from the $\bar{\Gamma}$-point between $k_x$=0.15 Å$^{-1}$ (d,k) and 0.9 Å$^{-1}$ (j,q), corresponding to the outermost rim of S6. In (d,i) the contrast is locally modified to enhance visibility of bands S4 and S6.

At 0.4 Å$^{-1}$ the situation suddenly changes: in (g,n) the v-feature reaching to $E_F$ is more intense, indicating that the surface resonance S6 has been reached, about midway of the two planes denoted in (a). S6 is the most intense band at 35 eV photon energy. In the 3D plot (a) it appears as a funnel with horseshoe-shaped upper rim at $E_F$, almost circular cross section at

higher binding energies (Fig. 5.2 (f),(g)) and linearly dispersing walls. At its bottom the funnel contracts to a point at $E_B$=0.77 eV and $k_x$=0.6 $Å^{-1}$ (h,o). Below this point, S6 is linearly extended and connects to surface state S4 (the oval band around $\bar{S}$). S6 lies completely in the bulk bandgap. The pronounced v- shaped features in sections (g,n), (h,o) and (i,p) and the straight horizontal line in (j,q) are cuts through this funnel. Its upper part with linearly-dispersing walls was already recognized in the perspective views of Fig. 5.2. Due to the presence of the bulk continuum, the funnel is truncated at its inner side (towards $\bar{\Gamma}$). The sequence ends at $k_x$=0.9 $Å^{-1}$ (j,q), corresponding to the outermost rim of S6, as sketched in (a). In the calculations S6 shows an unusual spin texture that will be investigated experimentally in the future. Due to its contraction to a point, its linear dispersion and its unusual spin texture (not shown here) we conclude that band S6 is no conventional surface state.

The topology of the E-vs-$k$ spectral function is further elucidated by $E - k$ sections in the perpendicular direction ($k_y$= const). A sequence of such sections is shown in Fig. 5.5. Panel (a) denotes the orientation of the sectional planes, (b) shows details of calculated constant-energy sections close to the crossing point at 1.2 eV ($E_B$ given below each section with stepwidth 25 meV). The experimental and calculated sections in the $\bar{\Gamma} - \bar{N}$ symmetry direction are shown in (c) and (g), respectively. Sections close to this plane are shown at $k_y$= 0.04, 0.08 and 0.12 $Å^{-1}$ (d-f) and $k_y$= 0.02, 0.04 and 0.06 $Å^{-1}$ (h-j) for experiment and theory, respectively. In order to show the behavior more clearly and accounting for the limited resolution, the experimental sequence is plotted with twice the $k_y$-stepwidth. In (c) we see S2, the oval band around $\bar{\Gamma}$, the paraboloid-shaped band S3 and a pronounced outer contour, consisting of bands S6 and S7, ending in a flat bottom with very high intensity at $E_B$= 1.2 eV which obviously corresponds to the intense point in (b), identified as anomalous band S1. We note that S2 was studied in much detail by Valla et al. [70] with emphasis on the signature of many-body effects.

With increasing $k_y$ the intense bottom line splits into the upper and lower branch of S1 as indicated by the vertical arrows in (d-f) and the insets in (h-j), as well as in the sequence shown in (b). The low intensity close to the $\bar{\Gamma}$-line is due to the symmetry selection rules (projection of the electric vector on the surface normal is zero for s-polarized light). Comparison with Fig. 5.5 reveals that the "Dirac-like" state is highly anisotropic, i.e. only slightly curved in the $\bar{\Gamma} - \bar{N}$ symmetry direction but with large slope along $\bar{\Gamma} - \bar{H}$. This principal behavior is identical to the case of W(110) [16,19].

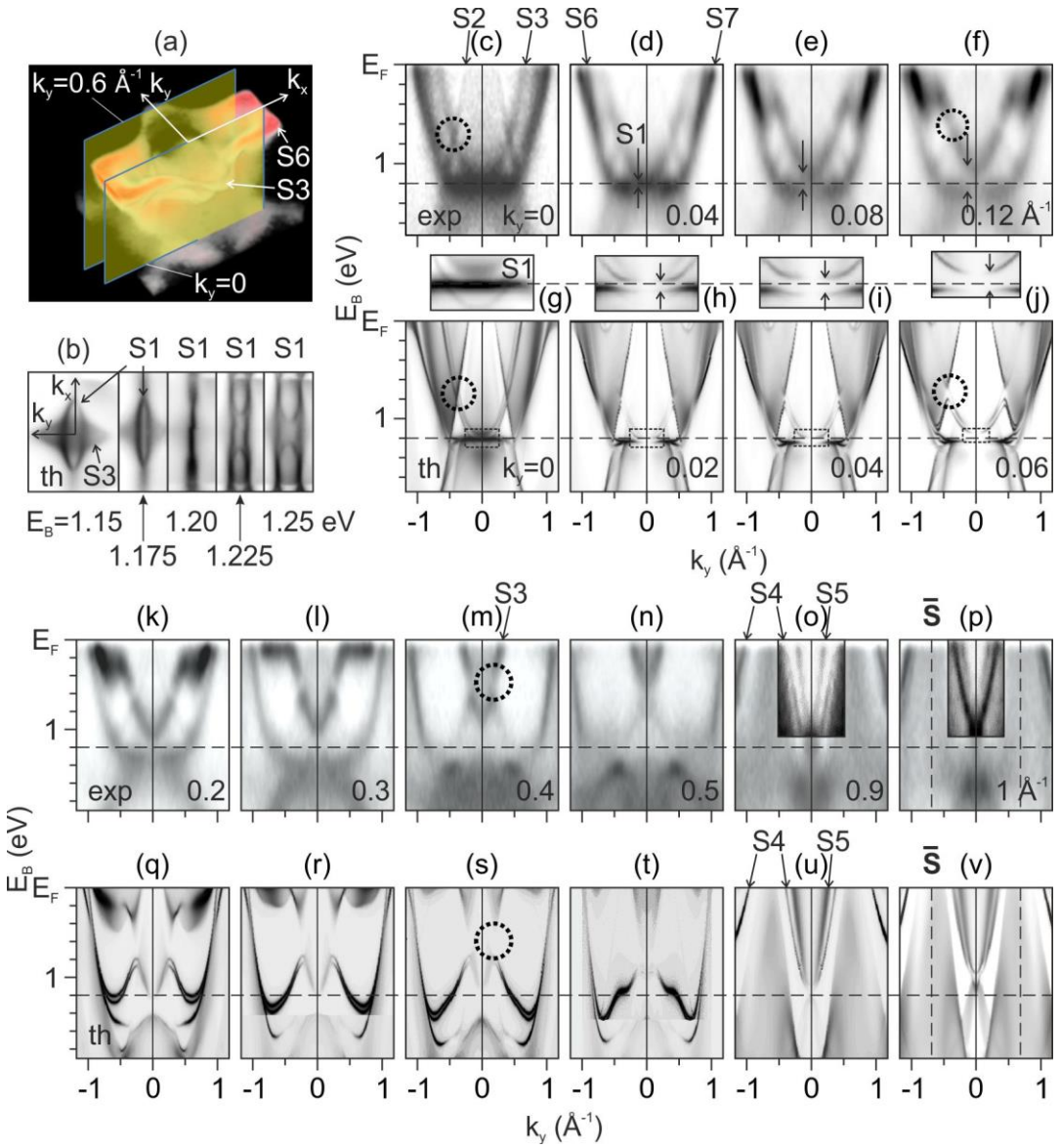


**Fig. 5.5**. $k_y$= const**.** sections through the 3D data matrix as sketched in (a). Panel (b) shows details of constant-energy sections very close to the crossover line in the range of $E_B$= 1.2 ± 0.05 eV. (c-f) experimental and (g-j) theoretical sections in and close to the $\bar{\Gamma} - \bar{N}$ symmetry direction. Details marked by dotted rectangles in panels (g-j) are shown enlarged as insets. The $k_y$- stepwidth is 2x larger in the experimental sequence due to the limited resolution. (k-p) experimental and (q-v) theoretical sections at larger distances from the $\bar{\Gamma}$-point between $k_y$= 0.2 Å$^{-1}$ (k,q) and 1 Å$^{-1}$ (p,v), corresponding to the section across the $\bar{S}$-points (dashed lines in (p,v)). In (o,p) the contrast is locally modified to enhance visibility of bands.

Along with the splitting of S1 around 1.2 eV, the crossing of S2 and S3 (circles in c,g) is lifted and a hybridization gap opens (circles in f,j). The same behavior was found for W(110) and is discussed in detail in Ref. [20]. S2 is almost spin-degenerate. In contrast, S3 representing

the upper continuation of S1 shows only one spin component for each $k_x$ direction. Thus only one spin component of S2 hybridizes, while the opposite spin component of S2 does not hybridize with S3/S1, cf. Fig. 2.7 (c),(d). As a consequence a hybridization gap opens for one spin component only. An opposite spin polarization is expected within this hybridization gap compared to the corresponding polarization of S1/S3.

Sections (k-p) (experiment) and (q-v) (theory) show the continuation further away from $\bar{\Gamma}$, between $k_y$= 0.2 (k,q) and 1 Å$^{-1}$ (p,v), corresponding to the section through the $\bar{S}$–points (denoted as dashed vertical lines). In the sequence (e,f,k) we see how the side wall of the funnel of S6 runs upwards, reaches the Fermi energy (horizontal branch at $E_F$ in (l)) and disappears (m). The top part in (m) is the diamond-shaped band S3, separated by a hybridization gap (circle in (m,s)) from the residue of S1. Close to (n,t) we reach the corner of the diamond (see also sketch in (a)) where the intense features of S6 and S7 have disappeared. Finally, sections (o,p,u,v) are dominated by S4 and S5 in the vicinity of the $\bar{S}$–point. The outer branches of S4 visible at the top left and right corners in (o,p,u,v) belong to the second SBZ on the other side of $\bar{S}$. They appear with enhanced intensity, a well-known fact in ARPES experiments [123]. The agreement between experiment and theory is excellent, even concerning subtle band details and trends of intensities. Finally, we note that the pronounced diamond-shaped feature derives from the Fermi surface pattern as we have studied in later measurements for W(110) (see also outlook on p. 82).

## 5.3 Linear dichroism in the photoelectron angular distribution (LDAD)

For non-magnetic systems circular and linear dichroism in the photoelectron angular distribution (CDAD [34] and LDAD [36]) arise due to a dissymmetric spatial arrangement of (i) the quantization axis of the orbital momenta of the initial state, (ii) the photon impact direction and (iii) the photoelectron momentum. CDAD requires a chiral geometry [124] and LDAD a dissymmetric orientation of the electric vector with respect to the initial-state orientation [125,126]. Our photon beam is *p-polarized* and for the example shown below the $\bar{\Gamma} - \bar{H}$ direction lies in the plane of incidence in Fig. 4.11. The in-plane ($E_y$) and out-of-plane component ($E_z$) of the electric vector point along the *–y* and *+z* axis. If the *x-z* plane is a mirror plane of the sample, the tilted ***E***-vector breaks this mirror symmetry, thus giving rise to linear dichroism. The (non-magnetic) system is no longer invariant under the mirror operation, but we have to reverse the phase relation of $E_\parallel$ and $E_\perp$, too. With *tan*(22°)≈0.4 (22° is the angle between ***E*** and *z*), the photon operator can be written as *z+0.4y* for $k_y$< 0 and *z-0.4y* for $k_y$> 0. Since the momentum microscope acquires the full $k_x - k_y$ plane

simultaneously, the LDAD asymmetry pattern can be determined in a single measurement from the intensity patterns of the $k_y > 0$ and $k_y < 0$ half planes *voxel-by-voxel* according to eq. (4.11). This is much easier than the procedure used in earlier work [115,124].

The evaluation of the LDAD-asymmetry in the 3D data matrix of Fig. 5.2 (see also Figs. 5.3-5.5) yielded surprisingly rich patterns. A detail, the *k*-region of the triangle $\bar{\Gamma} - \bar{S} - \bar{N}$ at 4 energies between 0.2 and 0.8 eV is shown in Fig. 5.6. The LDAD-asymmetry is color coded between red (+70%) and blue (-70%). The first and last rows show measured and calculated intensities, the second and third row measured and calculated LDAD asymmetries, respectively. High asymmetries up to 70% occur, clearly associated with the various band states. The upper half-plane above the $\bar{\Gamma} - \bar{N}$ line shows predominantly red color (denoting higher intensity than in the lower half-plane), but also blue color (denoting lower intensity than in the lower half-plane). The latter case is surprising at first sight, because it is opposite to the classical expectation: intensities should be larger in the sector with positive projection of $\boldsymbol{E}$ (denoted by the perspective arrow $\boldsymbol{E}$). Obviously, the classical picture is not generally valid, so we have a brief look into the quantum-mechanical origin of LDAD.

Starting from an atomic-like orbital in isotropic space, the phototransition leads to several outgoing partial waves excited either by the *z*-part or by the *x*-part of the operator $z \pm 0.4y$ (governed by the symmetry selection rules). Owing to the coherence of partial waves in the total final-state wavefunction, interference terms show up. These contain radial matrix elements and cosines of corresponding phase-shift differences. Note that there is only a subtle difference to the case of circularly polarized light with photon operator $z \pm i0.4y$ (for photon impact in the *x*-*z* plane): the CDAD asymmetry contains the same interference terms as the LDAD, except that due to the phase factor $i = e^{i\pi/2}$ sine functions of the phase-shift differences enter (for details, see [34]). The information content of LDAD and CDAD in the non-relativistic case is identical!

The studied surface resonances have $\Sigma_1(d_{z2})$, $\Sigma_2(d_{xy}, d_{x2-y2})$ and $\Sigma_3(d_{xz}, d_{yz})$ symmetry (see, e.g.[16,19]). The photoemission cross section is governed by Fermi's Golden Rule, e.g. for an atomic-like $d_{z2}$-orbital $d\sigma/d\Omega \propto |\langle f\,|z \pm 0.4y|d_{z2}\rangle|^2$. The dipole operator excites 4 final-state partial waves, two *p*- and two *f*-waves. The angular integrals of the spherical harmonic of the initial state ($Y_{20}$) with those of the final states ($Y_{10}$, $Y_{1\pm1}$, $Y_{30}$ and $Y_{3\pm1}$) contain interference terms between the four partial waves with their three phase differences. These have opposite signs for + and – in the operator. In turn, the complete angular distribution pattern is rotated about the *x*-axis, clockwise for operator $z+0.4y$ ($k_y < 0$) and counterclockwise for $z-0.4y$ ($k_y > 0$) (for details, see [35,127]). This rotation of the

$d\sigma/d\Omega$-pattern caused by the interference terms of different partial waves is the essence of the LDAD. Sign and size thus depend essentially on the initial-state band symmetry and relative phases of the final-state partial waves. Previous work on graphite [128] and Pd [129] revealed that this atomic-like picture is modified, but the interference effect persists in photoemission from crystalline samples and can lead to very high LDAD and CDAD asymmetries.

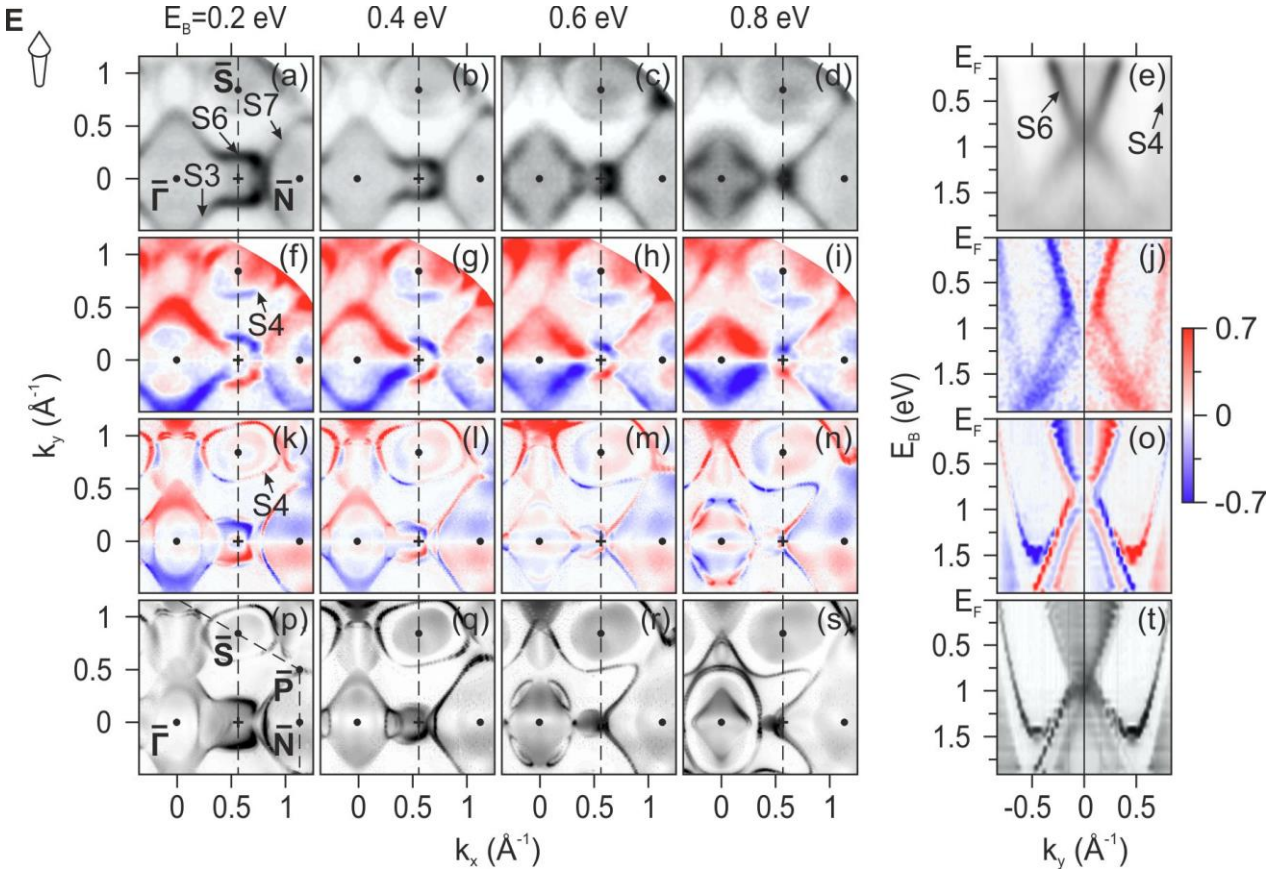


**Fig. 5.6.** Sequence of measured $E$=const intensity sections (a)-(d) and corresponding LDAD patterns (f-i) in the $\bar{\Gamma} - \bar{S} - \bar{N}$ region at binding energies between 0.2 and 0.8 eV. The calculated LDAD and intensity patterns are shown in (k)-(n) and (p)-(s), respectively. The midway point of $\bar{\Gamma} - \bar{N}$ is marked by +. Bipolar color shows the linear dichroism asymmetry defined by eq. (4.11), quantified by the color bar. The electric field vector ***E*** (marked by the top left arrow) lies in the plane spanned by the $\bar{\Gamma} - \bar{H}$ direction and z. Right column, $E$-$k$ sections at $k_x$= 0.6 Å$^{-1}$, along the dashed lines in the left panels.

For the chosen geometry, the orientation of ***E*** breaks the up-down symmetry. According to the definition (eq. (4.11)) the asymmetry vanishes along the horizontal $\bar{\Gamma} - \bar{N}$ symmetry line. Now we consider the colors of the bands above this line. S3 and S7 appear

in red (corresponding to the classical expectation), whereas S6 and the diffuse intensity around the $\bar{S}$-point appear in blue. Band S4, the oval band around $\bar{S}$ shows a particularly interesting behavior because it changes its LDAD sign and size along the circumference of the band, from blue at its lower rim to red on the left and right of the $\bar{S}$-point. The agreement between experiment and theory is very good at $E_B$= 0.2 and 0.4 eV. In particular, the fine structure of the horse-shoe pattern of S6 agrees perfectly well. Comparing the 0.6 and 0.8 eV patterns, we recognize differences, especially close to $\bar{\Gamma}$. These are caused by the fact that surface state S2 and the sixfold star composed of S4 and S7 appear only weakly in the experiment. Therefore their measured LDAD signature is partly masked by the intense diamond-shaped band S3 close to $\bar{\Gamma}$ and by the background for the weak band features (h,i), whereas the LDAD of S2 and the sixfold star is strongly visible in the calculation (m,n). The right column in Fig. 5.6 shows sections along the dashed lines marked in the right panels. In these $E$-$k_y$ sections, connecting two $\bar{S}$-points, we find reasonable agreement between experiment and theory for the main features of S6 and S4.

The LDAD-patterns in Fig. 5.6 allow to draw conclusions about the non-relativistic band symmetries. The diamond-shaped central feature S3 and the horse -shoe shaped pattern S6, being the most intense features of the whole surface band structure at 35 eV photon energy show different signs of LDAD, i.e. they have different initial-state symmetries. The varying LDAD of S4 gives evidence that the angular-momentum composition of this band state varies along the circumference. We attribute this to $\Sigma_3$-symmetry and variation of the $d_{xz}, d_{yz}$-composition, depending on the in-plane angle around the circumference around $\bar{S}$. For the special behavior of S4 we find good agreement between experiment and theory in intensity and dichroism.

## 5.4. Band mapping and circular dichroism of oxygen-covered Mo(110)

Adsorption of oxygen on Mo(110) results in various superstructures. Upon exposure to oxygen at room temperature atomic chemisorption takes place [130,131]. Heating molybdenum in oxygen at temperatures of around 1300℃ results in molybdenum oxide formation [132,133].

Depending on the oxygen dose, exposition to oxygen at room temperature leads to the formation of a quarter monolayer coverage (2×2 superstructure) at $5\times10^{-7}$ mbar·sec exposure; a half monolayer (1×2 superstructure) at exposures below $8\times10^{-5}$ mbar·sec or three quarter monolayer (inverse 2×2 superstructure) at exposures between $8\times10^{-5}$ and $8\times10^{-3}$

mbar·sec. At higher exposures a more complicated superstructure of oxygen was found [130,131].

In the laboratory experiment the exposure was 2 minutes at $2\times10^{-8}$ mbar corresponding to a dose of $1.2\times10^{-6}$ mbar·sec. This should result in the 2×2 superstructure. This assumption was confirmed by LEED investigations. The LEED pattern of the clean Mo(110) surface (Fig. 5.7(a)) changes to the pattern which matches the 2×2 oxygen superstructure (b) seen in previous experiments [130,134]. For higher coverage, patterns (c-f) have been observed.

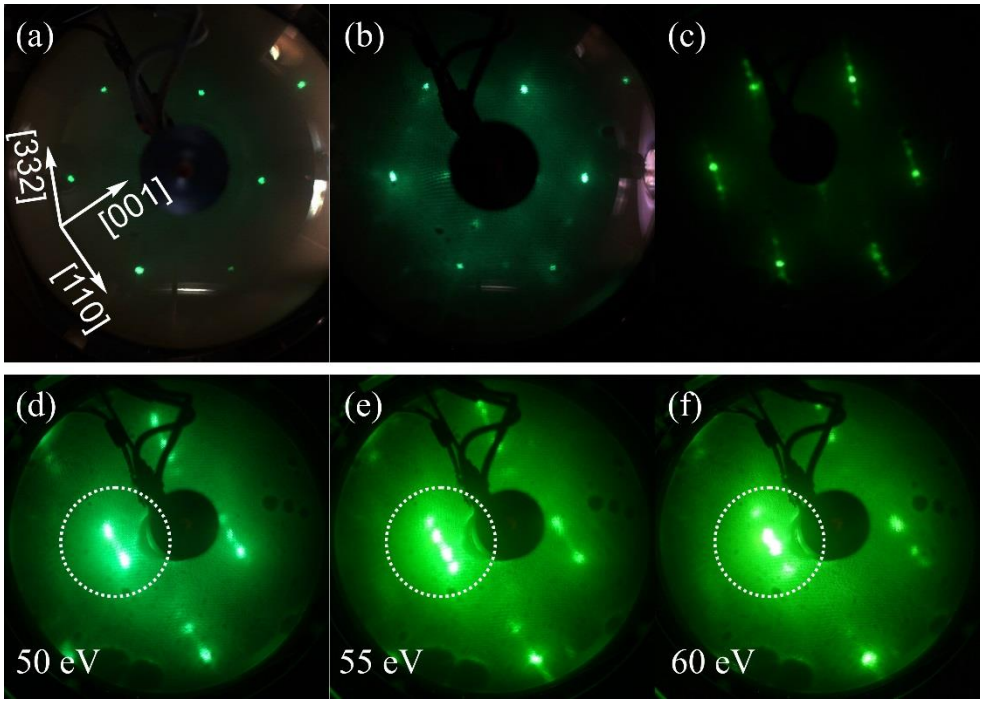


**Fig. 5.7.** LEED patterns of a clean Mo(110) surface (a), oxygen $2 \times 2$ superstructure on Mo(110) (b), epitaxial molybdenum oxide grown on Mo(110) (c), taken at 85 eV electron scattering energy. Panels (d)-(f) represent patterns from a facetted oxidized Mo(110) surface taken at 50, 55 and 60 eV, respectively.

A 3D representation of the observed band structure pattern is shown in Fig. 4.2. The $k_x - k_y$ Fermi cut and $E_\mathrm{B} - k_x$ and $E_\mathrm{B} - k_y$ cuts of O/Mo(110) in comparison with clean Mo(110) are presented in Fig. 5.8. The field of view becomes narrower with adsorption of oxygen, because the work function increases from 4.95 to 5.4 eV, as measured by the change of the width of the energy range. Consequently, the accessible $k_\parallel$-range also shrinks.

The results presented here are obtained with 2PPE. Therefore the observed band pattern differs from the one measured with excitation by synchrotron radiation. Particularly, one observes a new state labelled S'.

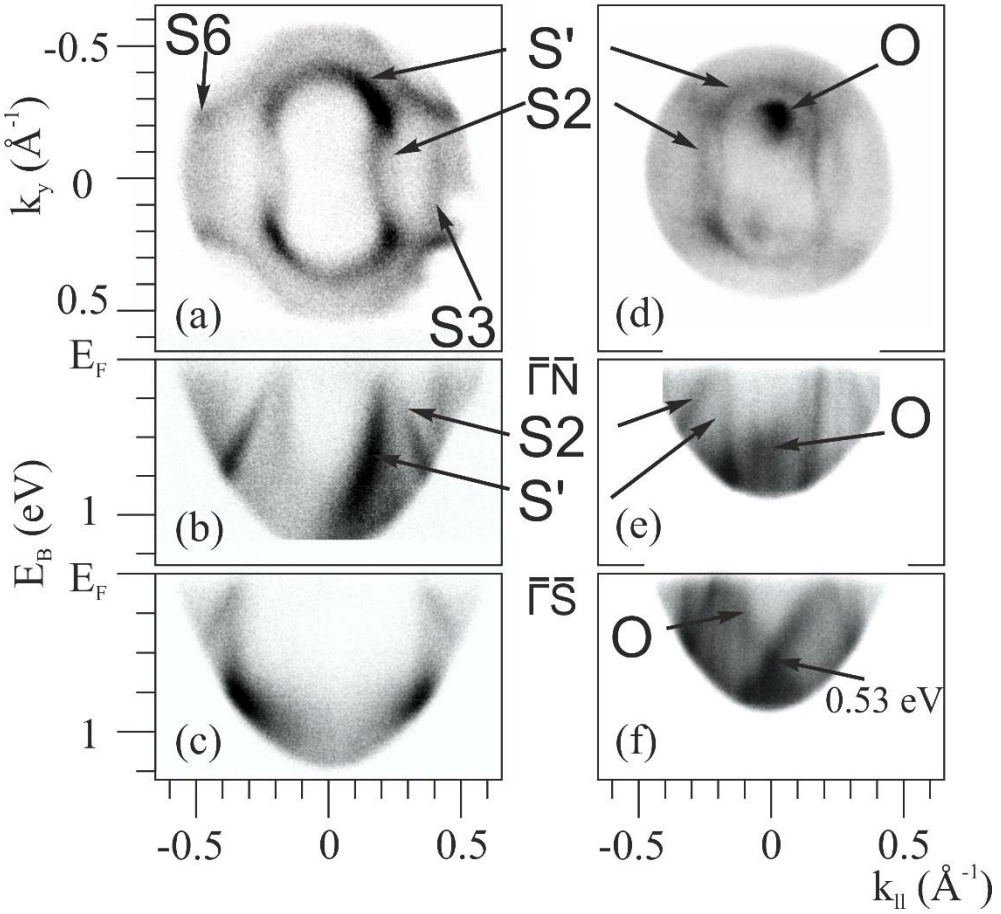


**Fig. 5.8.** Comparison of the $k_x - k_y$ cuts through the Fermi surfaces and $E_B - k_{\parallel}$ sections for clean Mo(110) (left row, a-c) and the oxygen induced $2 \times 2$ superstructure on Mo(110) (right row, d-f). Measurements were performed via 2PPE with circularly polarized Ti:sapphire laser excitation ($2h\nu$ = 6.2 eV).

In the visible k-region the band structure pattern for the O(2×2)/Mo(110) surface particularly resembles the one of clean Mo(110) [134]. It shows the same elliptical feature S' of the same shape but a bit smaller size, which seems to be even more narrow and sharp for the oxidized surface. In contrast, the band S2 (our indicator for surface cleanliness) is suppressed by the adsorbate, as was already mentioned in chapter 4.1. The features S3 and S6 at the edge of

the field of view are also absent for the oxygen-covered surface. Instead, another feature labelled "O" appears. After moderate heating to about 600 K, the S2 band appears again.

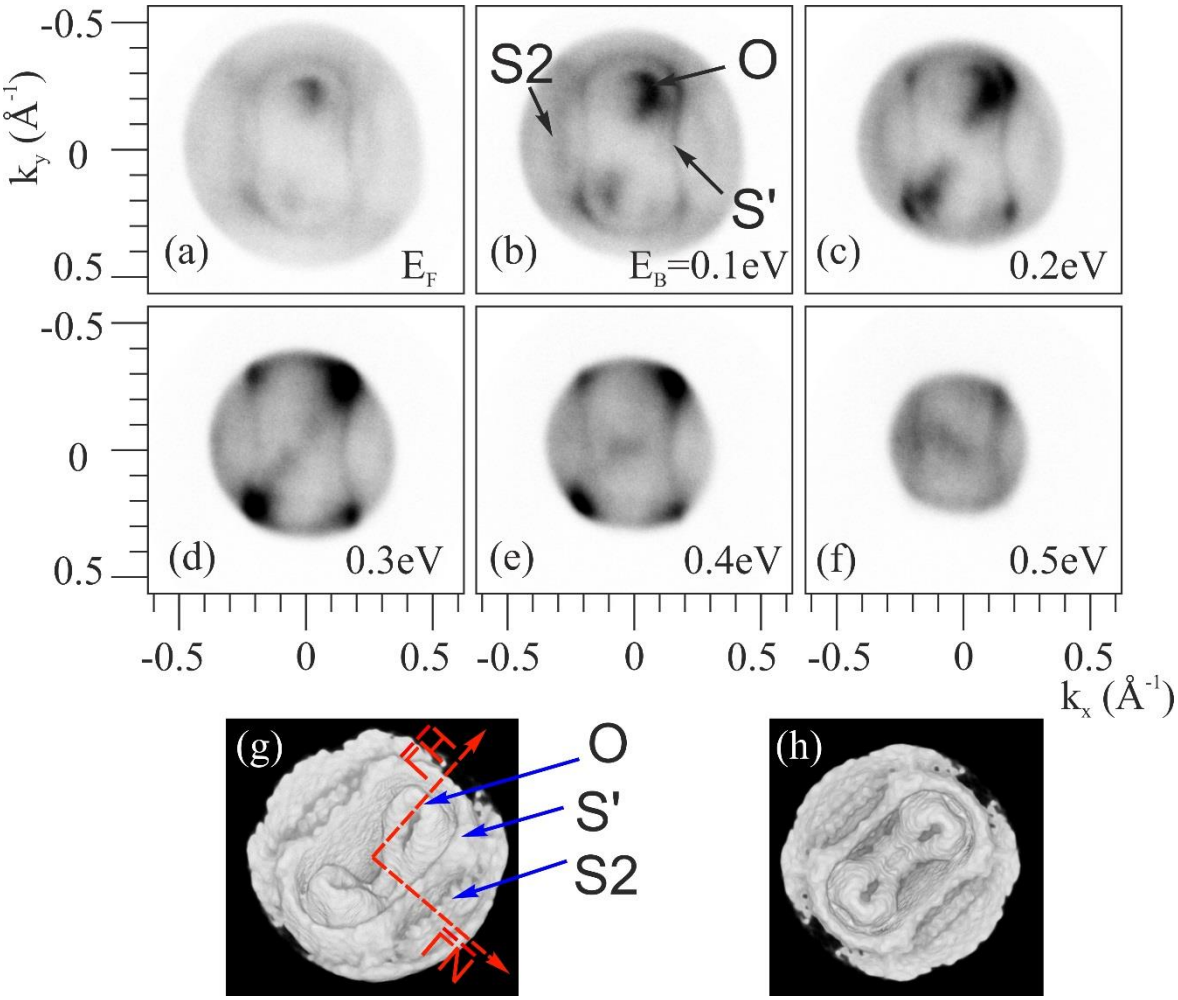


**Fig. 5.9.** $k_x - k_y$ sections of Mo(110) with $2 \times 2$ oxygen superstructure for $E_B$ from 0 to 0.5 eV with steps of 100 meV (a)-(f), respectively. Symmetrized spatial representation (g-h). (2PPE at $2h\nu$ = 6.2 eV)

The oxygen-induced state O has not been observed in previous ARPES experiments on 2×2 O/Mo(110). It has a shape close to two deformed cones with tips slightly above the Fermi edge and opening towards higher binding energies. Due to dichroism they show up only partially. In Fig. 5.8 (d),(f) it can be seen that they touch each other and cross at the $\bar{\Gamma}$ point at $E_B$ =530 meV. Approximately at the same energy they touch the S2 state on the other side of the cones (Figs. 5.8, 5.9). Fig. 5.9 presents constant energy sections for binding energies from $E_F$ to 500 meV in steps of 100 meV. Here it is evident that the visible part of the conical feature

O rotates clockwise around the cone axes on both sides with increasing binding energy. The observed k-pattern appeared to stay in $3\times10^{-10}$ mbar vacuum for days, except the very sensitive band S2. The chemisorbed oxygen provides a protective coating against surface contamination by rest-gas adsorption.

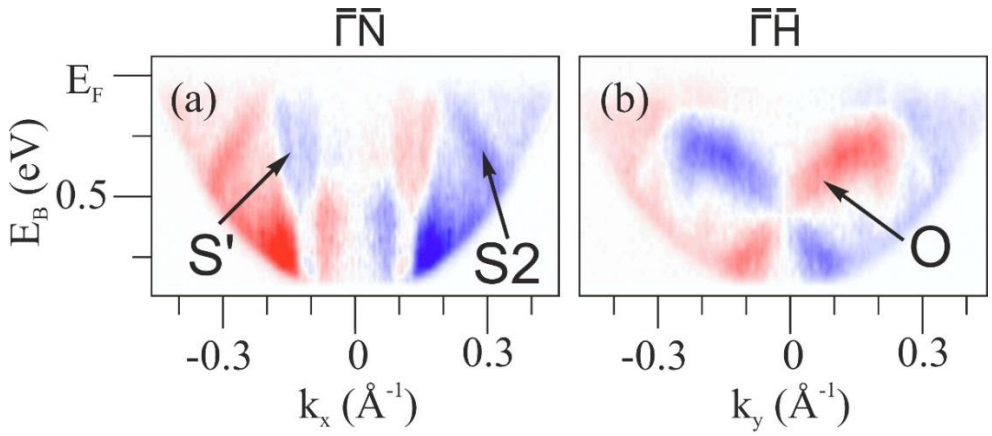


**Fig. 5.10.** Circular dichroism maps for the $2 \times 2$ oxygen superstructure on Mo(110) shown in $E_B - k_{\parallel}$ sections along $\bar{\Gamma} - \bar{\mathrm{N}}$ (a) and $\bar{\Gamma} - \bar{\mathrm{H}}$ (b) directions. The corresponding intensity patterns are shown in Fig. 5.8 (a,f). The bipolar color shows the dichroism asymmetry defined by eq. (4.11). (2PPE at $2h\nu$= 6.2 eV)

Band O shows pronounced central point symmetry upon excitation with p-polarized light along $\bar{\Gamma} - \bar{\mathrm{N}}$ in contrast to most of the other bands (especially looking at measurements with synchrotron radiation), which show mirror symmetry in this geometry. This means there is an asymmetry not only in the direction of the $E$-vector (which is the normal LDAD), but also in the perpendicular direction. The symmetrized 3D view in panels (g,h) in Fig. 5.9 shows that the inner band feature is tilted in both directions $k_x$ and $k_y$. Hence, in the canonical $E_B - k_x$ and $E_B - k_y$ sections its structure does not become visible. In the LDAD-difference images in Fig. 5.10 a strong dichroism dissymmetry appears as red-blue texture of the crossing branches of the state O for both $\bar{\Gamma} - \bar{\mathrm{N}}$ and $\bar{\Gamma} - \bar{\mathrm{H}}$ directions. In this case the light incidence plane was along $\bar{\Gamma} - \bar{\mathrm{N}}$ thus red-blue contrast is due to the LDAD effect while the contrast along $\bar{\Gamma} - \bar{\mathrm{H}}$ is because of CDAD.

In the synchrotron experiment the oxidized Mo(110) surface was prepared differently, by extended heating for 15 minutes at 1100 K in oxygen (~$5\times10^{-8}$ mbar) and subsequent flash

to about 1200 K in vacuum. At these conditions Mo(110) is known to form an epitaxial molybdenum oxide superstructure, in registry with the metal surface [130,133]. Our LEED observations were performed after band-structure mapping. Directly after the oxidation procedure the LEED pattern comprises two sets of reflexes shifting towards each other with change of the scattering energy. This behaviour is shown at the (0,0) reflex, marked with a dashed circle in Fig. 5.7(d)-(f). This effect is known to appear when the surface has a facetted structure (see, for example, the investigation by Comsa et al. for a Pt(997) surface [135]). After a brief flash in vacuum to a temperature higher than 1200 K the LEED pattern changes (Fig. 5.7(c)) and shows a structure similar to the one from the $MoO_2$ oxide shown by Radican et al. [133]. In our case we see only one reflex along one of the two equivalent crystallographic directions, indicating that the oxide film has single-crystal structure. The mechanism of formation of the rows of reflexes is due to lattice mismatch along the Mo[332] direction with coincidence periodicity of 17 units in the [100] direction. For a detailed discussion of this structure, see [133].

The measured momentum distributions (Figs. 5.11-5.12) reveal well-pronounced bands that partly resemble those of the clean Mo(110) surface, however, with a substantial shift to lower binding energies.

Fig. 5.11 shows $k_x - k_y$ cuts between the Fermi energy and $E_B$= 1.0 eV of Mo(110)-oxide prepared by heating in oxygen (panels g-l) in comparison to the case of clean Mo(110) between $E_B$= 0 and 1.8 eV (a-f, respectively). The band features here show many clear similarities as well as differences. This can be seen also in comparison of $E_B - \boldsymbol{k}_{\|}$ sections of clean and oxidized Mo(110) in Fig. 5.12. Many band features stay in general while changing their energy positions, sharpness and intensity. Several bands, particularly the band S6, appear to survive but shift to smaller binding energies. Considering this, we address the present bands in agreement (where possible) with respect to our notation for clean Mo(110) in section 5.2.

At the Fermi energy (Fig. 5.11(g)) the momentum pattern shows just a weakly pronounced diamond and a line with a central dot which is the top of a parabolic band (Fig. 5.12(d)) instead of the pronounced S6 and the diamond-shaped S3 band (see Fig. 5.11(a)). In this respect, it looks more similar to the pattern at $E_B$= 0.8 eV for clean Mo(110) in Fig. 5.11(c).

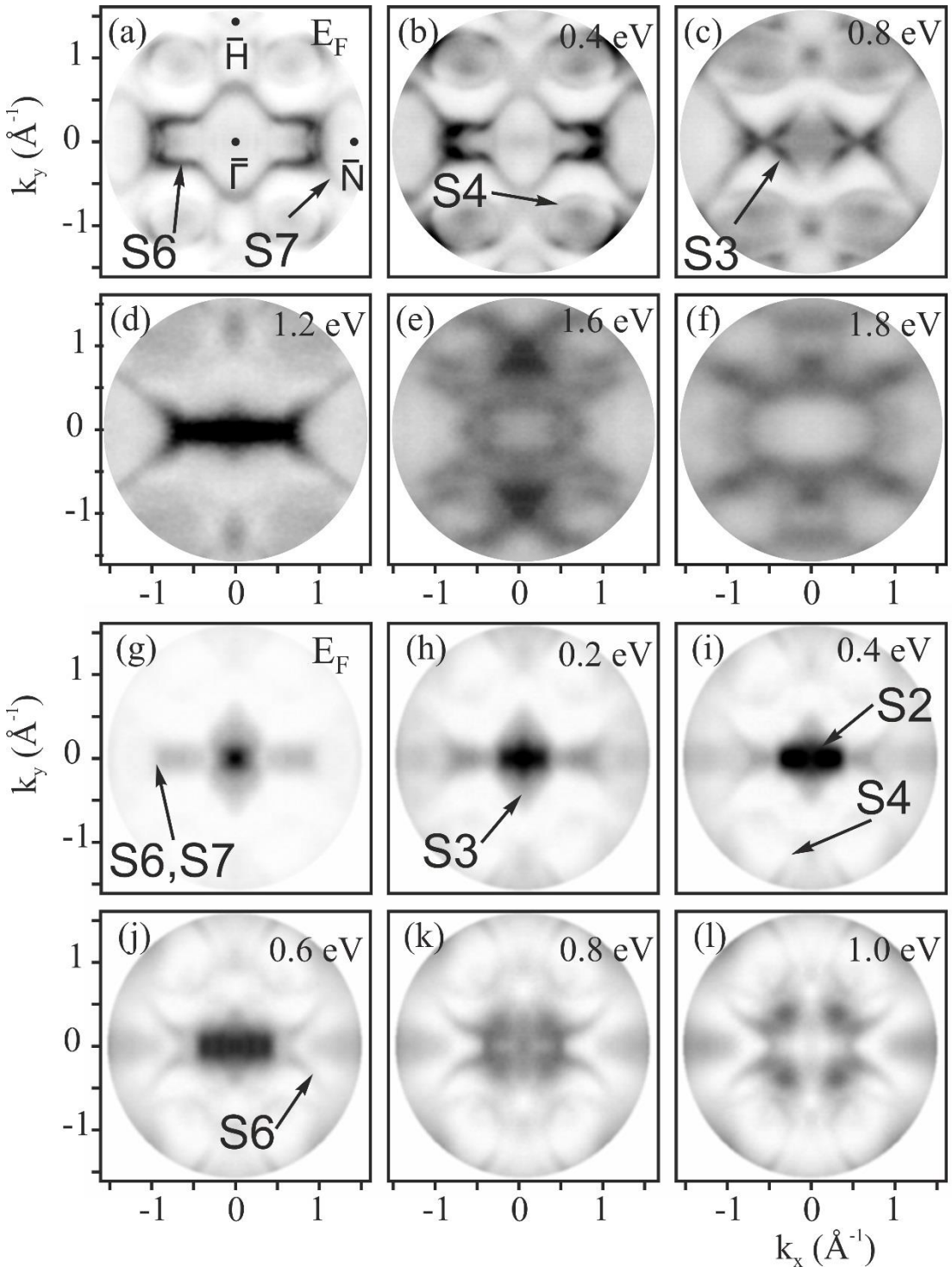


**Fig. 5.11.** $k_x - k_y$ sections of clean (a-f) and oxidized (g-l) Mo(110) for different binding energies. Energies for clean Mo(110) are chosen to emphasize the similarities. Sections for oxidized Mo(110) (g-h) are performed from $E_F$ with steps of 200 meV. (Synchrotron measurements at $h\upsilon$ = 35 eV).

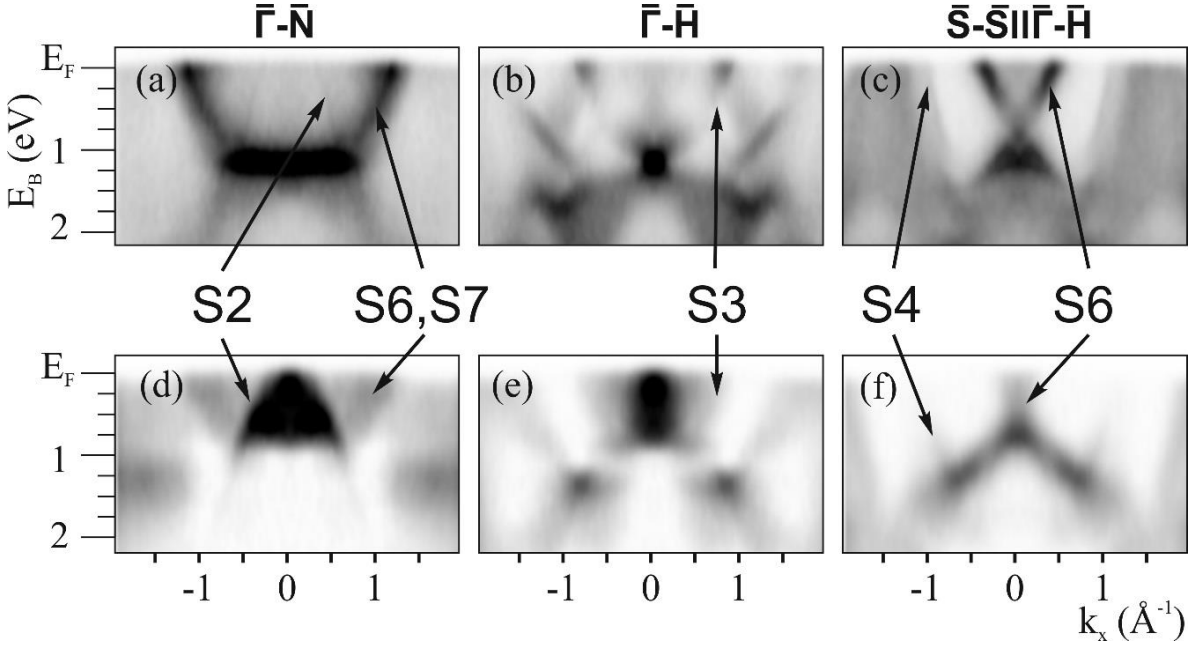


**Fig. 5.12**. Comparison of $E_B - \boldsymbol{k}_{\parallel}$ sections along $\bar{\Gamma} - \bar{\mathrm{N}}$, $\bar{\Gamma} - \bar{\mathrm{H}}$ and $\bar{\mathrm{S}} - \bar{\mathrm{S}}$ parallel to $\bar{\Gamma} - \bar{\mathrm{H}}$ directions for the clean (top row) and oxidized (bottom row) Mo(110) surface. (Synchrotron measurement at $h\upsilon$ = 35 eV).

Except band S6, the only pronounced feature visible at the Fermi surface of the Mo oxide surface has a shape of two similar rhombuses close to the $\bar{\Gamma}$-point shifted to positive and negative $k_y$-values along $\overline{\Gamma\mathrm{H}}$. The photoelectron intensity is strongly increased at the $\bar{\Gamma}$-point, where both features overlap. Fig.5.11 shows constant energy sections for energies from $E_{\mathrm{F}}$ to $E_{\mathrm{B}}$= 1 eV in steps of 200 meV. With increasing binding energy rhombuses move towards each other and the bright spot widens to the width of the overlap in the $\overline{\Gamma\mathrm{N}}$ direction (and even more at higher binding energies). However, in the $\overline{\Gamma\mathrm{H}}$ direction the width of the bright spot stays the same until the energy, where both rhombuses merge and fade out. Most pronounced features are the downward-oriented parabola in the section across $\overline{\Gamma\mathrm{N}}$ (Fig. 5.12(d)) and the intense vertical broad line in the $\overline{\Gamma\mathrm{H}}$ section (Fig. 5.12(e)). At a binding energy of 0.6 eV (Fig. 5.11(j)) the band structure comprises a pattern resembling the one of clean Mo(110) at $E_{\mathrm{B}}$= 1.2 eV (Fig. 5.11(d)), but the bright linear feature shows up not as long. Here it becomes obvious that the line consists of not just a single electron state, but is a combination of at least S3 and S7 states, as also predicted by the theoretical calculations shown in Fig. 5.5.

Comparing sections $\overline{\Gamma\mathrm{H}}$ and $\overline{\Gamma\mathrm{N}}$ of oxygenated and clean Mo(110) in Fig. 5.12 one may conclude that observed structures are connected with deformation and broadening of bands S3, S6 and S7 upon oxidation. Band S4 is present only for higher binding

energies. The section parallel to $\overline{\Gamma H}$ across two $\overline{S}$-points for oxygenated and clean Mo(110) also shows a lifting of the band structure to lower binding energies (Fig. 5.12(c),(f)). The rhombus feature, which is dominant close to $E_F$ for clean W(110) (Fig. 5.3 (a,b)) appears much weaker and diffuse for the oxidized surface (Fig. 5.11 (g,h)).This feature originates from the bulk Fermi surface of W(110).

# 6. Summary and outlook

The surprising existence of a Dirac-like state (characteristics of "massless" electrons) on the metal surface W(110), observed by Miyamoto et al. [16] rose the question whether similar states occur on the (110)-surfaces of other heavy bcc-metals. The purpose of the present Thesis was to investigate the (110)-surface of the isoelectronic bcc material molybdenum. The case of Mo is particularly interesting because spin-orbit interaction is about a factor of 5 smaller than in W. A (110) surface of a molybdenum single crystal was studied concentrating on the investigation of surface electronic states and surface resonances, and in particular the search for an anomalous state with linear dispersion.

The experimental investigations employed for the first time time-of-flight (ToF) momentum microscopy, which is a novel approach to investigate the electronic bandstructure. It aims at maximum parallelization of photoelectron data acquisition, which will be of extreme importance for measurements of samples sensitive to photon irradiation or with short lifetime. To achieve this, ToF momentum microscopy implements simultaneous detection of photoelectrons in a whole range of kinetic energies. The method combines the *k*-imaging properties of a cathode-lens microscope with parallel acquisition capability of ToF electron microscopy. A delay-line detector is a key component of the microscope. Principally the described approach can offer down to few-meV energy resolution in parallel to superb momentum space resolution. The measured resolution was about 0.01 to 0.02 $\text{Å}^{-1}$ in momentum space and 28 meV in energy. Given a k-disc diameter of about 3 $\text{Å}^{-1}$ and usable energy range of 3 eV this corresponds to > $10^6$ data voxels that are acquired simultaneously.

Theoretical investigations were performed by the group at TU Munich (H. Ebert et al.) along with experiment. Calculations were based on the fully relativistic one-step model in its spin-density matrix formulation allowing for proper description of the complete spin-polarization and also linear dichroism pattern. Calculations showed many similarities along with differences to the bandstructure of W(110), which were also confirmed experimentally.

3D data matrices of the surface bands on Mo(110) were measured in laboratory conditions with a Ti:sapphire laser and 2PPE excitation ($2h\upsilon = 6.2eV$) and with synchrotron excitation at $h\upsilon = 35eV$. The data was analysed with a closer look at cuts at $\mathrm{E_B} = const$ and $k_\mathrm{x}(k_\mathrm{y}) = const$. A constant-energy cut through the Fermi edge shows a structure quite similar to the one from W(110), as expected. On the other hand, weaker spin-orbit interaction in Mo(110) leads to smaller partial bandgap of only 120 meV width and less pronounced and smaller anomalous band S1, which shows up only in the vicinity of 1.2 eV, as also predicted by the calculations. Bands S1, S3, S6 and S7 stay visible for a full day after preparation. In contrast, S2, S4 and S5

disappear rapidly with increasing residual gas adsorption after less than one hour at $10^{-10}$ mbar. The likely reason for the longer lifetime of S3, S6 and S7 (the marked contour at $E_F$) is their existence in several surface layers i.e. they have the character of surface resonances. The character of S1 changes from surface-resonance-like in the bulk continuum to surface-state-like in the gap. S1 is the surface resonance exhibiting linear energy dispersion and a spin-polarization structure which is reminiscent of topological surface states.

The calculated section in the $\bar{\Gamma} - \bar{H}$ symmetry plane ($k_x = 0$) shows the band crossing in the center of the bandgap at $E_B$= 1.2 eV (width 120 meV) but the experiment did not resolve details of this crossing point because of insufficient energy resolution. Nevertheless the applied ToF-momentum microscopy technique allows making cuts off-center of the Brillouin zone and the cuts at $k_x$ = 0.15, 0.25 and 0.3 Å$^{-1}$ resolve the linear dispersion of S1 in the corresponding momentum region. The band S6 also shows linear dispersion and by calculations has an unusual spin texture making it a no conventional surface state.

Comparison between the calculated and experimental patterns reveals an excellent agreement including subtle band details and trends of intensities.

The geometrical arrangement of the experiment allowed for measurements of the linear dichroism in the photoelectron angular distribution investigations (LDAD). The agreement between theoretical calculations and experiment is also quite well. The obtained LDAD allowed to draw conclusions about the non-relativistic band symmetries for the bands S3, S4 and S6.

Oxygen-covered surfaces of Mo(110) were investigated in order to study the effect of chemisorption, in particular “hole doping”. Two different oxide structures were studied in the lab and during the synchrotron experiment: 2×2 oxygen superstructure and ultrathin epitaxial molybdenum oxide grown on Mo(110), respectively. For the lab experiment the 2PPE process results in a new state named S’ which is not visible in the synchrotron experiment and has not been observed before. The 2×2 oxygen on Mo(110) structure originates in a new state O in the shape of two cones shifted to positive and negative $k_y$ values with tips closely above the Fermi edge. The momentum patterns of this state show a “screw-like” behaviour with increasing binding energy.

For the oxide surface the band structure shows a rigid shift of most bands to lower binding energies in comparison to the clean Mo(110) surface. Comparing sections $\bar{\Gamma} - \bar{H}$ and $\bar{\Gamma} - \bar{N}$ of oxidized and clean Mo(110) shows that the oxidation causes a deformation and broadening of bands S3, S4, S6 and S7. A calculation for the oxygen-covered surface is in progress (S. Borek et al., to be published).

This chapter is concluded by an outlook on the future possibilities of the time-of-flight momentum microscope, which was put into operation in the framework of the present Thesis.

The possibilities of the novel type of microscope have been further explored very recently. In a beamtime in July/August 2015, the microscope has been operated with imaging spin filter at beamline U125-2 NIM at BESSY II (Berlin). In this beamtime we could show that the highly-parallelized data acquisition mode of the time-of-flight momentum microscope can also be exploited for a 3D spin analysis. In particular, we could show that more than $10^4$ data points can be acquired by the imaging spin filter. In this way, the complicated spin texture of surface and bulk Rashba-states of the topological ferroelectric GeTe(111) could be determined with unprecedented speed. Further, a spin-filtered analysis has been carried out for the W(110)-surface, which is isoelectronic to Mo(110). We could confirm the existence of the second anomalous point midway between $\bar{\Gamma}$ and $\bar{\mathrm{N}}$, which was discovered for Mo(110) in the framework of the present Thesis. This state also exists for W(110) and spin texture of this state has been measured and Rashba-type spin signature has been found.

In a second beamtime at beamline P04 at PETRA III (DESY, Hamburg) in October 2015 we operated the microscope for the first time using soft X-rays in a large photon-energy range. We observed sharp momentum distribution patterns up to a photon energy of 1300 eV at a sample temperature of 30 K. The small photon-energy band of this beamline (resolution 40,000) yielded a total energy resolution in the range of 30 meV. Given a well-focused energy range of about 3 eV this corresponds to 100 resolved energy slices acquired simultaneously. Each energy slice represents a *k*-disc of diameter 3 $\text{Å}^{-1}$. The best *k*-resolution was of about 0.02 $\text{Å}^{-1}$, yielding a total number of 18 000 data points in this *k*-disc. In total, the 3D-parallelization of data acquisition in these measurements yielded $10^5$ – $10^6$ data voxels acquired simultaneously. Sweeping the photon energy gives access to the variation of $k_\mathrm{z}$. In this way, a four dimensional $\mathrm{I}(k_\mathrm{x}, k_\mathrm{y}, k_\mathrm{z}, E_\mathrm{B})$ mapping of the complete bulk Brillouin zone could be performed with unprecedented acquisition speed.

Although there are no data yet, it is clear already that the ToF microscope will be superior to other techniques of angular resolved photoemission when it comes to the observation of ultrafast processes and transient states in electronic band structures. The true real-time capability, meaning that the 3D detector always "sees" the whole Brillouin zone and energy region of interest without sequential scanning, will allow for a most effective search for "hot spots" (e.g. k-regions of ultrafast demagnetization) in the band structure and subtle traces of transient states. In the present Thesis, this scheme of complete observation has led to the discovery of the anomalous crossing point midway between $\bar{\Gamma}$ and $\bar{\mathrm{N}}$.

# List of abbreviations:

2PPE – Two-Photon Photoemission

ARPES – Angular Resolved Photoelectron Spectroscopy

bcc-lattice – Body Centered Cubic Lattice

BFP - Backfocal Plane

BFP – Back-Focal Plane

CDAD – Circular Dichroism in the Angular Distribution

CES – Constant Energy Surface

cps – Counts per Second

DLD – Delay-Line Detector

HRTEM – High Resolution Transmission Electron Microscopy

IMFP – Inelastic Mean Free Path

KKR formalism – Korringa Kohn Rostoker formalism

LDA – Local Density Approximation

LDAD – Linear Dichroism in The Angular Distribution

LEED – Low Energy Electron Diffraction

MCP – Multichannel Plate

ML – Monolayer

PEEM – Photoemission Electron Microscope

RHEED – Reflection High Energy Electron Diffraction

SBZ – Surface Brillouin Zone

SPLEED – Spin-Polarized Low-Energy Electron Diffraction

STM – Scanning Tunnelling Microscopy

TB mode – Tight-Binding mode

TDC – Time to Digital Converter

TI – Topological Insulator

ToF – Time-of-Flight

# References


1. R. Feder. *Polarized Electrons in Surface Physics.* Singapore : World Scientific, 1985.

2. J. Kirschner. *Polarized Electrons at Surfaces.* Berlin : Springer, 1985.

3. U. Heinzmann, J. Kessler, J. Lorenz. Wavelength Dependence of the Fano Effect. *Phys. Rev. Lett. 25.* 1970, p. 1325.

4. G. Baum, M.S. Lubell, W. Raith. Spin-Orbit Perturbation in Heavy Alkali Atoms. *Phys. Rev. Lett. 25.* 1970, p. 267.

5. U. Fano. Spin Orientation of Photoelectrons Ejected by Circularly Polarized Light. *Phys. Rev. 178.* 1969, p. 131.

6. O. Heinzmann, G. Schönhense. Spin-Resolved Photoemission from Nonmagnetic Metals and Adsorbates. *Polarized Electrons in Surface Physics.* Singapore : World Scientific, 1985, p. 467.

7. K. Aulenbacher, P. Drescher, H. Euteneuer, D.V. Harrach, P. Hartmann, J. Hoffmann, K.-H. Kaiser, H.J. Kreidel, M. Leberig, Ch. Nachtigall, E. Reichert, M. Schemies, J. Schuler, M. Steigerwal, Ch. Zalto. A GaAs Type Source of Polarized Electrons at the Mainz Race Track Microtron MAMI. *Physics of Low Dimensional Systems.* s.l. : Springer US, 2001, p. 453.

8. E.I. Rashba. Properties of semiconductors with an extremum loop. 1. Cyclotron and combinational resonance in a magnetic field perpendicular to the plane of the loop. *Sov. Phys. Solid State. 2.* 1960, p. 1109.

9. Y.A. Bychkov, E.I. Rashba. Properties of a 2D electron gas with lifted spectral degeneracy. *JETP Lett. 81.* 1984 , p. 3978.

10. S. LaShell, B.A. McDougall, E. Jensen. Spin Splitting of an Au(111) Surface State Band Observed with Angle Resolved Photoelectron Spectroscopy. *Phys. Rev. Lett. 77.* 1996, p. 3419.

11. A. Tamai, W. Meevasana, P.D.C. King, C. Nicholson, A. de la Torre, E. Rozbicki, F. Baumberger. Spin-orbit splitting of the Shockley surface state on Cu(111). *Phys. Rev. B 87.* 2013, p. 075113.

12. J. Henk, A. Ernst, P. Bruno. Spin polarization of the L-gap surface states on Au(111): a first-principles investigation. *Surf. Sci. 566-568.* 2004, p. 482.

13. D. Hsieh, D. Qian, L. Wray, Y. Xia, Y.S. Hor, R.J. Cava, M.Z. Hasan. A topological Dirac insulator in a quantum spin Hall phase. *Nature 452.* 2008, p. 970.

14. S.Y. Zhou, G.-H. Gweon, J. Graf, A.V. Fedorov, C. D. Spataru, R.D. Diehl, Y. Kopelevich, D.-H. Lee, S.G. Louie, A. Lanzara. First direct observation of Dirac fermions in graphite. *Nature Physics 2.* 2006, p. 595.

15. S. Souma, K. Kosaka, T. Sato, M. Komatsu, A. Takayama, T. Takahashi, M. Kriener, Kouji Segawa, Yoichi Ando. Direct Measurement of the Out-of-Plane Spin Texture in the Dirac-Cone Surface State of a Topological Insulator. *Phys. Rev. Lett. 106.* 2011, p. 216803.

16. K. Miyamoto, A. Kimura, K. Kuroda, T. Okuda, K. Shimada, H. Namatame, M. Taniguchi, M. Donath. Spin-Polarized Dirac-Cone-Like Surface State with d Character at W(110). *Phys. Rev. Lett. 108.* 2012, p. 066808.

17. H. Mirhosseini, M. Flieger, J. Henk. Dirac-cone-like surface state in W(110): dispersion, spin texture and photoemission from first principles. *New J. Phys. 15.* 2013, p. 033019.

18. J. Braun, K. Miyamoto, A. Kimura, T. Okuda, M. Donath, H. Ebert, J. Minár. Exceptional behavior of d-like surface resonances on W(110): the one-step model in its density matrix formulation. *New J. Phys. 16.* 2014, p. 015005.

19. K. Miyamoto, A. Kimura, T. Okuda, K. Shimada, H. Iwasawa, H. Hayashi, H. Namatame, M. Taniguchi, M. Donath. Massless or heavy due to two-fold symmetry: Surface-state electrons at W(110). *Phys. Rev. B 86.* 2012, p. 161411(R).

20. K. Miyamoto, A. Kimura, T. Okuda, M. Donath. Spin polarization of surface states on W(110): Combined influence of spin–orbit interaction and hybridization. *J. Electron Spectrosc. Relat. Phenom. 201.* 2014, p. 53.

21. B. Engelkamp, H. Wortelen, H. Mirhosseini, A.B. Schmidt, J. Henk, and M. Donath,. Spin-polarized surface electronic structure of Ta(110): Similarities and differences to W(110). *Phys. Rev. B 92.* 2015, p. 085401.

22. B. Engelkamp, H. Wortelen, J. Henk, A. B. Schmidt, M. Donath. *Spin-split surface state above the Fermi level on Ta(110).* Dresden, 30 March - 04 April 2014. DPG Spring meeting.

23. E. Rotenberg, S.D. Kevan. Evolution of Fermi Level Crossings versus H Coverage on W(110). *Phys. Rev. Lett. 80.* 1998, p. 2905.

24. E. Rotenberg, J. W. Chung, S. D. Kevan. Spin-Orbit Coupling Induced Surface Band Splitting in Li/W(110) and Li/Mo(110). *Phys. Rev. Lett. 82.* 1999, p. 4066.

25. M. Hochstrasser, J.G. Tobin, E. Rotenberg, S.D. Kevan. Spin-Resolved Photoemission of Surface States of W(110)-(1x1)H. *Phys. Rev. Lett. 89.* 2002, p. 216802.

26. J. Prokop, A. Kukunin, H. J. Elmers. Nanostripes, Magnetic Anisotropies and Coupling Mechanisms in Fe/Mo(110). *Phys. Rev. Lett. 95.* 2005, p. 187202.

27. H. Hasan, C. Kane. Colloquium: topological insulators . *Rev. Mod. Phys. 82.* 2010, p. 3045.

28. M. König, S. Wiedmann, C. Brüne, A. Roth, H. Buhmann, L.W. Molenkamp, X.-L. Qi, S.-C. Zhang. Quantum spin Hall insulator state in HgTe quantum wells. *Science 318.* 2007, p. 766.

29. H. Zhang, Ch.-X. Liu, X.-L. Qi, Zh. Fang, Sh.-Ch. Zhang. Topological insulators in Bi2Se3, Bi2Te3 and Sb2Se3 with a single Dirac cone on the surface. *Nature Phys. 5.* 2009, p. 438.

30. S.V. Eremeev, G. Landolt, T.V. Menshchikova, B. Slomski, Y. M. Koroteev, Z. S. Aliev, M. B. Babanly, J. Henk, A. Ernst, L. Patthey, A. Eich, A. A. Khajetoorians, J. Hagemeister, O. Pietzsch, J. Wiebe, R. Wiesendanger, P. M. Echenique, S. S. Tsirkin, and I.R. Amiraslanov, J. H. Dil, E. V. Chulkov. Atom-specific spin mapping and buried topological states in a homological series of topological insulators. *Nature Commun. 3.* 2012, p. 635.

31. H. L. Meyerheim, D. Sander, R. Popescu, P. Steadman, S. Ferrer, J. Kirschner. Interlayer relaxation of W(110) studied surface x-ray diffraction. *Surf. Sci. 475.* 2001, p. 103.

32. R.G. Musket, W. McLean, C.A. Colmenares, D.M. Makowiecki, W.J. Siekhaus. Preparation of atomically clean surfaces of selected elements: A review. *Appl. Surf. Sci. 10.* 1982, p. 143.

33. K. Kuroda, M. Arita, K. Miyamoto, M. Ye, J. Jiang, A. Kimura, E. E. Krasovskii, E. V. Chulkov, H. Iwasawa, T. Okuda, K. Shimada, Y. Ueda, H. Namatame, M. Taniguchi. Hexagonally Deformed Fermi Surface of the 3D Topological Insulator Bi2Se3. *Phys. Rev. Lett. 105.* 2010, p. 076802 .

34. G. Schönhense. Circular Dichroism and Spin Polarization in Photoemission from Adsorbates and Non-Magnetic Solids. *Physica Scripta T31.* 1990, p. 255.

35. T. Matsushita, S. Imada, H. Daimon, T. Okuda, K. Yamaguchi, H. Miyagi, S. Suga. Linear and circular dichroism in photoemission angular distribution from the valence band of 1T-TaS2. *Phys. Rev. B 56.* 1997, p. 7687.

36. N.A. Cherepkov, G. Schönhense. Linear Dichroism in Photoemission from Oriented Molecules. *Europhys. Lett., 24 (2).* 1993, p. 79.

37. W. Kuch, C.M Schneider. Magnetic dichroism in valence band photoemission. *Rep. Prog. Phys. 64.* 2001, p. 147.

38. W. Eberhardt, F.J. Himpsel. Dipole selection rules for optical transitions in the fcc and bcc lattices. *Phys. Rev. B 21.* 1980, p. 5572.

39. D. Hsieh1 Y. Xia1, L. Wray, D. Qian, A. Pal, J. H. Dil, J. Osterwalder, F. Meier, G. Bihlmayer, C. L. Kane, Y. S. Hor, R. J. Cava, M. Z. Hasan. Observation of Unconventional Quantum Spin Textures in Topological Insulators. *Science 323.* 2009, p. 919.

40. P.A. Lee, T.V. Ramakrishnan. Disordered electronic systems. *Rev. Mod. Phys. 57.* 1985, p. 287.

41. J. Henk, M. Hoesch, J. Osterwalder, A. Ernst, P. Bruno. Spin–orbit coupling in the L-gap surface states of Au(111): spin-resolved photoemission experiments and first-principles calculations. *J. Phys.: Condens. Matter 16.* 2004, p. 7581.

42. L. Fu. Hexagonal warping effects in the surface state of the topological insulator Bi2Te3. *Phys. Rev. Lett. 103.* 2009, p. 266801.

43. T. Inui, Y. Tanabe, Y. Onodera. *Group Theory and its Applications in Physics (Springer Series in Solid State Sciences vol 78).* Berlin : Springer, 1990.

44. Sz. Vajna, E. Simon, A. Szilva, K. Palotas, B. Ujfalussy, L. Szunyogh. Higher-order contributions to the Rashba–Bychkov effect with application to the Bi/Ag(111) surface alloy. *Phys. Rev. B 85.* 2012, p. 075404.

45. J. Premper, M. Trautmann, J. Henk, P. Bruno. Spin–orbit splitting in an anisotropic two-dimensional electron gas. *Phys. Rev. B 76.* 2007, p. 073310.

46. E. Simon, A. Szilva, B. Ujfalussy, B. Lazarovits, G. Zarand, L. Szunyogh. Anisotropic Rashba splitting of surface states from the admixture of bulk states: relativistic ab initio calculations and k • p perturbation theory. *Phys. Rev. B 81.* 2007, p. 235438.

47. D. Venus, S. Cool, M. Plihal. Quantitative structural determination using spin-polarized low-energy electron diffraction rotation curves: W(110). *Surf. Sci. 446.* 2000, p. 199.

48. J. Henk. Theory of low-energy diffraction and photoelectron spectroscopy from ultra-thin films. *Handbook of Thin Film Materials vol 2.* San Diego : Academic, 2002, p. 479.

49. J. Braun. The theory of angle-resolved ultra-violet photoemission and its applications to ordered materials. *Rep. Prog. Phys. 59.* 1996, p. 1267.

50. S.V. Chernov, K. Medjanik, C. Tusche, D. Kutnyakhov, S. A. Nepijko, A. Oelsner, J. Braun, J. Minár, S. Borek, H. Ebert, H.J. Elmers, J. Kirschner, G. Schönhense. Anomalous d-like Surface Resonance on Mo(110). *Ultramic. 159.* 2015, p. 453.

51. S.V. Halilov, E. Tamura, D. Meinert, H. Gollisch, R. Feder. Relativistic Green function theory of layer densities of states and photoemission from magnetic compounds. *J. Phys. Condens. Matter 5.* 1993, p. 3859 .

52. J.B. Pendry. Theory of photoemission. *Surf. Sci. 57.* 1976, p. 679.

53. G. Borstel. Theoretical Aspects of Photoemission. *Appl. Phys. A 38.* 1985, p. 193.

54. C. Caroli, D. Lederer-Rozenblatt, B. Roulet, D. Saint-James. Inelastic Effects in Photoemission: Microscopic Formulation and Qualitative Discussion. *Phys. Rev. B 8.* 1973, p. 4552 .

55. J. Braun. New developments in UPS and XPS from ferromagnetic materials, in Band-Ferromagnetism: Ground-State and Finite-Temperature Phenomena. [book auth.] M. Donath, W. Nolting K. Baberschke. *Vol. 580, from Lecture Notes in Physics.* Berlin : Springer, 2001, p. 267.

56. J.B. Pendry. *Low Energy Electron Diffraction.* London : Academic Press, 1974.

57. G. Hilgers, M. Potthoff, N. Müller, U. Heinzmann, L. Haunert, J. Braun, G. Borstel. Necessity of self-energy corrections in LEED theory for Xe(111): Comparison between theoretical and experimental spin-polarized LEED data. *Phys. Rev. B 52.* 1995, p. 14859.

58. S.H. Vosko, L. Wilk, M. Nusair. Accurate spin-dependent electron liquid correlation energies for local spin density calculations: a critical analysis. *Can. J. Phys. 58.* 1980, p. 1200.

59. H. Ebert et al. The munich SPR-KKR package, version 6.3. [Online] 2012.

60. H. Ebert. Fully relativistic band structure calculations for magnetic solids - Formalism and Application. [book auth.] H. Dreyssé. *Electronic Structure and Physical Properties of Solids, vol. 535.* Berlin : Springer, 2000, p. 191.

61. H. Ebert, D. Ködderitzsch, J. Minár. Calculating condensed matter properties using the KKR-Green's function method—recent developments and applications. *Rep. Prog. Phys. 74.* 2012, p. 096501.

62. Y.G. Zhou, X.T. Zu, J.L. Nie, Y. Gao. Adsorption of O on Mo(110) surface from first-principles calculation. *Eur. Phys. J. B. 67.* 2009, p. 27.

63. G. Malmström, J. Rundgren. A program for calculation of the reflection and transmission of electrons through a surface potential barrier. *Comput. Phys. Commun. 19.* 1980, p. 263.

64. A. Nuber, J. Braun, F. Forster, J. Minár, F. Reinert, H. Ebert. Surface versus bulk contributions to the Rashba splitting in surface systems. *Phys. Rev. B 83.* 2011, p. 165401.

65. A. Bendounan, K. Ait-Mansour, J. Braun, J. Minár, S. Bornemann, R. Fasel, O. Gröning, F. Sirotti, H. Ebert. Evolution of the Rashba spin-orbit-split Shockley state on Ag/Pt(111). *Phys. Rev. B 83.* 2011, p. 195427.

66. J.F.L. Hopkinson, J. B. Pendry, D. J. Titterington. Calculation of photoemission spectra for surfaces of solids. *Comput. Phys. Commun. 19.* 1980, p. 69.

67. R. Matzdorf, A. Gerlach, A. Goldmann, M. Fluchtmann, J. Braun. Momentum matrix elements for angle-resolved UV-photoemission from Cu(111): comparison of experimental data and results from one-step calculations. *Surf. Sci 421.* 1999, p. 167.

68. H. Eckhardt, L. Fritsche, J. Noffke. Self-consistent relativistic band structure of the noble metals. *J. Phys. F: Met. Phys. 14.* 1984, p. 97.

69. C. Hodges, H. Smith, J. W. Wilkins. Effect of Fermi Surface Geometry on Electron-Electron Scattering. *Phys. Rev. B 4.* 1971, p. 302.

70. T. Valla, A.V. Fedorov, P.D. Johnson, S.L. Hulbert. Many-Body Effects in Angle-Resolved Photoemission: Quasiparticle Energy and Lifetime of a Mo(110) Surface State. *Phys. Rev. Lett. 83.* 1999, p. 2085.

71. S. Huefner. *Photoelectron Spectroscopy: Principles and Applications (Advanced Texts in Physics).* Berlin : Springer-Verlag GmbH, 2003.

72. A. Damascelli. Probing the Electronic Structure of Complex Systems by ARPES. *Physica Scripta. T109.* 2004, p. 61.

73. M.P. Seah, W.A. Dench. Quantitative electron spectroscopy of surfaces: A standard data base for electron inelastic mean free paths in solids. *Surf. Interface Anal. 1.* 1979, p. 2.

74. J.J. Yeh, I. Lindau. Atomic subshell photoionization cross sections and asymmetry parameters: $1 \leqslant Z \leqslant 103$. *At. Data. Nucl. Tables 32.* 1985, p. 1.

75. S. Suga, A. Sekiyama. *Photoelectron Spectroscopy.* Berlin : Springer-Verlag, 2013.

76. G.D. Mahan. Theory of Photoemission in Simple Metals. *Phys. Rev. B 2.* 1970, p. 433.

77. I. Tae Kim, G.A. Nunnery, K. Jacob, J. Schwartz, X. Liu, R. Tannenbaum. Synthesis, Characterization, and Alignment of Magnetic Carbon Nanotubes Tethered with Maghemite Nanoparticles. *J. Phys. Chem. C 114.* 2010, p. 6944.

78. Ultra High Vacuum Lab. [Online] Universität des Saarlandes. [Cited: 01 06 2015.] http://jacobs.physik.uni-saarland.de/english/instrumentation/uhvl.htm.

79. H. Rose. Future trends in aberration-corrected electron microscopy. *Phil. Trans. R. Soc. A 367.* 2009, p. 3809.

80. H. Rose, P. Hartel, D. Preikszas. Outline of the Mirror Corrector for SMART and PEEM3. *Microsc. Microanal. 10.* 2004, p. 28.

81. P. Hartel, D. Preikszas, R. Spehr, H. Müller, H. Rose. Mirror corrector for low-voltage electron microscopes. *Advances in Imaging and Electron Physics.* s.l. : Elsevier Ltd, 2002, p. 41.

82. P. Hawkes, E. Kasper. *Principles of Electron Optics.* London : Academic Press, 1996.

83. W. Engel, R. Degenhardt, A. M. Bradshaw, W. Erlebach, K. Ihmann, H. Kuhlenbeck, R. Wichtendahl, H.-J. Freund, R. Schlögl, D. Preikszas, H. Rose, R. Spehr, P. Hartel, G. Lilienkamp, Th. Schmidt, E. Bauer, G. Benner, R. Fink, M. R. Weiss, E. Umbach. Concept and Design of the SMART Spectromicroscope at BESSY II. *X-Ray Microscopy and Spectromicroscopy.* Heidelberg : Springer-Verlag GmbH, 1998, p. 271.

84. M. Kotsugi, W. Kuch, F. Offi, L. I. Chelaru, J. Kirschner. Microspectroscopic two-dimensional Fermi surface mapping using a photoelectron emission microscope. *Rev. Sci. Instrum. 74.* 2003, p. 2754.

85. https://www.vgscienta.com. [Online] VG Scienta. [Cited: 22 04 2015.] http://www.vgscienta.com/productlist.aspx?MID=389.

86. [Online] VG SCIENTA. [Cited: 01 06 2015.] http://www.vgscienta.com/productlist.aspx.

87. D. Roy, J. D. Carette. *Electron Spectroscopy for Surface Analysis.* Berlin : Springer-Verlag GmbH, 1977.

88. B. Krömker, M. Escher, D. Funnemann, D. Hartung, H. Engelhard, J. Kirschner. Development of a momentum microscope for time resolved band structure imaging. *Rev. Sci. Instrum. 79.* 2008, p. 053702.

89. Wikipedia. [Online] https://en.wikipedia.org/wiki/Angle-resolved_photoemission _spectroscopy.

90. M. Escher, N. Weber, M. Merkel, C. Ziethen, P. Bernhard, G. Schönhense, S. Schmidt, F. Forster, F. Reinert, B. Krömker, D. Funneman. NanoESCA: a novel energy filter for imaging x-ray photoemission spectroscopy. *J. Phys.-Condens. Mat.* 2005, p. S1329 .

91. M. Escher, K. Winkler, O. Renault, N. Barrett. Applications of high lateral and energy resolution imaging XPS with a double hemispherical analyser based spectromicroscope. *J. Electron Spectrosc. 178–179.* 2010, p. 303.

92. C. Tusche, A. Krasyuk, J. Kirschner. Spin-resolved bandstructure imaging with a high resolution momentum microscope. *Ultramicroscopy.* 2015, doi: 10.1016/j.ultramic.2015.03.020.

93. R.E. Imhof, A. Adams, G.C. King. Energy and time resolution of the 180º hemispherical electrostatic analyser. *J. Phys. E: Sci. Instrum. 9.* 1976, p. 138.

94. L.D. Landau, E. M. Lifschitz. *Lehrbuch der Theoretischen Physik.* Berlin : Akademie, 1976.

95. A. Oelsner, O. Schmidt, M. Schicketanz, M. Klais, G. Schönhense. Microspectroscopy and imaging using a delay line detector in time-of-flight photoemission microscopy. *Rev. Sci. Instrum. 72.* 2001, p. 3968.

96. J. Henk, A. Ernst, P. Bruno. Spin polarization of the L-gap surface states on Au(111). *Phys. Rev. B 68.* 2003, p. 165416.

97. J. Henk, M. Hoesch, J. Osterwalder, A. Ernst, P. Bruno. Spin–orbit coupling in the L-gap surface states of Au(111): spin-resolved photoemission experiments and first-principles calculations. *J. Phys.: Condens. Matter 16.* 2004, p. 7581.

98. E. Rotenberg, O. Krupin, S.D. Kevan. Surface states and spin density wave periodicity in Cr(110) films. *New J. Phys. 10.* 2008, p. 023003 .

99. A. Oelsner, O. Schmidt, M. Schicketanz, M. Klais, G. Schönhense, V. Mergel, O. Jagutzki, H. SchmidtBöcking. Microspectroscopy and imaging using a delay line detector in time-of-flight photoemission microscopy. *Rev. Sci. Instrum. 72.* 2001, p. 3968.

100. D.T. Grubb. Radiation damage and electron microscopy of organic polymers. *J. Mater. Sci 9.* 1974, p. 1715.

101. C. Heller, H.M. McConnell. Radiation Damage in Organic Crystals. II. Electron Spin Resonance of (CO2H)CH2CH(CO2H) in β-Succinic Acid. *J. Chem. Phys. 32.* 1960, p. 1535.

102. D. Kutnyakhov, P. Lushchyk, A. Fognini, D. Perriard, M. Kolbe, K. Medjanik, E. Fedchenko, S.A. Nepijko, H.J. Elmers, G. Salvatella, C. Stieger, R. Gort, T. Bähler, T. Michlmayer, Y. Acremann, A. Vaterlaus, F. Giebels, H. Gollisch, R. Feder, C. Tusche, and A. Krasyuk, J. Kirschner, G. Schoenhense. Imaging spin filter for electrons based on specular reflection from iridium (001). *Ultramicroscopy 130.* 2013, p. 63.

103. M. Kolbe, P. Lushchyk, B. Petereit, H. J. Elmers, G. Schönhense, A. Oelsner, C. Tusche, J. Kirschner. Highly Efficient Multichannel Spin-Polarization Detection. *Phys. Rev. Lett. 107.* 2011, p. 207601 .

104. C.S. Fadley. X-ray photoelectron spectroscopy: Progress and perspectives. *J. Electron Spectorc. 178-179.* 2010, p. 2.

105. A. Oelsner, M. Rohmer, C. Schneider. Time- and energy resolved photoemission electron microscopy-imaging of photoelectron time-of-flight analysis by means of pulsed excitations. *J. Electron Spectrosc. 178-179.* 2015, p. 317.

106. G. Schönhense, K. Medjanik, H.J. Elmers. Space-, time- and spin-resolved photoemission. *J. Electron Spectrosc. Relat. Phenom.* 2015, doi: 10.1016/j.elspec.2015.05.016.

107. H. Spiecker, O. Schmidt, Ch. Ziethen, D. Menke, U. Kleineberg, R.C. Ahuja, M. Merkel, U. Heinzmann, G. Schönhense. Time-of-flight photoelectron emission microscopy TOF-PEEM: first results. *Nucl. Instrum. Meth. A 406.* 1998, p. 499.

108. C. Tusche, M. Ellguth, A. A. Üna, C.-T. Chiang, A. Winkelmann, A. Krasyuk, M. Hahn, G. Schönhense, J. Kirschner. Spin resolved photoelectron microscopy using a two-dimensional spin-polarizing electron mirror. *Appl. Phys. Lett. 99.* 2011, p. 032505.

109. S. Suga, C. Tusche. Photoelectron spectroscopy in a wide hν region from 6 eV to 8 keV. *J. Electron Spectrosc. 200.* 2015, p. 119.

110. P. Ranade, H. Takeuchib, T.-J. Kingb, C. Hub. Work Function Engineering of Molybdenum Gate Electrodes by Nitrogen Implantation. *Electrochem. Solid St. 4.* 2001, pp. G85-G87.

111. G. Schönhense, K. Medjanik, C. Tusche, M. de Loos, B. van der Geer, M. Scholz, F. Hieke, N. Gerken, J. Kirschner, W. Wurth. Correction of the deterministic part of space–charge interaction in momentum microscopy of charged particles. *Ultramicroscopy.* 2015, doi:10.1016/j.ultramic.2015.05.015.

112. J. Henk, A. Ernst, P. Bruno. Spin polarization of the L-gap surface states on Au(111). *Phzs. Rev. B 68.* 2003, p. 165416.

113. J. Hölzl, F. K. Schulte. Work Function of Metals. *Springer Tracts in Modern Physics Vol. 85.* Berlin : s.n., 1979.

114. https://www.helmholtz-berlin.de. [Online]

115. G. Schönhense. Circular Dichroism and Spin Polarization in Photoemission from Adsorbates and Non-Magnetic Solids. *Physica Scripta T31.* 1990, p. 255.

116. J. Feydt, A. Elbe, H. Engelhard, G. Meister, Ch. Jung, A. Goldmann. Photoemission from bulk bands along the surface normal of W(110). *Phys. Rev. B 58.* 1998, p. 14007.

117. J. Feydt, A. Elbe, H. Engelhard, G. Meister, A. Goldmann. Normal-emission photoelectron studies of the W(110)(1×1)O surface. *Surf. Sci. 440.* 1999, p. 213.

118. A. Eiguren, C. Ambrosch-Draxl. Spin polarization and relativistic electronic structure of the 1×1 H/W(110) surface. *New J. Phys 11.* 2009, p. 013056.

119. J. Kröger, T. Greber, J. Osterwalder. Angle-resolved photoemission study of clean and hydrogen-saturated Mo(110). *Phys. Rev. B 61.* 2000, p. 14146.

120. K. Jeong, R. H. Gaylord, S. D. Kevan. Experimental Fermi surface of Mo(011). *Phys. Rev. B 39.* 1989, p. 2973.

121. M. Okada, E. Rotenberg, S. D. Kevan, J. Schäfer, B. Ujfalussy, G. M. Stocks, B. Genatempo, E. Bruno, E. W. Plummer. Evolution of the electronic structure in Mo1−xRex alloys. *New J. of Physics 15.* 2013, p. 093010.

122. S.D. Kevan. Fermi contours and surface dynamical phenomena. *Surf. Sci 307-309.* 1994, p. 832.

123. M. Izquierdo, L. Roca, J. Avila, G. Gu, Z. Z. Li, H. Raffy, M. C. Asensio. Effects of the doping and the number of planes on the shadow bands of Bi-based cuprates. *Eur. Phys. J. B 46.* 2005, p. 309.

124. C. Westphal, J. Bansmann, M. Getzlaff, G. Schönhense. Circular dichroism in the angular distribution of photoelectrons from oriented CO molecules. *Phys. Rev. Lett. 63.* 1989, p. 151.

125. G.H. Fecher. The Solid Surface as Origin of Circular Dichroism in the Angular Distribution of Photoelectrons from Spherical States of Adsorbates. *Eur. Phys. Lett. 29.* 1995, p. 605.

126. S. K. Semenov, N. A. Cherepkov, G. H. Fecher, G. Schönhense. Generalization of the atomic random-phase-approximation method for diatomic molecules: N2 photoionization cross-section calculations. *Phys. Rev. A 61.* 2000, p. 032704.

127. G. Schönhense. Spin-Dependent Effects in Photoemission. *Vacuum 41.* 1990, p. 506.

128. G. Schönhense, C. Westphal, J. Bansmann, M. Getzlaff. Circular Dichroism in Photoemission from Nonmagnetic Low-Z Solids:A Conspicuous Effect of the Photon Spin. *Europhys. Letters 17* . 1992, p. 727.

129. G. Schönhense, C. Westphal, J. Bansmann, M. Getzlaff, J. Noffke, L. Fritsche. Circular Dichroism in Photoemission from Surfaces. *Surface Science 251/252* . 1991, p. 132.

130. T.W. Haas, A.G. Jackson. Low-Energy Electron-Diffraction Study of Molybdenum (110) Surfaces. *J. Chem. Phys. 44.* 1966, p. 2921.

131. H.M. Kennett, A.E. Lee. The Initial Oxidation of Molybdenum. I. LEED and RHEED observations on (110) molybdenum. *Surf. Sci. 48.* 1975, p. 591.

132. H.M. Kennett, A.E. Lee. The Initial Oxidation of Molybdenum. IV. Epitaxial Growth of Oxide on Molybdenum. *Surf. Sci. 48.* 1975, p. 624.

133. K. Radican, N. Berdunov, G. Manai, I.V. Shvets. Epitaxial molybdenum oxide grown on Mo(110): LEED, STM, and density functional theory calculations. *Phys. Rev. B 75.* 2007, p. 155434.

134. E. Bauer, H. Poppa. On the adsorption of oxygen on the Mo{110} surface and its vicinals. *Surf. Sci. 127.* 1983, p. 243.

135. G. Comsa, G. Mechtersheimer, B. Poelsema. He Beam Scattering and LEED Evidence For Partial Facetting of a Pt(997) Surface. *Surf. Sci. Lett. 97.* 1980, p. L297.

## List of publications:

1. S.V. Chernov, K. Medjanik, C. Tusche, D. Kutnyakhov; S.A. Nepijko, A. Oelsner, J. Braun, J. Minár, S. Borek, H. Ebert, H.J. Elmers, J. Kirschner, G. Schönhense. *Anomalous d-like Surface Resonance on Mo(110) Analyzed by Time-of-Flight Momentum Microscopy. Ultramic. 159.* 2015, p. 453.
2. S.V. Chernov, Z.M. Makukha, I.Yu. Protsenko, S.A. Nepijko, H.J. Elmers, G. Schönhense. *Test object for emission electron microscope*. Appl Phys A. 114. 2014, p. 1383.

## Other publications:

3. S.A. Nepijko, O. Fedchenko, S.V Chernov, G. Schönhense. *Growth and defect studies of CdTe particles*. Cryst. Res. Technol. 48, No. 5. 2013, p. 287.
4. S.A. Nepijko, A. Chernenkaya, K. Medjanik, S.V. Chernov, D.V. Shapko, I.Yu. Protsenko, W. Schulze, G. Schönhense. *Investigation of a Ge nanoparticle film by means of electron stimulated photon emission spectroscopy*. J. Electron Spectrosc. 193, 2014, p. 54.
5. S.A. Nepijko, A. Chernenkaya, K. Medjanik, S.V. Chernov, M. Klimenkov, O.V. Vlasenko, S.S. Petrovskaya, L.V. Odnodvorets, Ya.V. Zaulichnyy, G. Schönhense. *Soft X-ray emission spectroscopy used for the characterization of a-C and CNx thin films*. Thin Solid Films. 577. 2015, p. 109.
6. I. Shpetnyi, A.S. Kovalenko, M. Klimenkov, I.E. Protsenko, S.V. Chernov, S.A. Nepijko, H.J. Elmers, G. Schönhense. *Characterization and magnetic properties of nanoparticles based on FePt solid solution with an oxide shell*. J. Magn. Magn. Mater. 373. 2015, p. 231.
7. A.V. Zaporozhchenko, S.V. Chernov, L.V. Odnodvorets, B.V. Stetsenko, S.A. Nepijko, H.J. Elmers, G. Schonhense. *Photon-assisted field emission from a Si tip at addition of an AC low voltage*. Appl. Phys. A. 120. 2015, p. 161.
8. O. Fedchenko, S.V. Chernov, M. Klimenkov, S.I. Protsenko, S.A. Nepijko, G. Schonhense. *TEM Investigation of Oxidation of (110) NiAl Single Crystal with Non-Stoichiometry Composition (Surplus of Ni).* Jpn. J. Appl. Phys. (in press).
9. E.D. Schaefer, S.V. Chernov, A.A. Sapozhnik, D.M. Kostyuk, A.V. Zaporozhchenko, I.A. Khromov, S.I. Protsenko, M. Bode, S.A. Nepijko, H.J. Elmers, G. Schonhense.

*Investigation of Fe/W(110) system by using scanning tunneling microscopy and Lorentz microscopy*. Jpn. J. Appl. Phys. (in press).

10. O.N. Martyanov, D.A. Balaev, O.V. Pylypenko, L.V. Odnodvorets, S.V. Chernov, S.A. Nepijko, H.J. Elmers, C.M. Schneider, G. Schonhense. *FMR investigations of two-dimensional periodic arrays of disc-shaped Co particles at different temperatures. J. Supercond*. Nov. Magn. 2015, doi:10.1007/s10948-015-3178-3 (in press).

# Acknowledgements

I would like to thank all people who participated directly or indirectly during the long and complicated preparation of the present work.

There is no specific order in how I mention everyone in this chapter. Also I want to apologize that I cannot make the list full and mention all whom I want to express my sincere thanks. But the limiting factors are purely physical and thus could not be overcome: space and time.

I want to give my thanks to professor for giving me the great opportunity to join the working group at the University of Mainz and to other professors for providing me literally all possible kinds of support during my work.

I would like to thank to the research group which performed calculations appearing in the work and discussions about theoretical aspects.

I am grateful to developers and creators of the electron detector for their job, on-time help and warm communication.

Another thanks go to my group mates and to our whole big joint Ukrainian-Russian-German scientific community at University of Mainz and in Germany in general.

I want to thank my family, especially my parents for their major support in everything I do.

At last but not at least, I want to express my appreciation to friends, who helped me to make it through. Thanks to all of you, Anna, Alexander, Alexey, Alisa, Dmitry, Eduard, Elena, Eugenia, Gerd, Hans, Katerina, Lubov, Margarita, Mariah, Martin, Maximilian, Olga, Pavel, Polina, Sergey, Valery, Vladimir, and many others.